Monte Carlo Studies on Liquid Crystalline Systems

A Thesis submitted to the University of Hyderabad for the award of the degree of

Doctor of Philosophy

in Physics

by

Regina Jose

School of Physics
University of Hyderabad
Hyderabad - 500046, India

November 2014

Declaration

I hereby declare that the work presented in this thesis has been carried out by me under the supervision of Prof. V. S. S. Sastry, School of Physics, University of Hyderabad, Hyderabad, India, as per the Ph. D. ordinances of the University. I declare to the best of my knowledge, that no part of this thesis has been submitted for the award of a research degree of any other University. I hereby agree that my thesis can be deposited in Shodhganga/INFLIBNET.

Regina Jose
Reg. No: 07PHPH04

Certificate

This is to certify that the thesis entitled **Monte Carlo Studies on Liquid Crystalline Systems** being submitted to the University of Hyderabad by **Regina Jose** (Reg. No. 07PHPH04), for the award of the degree of Doctor of Philosophy in Physics, is a record of *bonafide* work carried out by her under my supervision and is free of plagiarism.

The matter embodied in this report has not been submitted to any other University or Institution for the award of any degree or diploma.

Prof. V. S. S. Sastry,
Thesis Supervisor,
School of Physics,
University of Hyderabad.

Dean,
School of Physics,
University of Hyderabad.

Acknowledgments

I would like to thank my thesis supervisor Prof. V. S. S. Sastry for being a wonderful mentor to me. I would always be indebted to him for his encouragement on my research.

I am thankful to Prof. Slobodan Žumer and Dr. Gregor Skačej (University of Ljubljana, Slovenia) for the research collaboration we had together, and also for their cordial hospitality.

I thank Prof. K. P. N. Murthy and Dr. Surajit Dhara for the valuable academic discussions and suggestions. I have benefited from the academic discussions we had with Prof. N. V. Madhusudana (RRI, Bangalore).

I thank Prof. S. R. Shenoy, Prof. S. N. Kaul, Prof. M. Sivakumar and Prof. P. K. Suresh for the training during the initial course work.

I thank all the former and present Deans of the School of Physics for their continuous support. The Directors and staff of the Centre for Modeling Simulation and Design (CMSD) are gratefully acknowledged for extending the computational facilities.

Thanks to T. Abraham and other staff in the School of Physics for all their help.

Thanks are due to the colleagues in our research group: Sai Preeti, Jayasri, Kamala Latha, Trivikram, Rajeswari and all the other members of *Boltzmann* group. I also thank the colleagues of the soft matter research group in Ljubljana.

I remember my friends Mini, Monisha, Saipriya, Yashaswini, Suman, Sathyanarayana, Balu, Siva, Hongray, Gopal Krishna, Suresh, Sekhar and Senthil. My unending thanks to my dearest family for the continual support.

Assistance from the Universty of Hyderabad (through BBL scholarship), Council of Scientific and Industrial Research (New Delhi, India, through NET-SRF fellowship) and European Union (through EC ITN Marie Curie Early Stage Researcher fellowship of the network HIERARCHY) are also gratefully acknowledged.

Preface

Liquid crystals are soft materials that continue to excite technologists and scientists due to their easy-to-manipulate features arising from their susceptibility (sensitivity) to external influences. They exhibit notable anisotropy in their magnetic, electrical and optical properties due to the crystal-like behaviour originating from long range orientational order. On the other hand partial or no positional order endows them with liquid-like flow properties. The simplest of the various phases in this class is the nematic phase where the constituent molecules align orientationally on an average along an apolar director $\boldsymbol{n} = (-\boldsymbol{n})$, with an isotropic distribution of their centers of masses. Such phases are typically formed in media hosting molecules with highly anisotropic polarizabilities, interacting primarily through van der Waals-type and steric interactions.

Liquid crystals forming uniaxial nematic phase (from rod-like or disk-like molecules) with cylindrical symmetry about their director are found to be extremely feasible for display devices. For most of the practical purposes such as the measurement of their properties for characterization, or for technological applications, liquid crystals are confined to limiting surfaces. Nematic films are the most common amongst confined liquid crystal systems because of their simpler geometry for experiments and applicability in the display devices. They are suitable for studying anchoring effects of the confining substrates and the elasticity of the medium. Films with agreeable, hybrid or conflicting anchoring influences at both the substrates come handy for many different applications.

Biaxial nematics formed by constituents (lath-like molecules) of similar symmetry (wherein the phase no more has a cylindrical symmetry), was conceived and predicted both by molecular mean-field and Landau theory-based approaches, as well as by computer simulations. To date, the phase remains unarguably realized only in lyotropic systems where the solute concentration determines the phase properties. Since such a control parameter is practically inconvenient for applications, an irrefutable experimental realization of a biaxial phase in thermotropic liquid crystals, stable over a reasonable temperature range, can set a breakthrough in liquid crystal research and in technology-based applications, such as energy-efficient display devices with in-plane switching.

Another class of materials which is gaining momentum is the colloidal nematics where surfactant coated colloidal particles of nano- to micrometer range are dispersed in a nematic liquid crystal host. The particles are observed to self-assemble to form robust colloidal crystalline structures with binding energies which are 100-1000 k_BT times larger than those with particles or nematic droplets in an isotropic host like water. Here the van der Waals interactions of the particles are typically screened out within distances of the order of molecular length scales, and the dominant interactions of the particles with the anisotropic medium is *via* the surface forces brought in by the orientational anchoring on their surfaces. The particle inclusions produce director deformations in the host liquid crystal, giving rise to defects in the orientational field called disclinations. These curvature elasticity-mediated interactions thus result in fascinating metamaterials that are of interest from a topological point of view, as well as for applications such as in photonic devices, due to their larger interstitial spacing comparable to that of the wavelength of light.

Computer-based simulation experiments with appropriate Hamiltonian models have emerged as a powerful branch in scientific research to substantiate and complement laboratory-based experimental observations, validate proposed theoretical models, as well as to predict in favourable circumstances new physical phenomena. The choice of the simulation technique of course depends on the actual physical process of interest, based on the time and length scales of the system under study. In this thesis we employ Monte Carlo simulation methods based on Boltzmann and non-Boltzmann sampling methods to study various liquid crystalline systems. Alongside their impressive success in extracting physical features of the systems, these methods could also pose limitations with respect to the manipulation of different control parameters, or when pressed into service to deal with complex systems. This urges for the need to extend or adapt the current computational techniques suitably, so as to provide means to handle such cases reasonably satisfactorily.

In this context, the present work attempts to investigate some of these interesting liquid crystalline systems using Monte Carlo simulation methods. This includes

a detailed investigation of the stable and permissible director structures in a nematic film using canonical Boltzmann sampling method as well as entropic sampling method. This study necessitated development of a new sampling method, guiding a uniformly distributed random walk along another reaction coordinate, the order parameter. This turned out to be successful in visiting rare regions of the microstate space which are compatible with the imposed experimental conditions, but inaccessible by other methods. This sampling method is further extended to study bulk uniaxial and biaxial nematic systems to examine qualitatively different and rare fluctuations of the equilibrium states. Another problem of interest is the study of the effect of an external field on the isotropic-nematic transition in a uniaxial system with special interest in the low field regime, using entropic sampling method to achieve the required very high resolution with respect to high temperature. The study is subsequently extended to a biaxial nematic system keeping in view the curious effects of the external field on the phase transition temperatures depending on the choice of the interaction parameters. Lastly, we simulate a colloidal nematic system to understand the behaviour of a colloidal particle in the vicinity of a nematic disclination using Boltzmann simulation method. This study, involving distinct time and length scales, required adaptation of the single spin-flip algorithm to encompass local director equilibration process. Presentation of the results of these investigations in the thesis is organized in seven chapters.

The first chapter introduces liquid crystal physics relevant for the work. This includes the description of uniaxial and biaxial nematic phases and a brief review of the important theories associated with the phase transitions involved. Elastic distortions in the nematic medium and the effect of external influences due to surface anchoring and bulk fields are discussed. Discussion on nematic disclinations and topological effects in colloidal nematic systems are briefly presented. The chapter concludes by introducing the model Hamiltonians used in the simulations, describing these phases and associated phenomena. We use Lebwohl-Lasher model which is a lattice discretized form of Maier-Saupe potential for the interaction between uniaxial constituents. While studying the biaxial systems, a three-parameter Hamiltonian based on the interactions between the uniaxial and biaxial orientational tensor components of the constituents with D_{2h} symmetry is

used. The second chapter describes various Monte Carlo techniques employed to study the statistical physics of our systems. In particular, conventional Metropolis algorithm-based Boltzmann sampling method, and the newer non-Boltzmann entropic sampling-based Wang-Landau sampling method are discussed. Simulational procedure for determining the various properties of liquid crystalline systems is also presented.

The third chapter deals with the different director structures observed in a planar liquid crystal film confined between substrates inducing homeotropic (perpendicular to the substrate surface) anchoring. In addition to the 'trivial' solution predicted by continuum-based theories, we observe that at lower temperatures the system can condense (depending on its thickness) into a qualitatively different director structure that is stable over a wide temperature range below the isotropic-nematic phase transition temperature. The microstate spaces of these two structures are found to be disconnected in that they remain nontraversible from one to the other in the course of Markov chain Monte Carlo dynamics. Boltzmann sampling and energy-based entropic sampling are used to investigate the system in this respect. An order parameter-based entropic sampling method (OP-sampling) is proposed and successfully applied to this system, to extract microstates of the system belonging to the two different director structures, with comparable macroscopic parameters such as energy and order parameter. Further investigations reveal that the two director structures are topologically distinct apparently forbidding a continuous transformation from one to the other.

In the fourth chapter we apply OP-sampling method to bulk nematic systems of uniaxial and biaxial liquid crystals. Rather impressively, the method could detect the presence of rare microstates, which are practically inaccessible by any other techniques. Orientational correlations of these states are studied as a function of the order parameter, and are observed to behave distinctly from those of the expected bulk-like behaviour. In the case of biaxial liquid crystals where the Hamiltonian has more control parameters, correlation studies disclose the fascinating qualitative diversity of microstates available within the given energy sheet.

The fifth chapter deals with the study of the effect of an externally applied field, E_a in bulk nematic systems. Initially a uniaxial system is subjected to E_a and its effect on the isotropic-nematic (IN) transition temperature is investigated using the entropic sampling method. The field induces very fine shifts in the paranematic-nematic transition temperature, T_{PN}. This shift is seen to be linear with respect to E_a for very small values of the field, contrary to the expectations based on the form of the field-dependent interaction term in the Hamiltonian. These findings are in accord with the earlier experiments, which attributed this linearity to the quenching of director fluctuations due to the interaction of the field with the LC molecules. Confirmation of the consequences based on phenomenological theory with simulations involving microscopic interactions with only nearest neighbour interactions is very satisfactory and noteworthy. We extended this work to carry out a systematic study of the effect of an external field on a bulk biaxial system for various sets of interaction parameters. Variation of the transition temperature to the biaxial phase is observed to be of non-universal nature with respect to E_a, and is seen to depend on the choice of the Hamiltonian parameters. Referencing this discussion to the delineation of the parameter space based on biaxial stability criteria, the transition temperature is affected differently depending on the uniaxial torque axis of the system *vis-à-vis* the direction of the applied field. The contribution to the enhancement of the transition temperature (to the biaxial phase) are seen to arise from the quenching of the fluctuations of the secondary directors, associated with the corresponding minor molecular axes.

In the sixth chapter we study the interaction between a colloidal nanoparticle and a nematic disclination, which forms the basis of a nematic colloidal crystal, understanding of which remains rather elusive to date. Large scale simulations with the Lebwohl-Lasher interaction are performed aiming at extracting detailed behaviour at a nanoscale. It may be noted that simulations on such large systems based on off-lattice, coarse-grained or atomistic model are less practical due to computational costs. Treatment of this problem by continuum-based phenomenological approaches also faces certain difficulties due to the constraints on the lower limit of length scales they can probe into. The conventional single spin-flip simulation procedure is adapted to accommodate multiscales entering into the problem

taking advantage of the relatively slow translational motion of a larger particle in equilibrium in relation to the dynamics of the liquid-crystalline medium. The disclination line is stretched by moving the colloid, as in the laser-tweezing experiments, and this results in a restoring force attempting to minimize the disclination length. From the constant-force simulations we extract the corresponding disclination line-tension, and observe its decrease with increasing temperature. The seventh chapter summarizes relevant results and conclusions arising from the reported work in the thesis, and points to its plausible extensions, and ensuing open problems, for possible future investigations.

Contents

List of Figures

List of Tables

Chapter 1

Introduction to liquid crystalline systems

Liquid crystals (LCs) exist in a variety of phases with a degree of molecular order intermediate between the isotropic liquid and the crystalline solid. These properties are reflected in their macroscopic behaviour, and these can easily be manipulated by external influences, thereby imparting to them characteristics of a representative soft matter. The interaction between molecules forming such phases tend to align them parallel to each other thus defining an average direction for the preferred orientation of the molecules, called the director $\boldsymbol{n}$ [1, 2]. Consequently the ordered phases of LCs exhibit optical, electrical and magnetic anisotropy. The phases are classified according to the kind of orientational order which exists among the constituent molecules, and to the degree to which they lack their positional order. In thermotropic LCs for which temperature is the control parameter for the phase behaviour, orientational order is governed by the shape of the molecule (rod, disc, lath, banana, *etc.*). On the other hand, the properties of lyotropic LCs are governed by the relative concentration of the solute in the solvent. The distinction between these two types is not complete and the materials that exhibit both the properties are called amphotropic.

Due to their high birefringence leading to a clear manifestation of optical properties, and convenient working temperature range, LCs continue to excite scientists and technologists for different complementing reasons. It is then not very surprising that they find versatile applications in a wide range of electro-optical devices such as displays, temperature indicators, photonic crystals, wave guiding of light, lasers, lenses *etc.* LC-polymer systems have found further use in switchable windows, high modulus fibres and artificial muscles [3]. LC-colloidal systems are becoming promising candidates for photonic crystals [4].

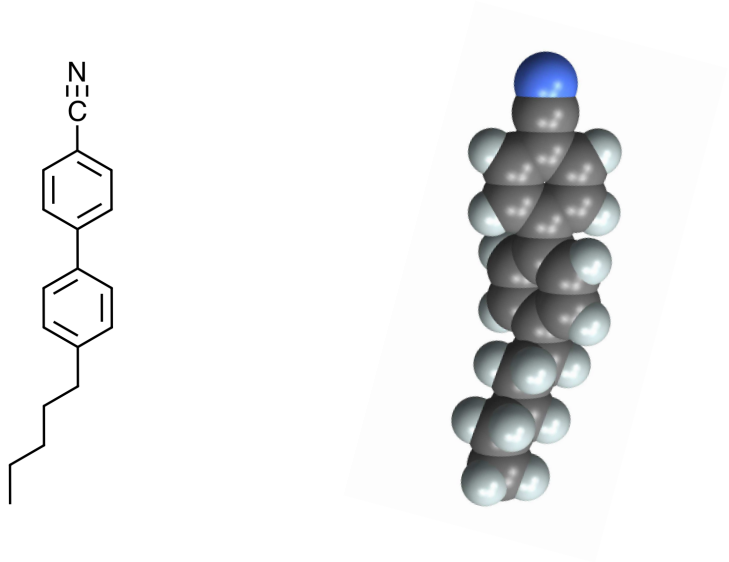

(a) (b)

Figure 1.1: (a) Two dimensional chemical structure of 5CB and (b) its three dimensional space-filling model where white, grey and blue represent hydrogen, carbon and nitrogen atoms respectively. The molecule is ~ 2 nm in length, and ~ 0.5 nm in width. It exhibits a nematic phase between 24 °C and 35 °C.

Studies towards this thesis are concentrated on LCs exhibiting nematic phase, both uniaxial and biaxial. Nematic phases are formed by anisotropic molecules and are characterized by long range orientational order, while retaining continuous translational symmetry of molecular positions reminiscent of the isotropic fluid. They lack correlation of centres of mass of molecules, but for the very short-range molecular organization. The phase is uniaxial if only one of the axes (longest for rod-like and shortest for disc-like molecules) of the molecules tend to be parallel, and is biaxial if all the faces are parallel to each other leading to secondary director axes. Most of the rod-shaped nematic materials currently in vogue consist of two (or more) benzene rings associated with different functional groups, besides short flexible exterior chains [3]. An example is the molecule 4-Cyano-4′-pentylbiphenyl (5CB) which exhibits a room temperature nematic phase (Figure 1.1) is a prototype system, widely used due to its colourless nature and stability to moisture. Studies on biaxial nematic systems have been gaining importance due to the continuing progress in discovering new system with exciting properties, and their prospected use in faster switchable display devices [5, 6].

1.1 Description of nematic phases

Thermodynamic phases are described by an order parameter field (scalar, vector or tensor) defined at each point of the system. In a homogeneous medium the value of order parameter is the same at all points. Nematic phase is characterized by a non-zero orientational order parameter which vanishes in the isotropic phase. Such a phase is exhibited by elongated (prolate) or flat-shaped (oblate) molecules. This anisotropy at molecular level reflects at the macroscopic phase level also. While defining nematic order from the microscopic level, each constituent molecule is assumed to be rigid and is endowed with some symmetry depending on its structure. Even if the constituents are polar (lack of head-tail symmetry), the liquid crystal medium is observed to be macroscopically apolar, indicating an equal number of molecules pointing up and down with respect to the ordering director; *i.e.*, $\boldsymbol{n} = -\boldsymbol{n}$. Thus the assumption of reflection symmetry about a plane perpendicular to the long axis holds even at the molecular level. The molecules usually have flexible chains or rings that can rotate with respect to each other, but the assumption of a rigid model allows a convenient representation of each of them by a simple unit vector. With respect to a fixed laboratory frame $\{\boldsymbol{e}_X, \boldsymbol{e}_Y, \boldsymbol{e}_Z\}$, any rigid molecule can be described by the three position co-ordinates of its center of mass $\boldsymbol{r}$, and three Euler angles $(\phi, \theta, \psi) \equiv \Omega$ representing its orientation, thereby defining the origin and orientation of a coordinate frame $\{\boldsymbol{e}, \boldsymbol{e}_\perp, \boldsymbol{m}\}$ fixed on the molecule. Here $\boldsymbol{m}$ represents the long axis of the molecule. Let us choose the laboratory $\boldsymbol{e}_Z$ to coincide with the nematic director direction. Due to thermal fluctuations individual molecular orientations deviate from that of the director. For a uniform system, the distribution of centers of mass of molecules in a nematic phase is isotropic in space and hence their position coordinates are irrelevant. If the individual molecules are assumed to have a head-tail symmetry, it is not possible to introduce a vector order parameter analogous to magnetization in ferromagnets. A natural order parameter to describe ordering in nematics thus turns out to be a second rank tensor, which is the next order tensor. The description of the order parameter in the nematic phases is based on the singlet orientational distribution function, $f(\Omega)$ of the constituent

molecules. The probability of finding a molecule having an orientation within the solid angle $\mathrm{d}\Omega$ is given by $f(\Omega)\mathrm{d}\Omega/(8\pi^2)$, which follows the normalization condition, $\int f(\Omega)\mathrm{d}\Omega = \int_0^{2\pi}\mathrm{d}\phi\int_0^{\pi}\sin\theta\,\mathrm{d}\theta\int_0^{2\pi}\mathrm{d}\psi f(\phi,\,\theta,\,\psi) = 8\pi^2$. Depending on the molecular symmetry properties of the constituents which is responsible for the interactions among them, and the given system parameters, a variety of nematic phases are formed.

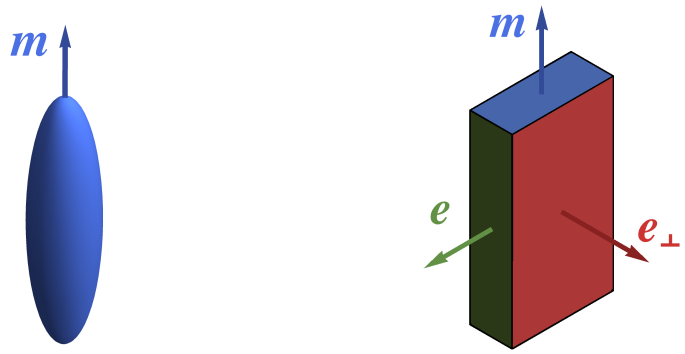

(a) (b)

Figure 1.2: Schematic representation of (a) uniaxial ($D_{\infty h}$) and (b) biaxial (D_{2h}) molecule. $\boldsymbol{m}$ represents the long axis while $\boldsymbol{e}$ and $\boldsymbol{e}_\perp$ represent the short axes of the molecule.

System of $D_{\infty h}$ symmetric molecules

Molecules forming the uniaxial nematic phase have symmetry of ellipsoids of revolution due to fast rotations along their axes of symmetry. Based on whether this axis of rotation is the long or short one, the molecules are distinguished as cylindrical or discotic. A vast majority of molecules forming liquid crystalline phases are approximated to rigid rods with $D_{\infty h}$ symmetry (invariance group of a cylinder) as shown schematically in Figure 1.2 (a), characterized by: (i) an ∞-fold rotation axis C_∞ (long axis of the rod), (ii) infinite number of 2-fold rotation axes C_2 perpendicular to C_∞ and (iii) a mirror plane σ_h perpendicular to C_∞ containing the C_2 axes. C_∞ symmetry implies cylindrical symmetry along the long axis, and this holds due to the fast isotropic rotation of molecules about their long axis. This makes ψ irrelevant, and as the phase is uniaxial, the orientational distribution of molecules is independent of ϕ. Hence, $f(\phi,\,\theta,\,\psi) = f(\theta)$, which can be expanded

in terms of the complete set of Legendre polynomials which reflect the symmetry of both the molecules and the phase as,

$$f(\theta) = \sum_{L=0}^{\infty} a_L P_L(\cos\theta)\,. \tag{1.1}$$

Here we have assumed that the nematic director $\boldsymbol{n}$ coincides with the laboratory $\boldsymbol{e}_Z$ axis. Using the orthogonality relations among $P_L(\cos\theta)$,

$$a_L = \frac{2L+1}{2}\int_0^{\pi} f(\theta) P_L(\cos\theta)\sin\theta \mathrm{d}\theta = (2L+1)\left\langle P_L(\cos\theta)\right\rangle\,, \tag{1.2}$$

where $\langle P_L(\cos\theta)\rangle = \int f(\Omega) P_L(\cos\theta)/(8\pi^2)\mathrm{d}\Omega$.

The coefficients a_L are identified with the order parameters to various degrees but for a possible scale factor. The apolar nature of nematic phase implies that $f(\pi-\theta) = f(\theta)$. Since $\cos(\pi-\theta) = -\cos(\theta)$, $a_L = 0$ for all odd values of L. The first term, $a_0 = 1$ is independent of the orientations of molecules. The next higher term is $a_2 = 5\left\langle P_2(\cos\theta)\right\rangle = 5S$. The scalar S defines the degree of nematic order, and the average is over all molecular orientations (equilibrium ensemble average). The value of S is in the range $[-\frac{1}{2}, 1]$. Its value being 1, 0 and $-\frac{1}{2}$ implies a nematic phase with perfect order, isotropic phase and a state where all the molecules lie perpendicular to the director $\boldsymbol{n}$, respectively. For a nematic liquid crystal like 5CB, typical range of S varies between 0.35 – 0.65 at room temperature [7].

A tensorial order parameter $\mathbf{Q}$ can be defined which includes the information on the nematic director and the scalar order parameter. Expanding the orientational distribution function $f(\theta)$ upto the first non-trivial term,

$$\begin{aligned} f(\theta) &= 1 + \frac{5S}{2}\left[3(\boldsymbol{n}\cdot\boldsymbol{m})^2 - 1\right] = 1 + \frac{5S}{2}\left[3(n_i n_j) - \delta_{ij}\right] m_i m_j \\ &= 1 + 5\, Q_{ij}\, m_i m_j\,, \end{aligned} \tag{1.3}$$

where δ_{ij} is the Kronecker delta and the summation is carried over repeated indices.

$$\mathbf{Q} = \frac{S}{2}\left[3\boldsymbol{n}\otimes\boldsymbol{n} - \mathbf{I}\right], \tag{1.4}$$

where $\mathbf{I}$ is the identity tensor.

Under external influences such as electric and magnetic fields or due to the presence of bounding surfaces, cylindrical symmetry of the phase about the primary director $\boldsymbol{n}$ may be lost. Now $f(\phi,\, \theta,\, \psi) = f(\phi,\, \theta)$, which can be expanded in terms of the complete set of spherical harmonics as,

$$f(\phi,\, \theta) = \sum_{L=0}^{\infty} \sum_{m=-L}^{L} b_{Lm} Y_{Lm}(\theta,\, \phi)\,. \tag{1.5}$$

Orthogonality relation among the spherical harmonics gives,

$$b_{Lm} = \frac{2L+1}{4\pi} \int_0^{2\pi} \mathrm{d}\phi \int_0^{\pi} \sin\theta \,\mathrm{d}\theta\, {Y_{Lm}}^*(\theta,\, \phi) f(\phi,\, \theta) = (2L+1)\, \langle {Y_{Lm}}^*(\theta,\, \phi)\rangle\ . \tag{1.6}$$

This leaves $2L+1$ order parameters for each L. Distribution of long molecular axes is described by order parameters with $m = 0$: $b_{L0} = a_L = (2L+1)\,\langle P_L(\cos\theta)\rangle$. First non-trivial order parameter occurs at $L = 2$. $b_{20} = a_2 = 5S$. Considering a different symmetry of the phase, namely the two mutually perpendicular mirror planes containing the primary director $\boldsymbol{n}$, $f(\pi - \phi,\, \theta) = f(\phi,\, \theta) = f(\pi + \phi,\, \theta)$, the system requires one more order parameter,

$$b_{2-2} = b_{22} = \sqrt{\frac{3}{8}}\, \big\langle \sin^2\theta\, \cos 2\phi \big\rangle = \sqrt{\frac{1}{6}} P\,, \tag{1.7}$$

where P is called the phase biaxiality. It quantifies the lack of rotational symmetry in the distribution of the long molecular axes. The ordering tensor now becomes,

$$\mathbf{Q} = \frac{S}{2}[3\boldsymbol{n} \otimes \boldsymbol{n} - \mathbf{I}] + \frac{P}{2}[\boldsymbol{e}_1 \otimes \boldsymbol{e}_1 - \boldsymbol{e}_2 \otimes \boldsymbol{e}_2]\,, \tag{1.8}$$

where $\boldsymbol{e}_1$ represents the secondary director such that $\{\boldsymbol{e}_1,\, \boldsymbol{e}_2,\, \boldsymbol{n}\}$ forms an orthonormal triad, and $P = (3/2)\,\big\langle \sin^2\theta\, \cos 2\phi \big\rangle$. It is to be noted that the $\boldsymbol{e}_1$-$\boldsymbol{e}_2$ plane coincides with the $\boldsymbol{e}_X$-$\boldsymbol{e}_Y$ plane of the laboratory-fixed frame, even though these axes themselves need not necessarily coincide.

Under the rigid-rod approximation of the molecules, another representation of the microscopic $\mathbf{Q}$ tensor is by Saupe ordering matrix:

$$\mathbf{Q} = \frac{1}{2}[3\,\langle \boldsymbol{m} \otimes \boldsymbol{m} \rangle - \mathbf{I}]\,, \tag{1.9}$$

where the averaging is over all the molecules. $\mathbf{Q}$ is traceless and symmetric and can be diagonalized so as to be represented in its principal eigen frame. The eigen values turn out to be S, $-(S+P)/2$ and $-(S-P)/2$, the corresponding eigen vectors being $\boldsymbol{n}$, $\boldsymbol{e}_1$ and $\boldsymbol{e}_2$, respectively. $P = 0$ for a uniaxial phase, and it takes a nonzero value when the phase is not cylindrically symmetric with respect to the principal director.

System of D_{2h} symmetric molecules

Here the molecules have a reduced symmetry relative to the previous case. They have an inversion symmetry through the center, a 2-fold principal symmetry axis C_2, two 2-fold C_2 symmetry axes orthogonal to the principal axis, a horizontal mirror plane σ_h intersecting the principal symmetry axis, and two vertical mirror planes σ_v aligned with the principal symmetry axis. Such molecules are typically visualized to be lath-like or book-shaped as in Figure 1.2 (b), having a principal long axis and two minor axes which themselves are distinguishable. Despite the asymmetry of molecules, it is possible that the phase is macroscopically uniaxial. Then the orientational distribution function is independent of ϕ and hence $f(\phi,\, \theta,\, \psi) = f(\theta,\, \psi)$. In analogy with equations 1.5 and 1.6, and considering the symmetry of the molecule, $f(\theta,\, \pi - \psi) = f(\theta,\, \psi) = f(\theta,\, \pi + \psi)$ we have,

$$f(\theta,\, \psi) = \sum_{L=0}^{\infty} \sum_{n=-L}^{L} c_{Ln} Y_{Ln}(\theta,\, \psi) \quad ; \quad c_{Ln} = (2L+1)\,\langle {Y_{Ln}}^*(\theta,\, \psi) \rangle \text{ and} \tag{1.10}$$

$$c_{2-2} = c_{22} = \sqrt{\frac{3}{8}}\,\langle \sin^2\theta\, \cos 2\psi \rangle = \sqrt{\frac{1}{6}} D\,. \tag{1.11}$$

The order parameter D is related to the *flatness* of the molecules. A finite D corresponds to a difference in the tendency of the two transverse molecular axes to project on the director, even when the phase is not biaxial. This need not however

imply preference for the minor axes of molecules to be parallel. D vanishes when $S = 1$ as the projections are zero in that case, as well as in the isotropic phase where average projections are similar.

The general and complete expansion of $f(\Omega) = f(\phi,\, \theta,\, \psi)$ is given by,

$$f(\Omega) = \sum_{L=0}^{\infty} \sum_{m=-L}^{L} \sum_{n=-L}^{L} f_{Lmn} \mathcal{D}^{L}_{mn}(\Omega)\,, \tag{1.12}$$

where $\mathcal{D}^{L}_{mn}$ is the Wigner matrix element of the unitary rotation operator $R(\phi,\, \theta,\, \psi)$ on its eigen-subspace with respect to the angular momentum basis $\{|L,\, n\rangle\}$ such that,

$$\mathcal{D}^{L}_{mn}(\Omega) = \langle L,\, m \,|\, R(\phi,\, \theta,\, \psi) \,|\, L,\, n \rangle\ . \tag{1.13}$$

They satisfy the orthogonality relation,

$$f_{Lmn} = \frac{2L+1}{8\pi^2} \int \mathrm{d}\Omega\, {\mathcal{D}^{L}_{mn}}^{*}(\Omega) f(\Omega) = (2L+1) \left\langle {\mathcal{D}^{L}_{mn}}^{*}(\Omega) \right\rangle\ . \tag{1.14}$$

This leaves $(2L+1)^2$ order parameters for each L. The smallest subspace which accommodates the biaxial, uniaxial and isotropic phases is the one with $L = 2$. The head-tail symmetry of molecules, as well as the reflection symmetry of the phase and the molecules, leave behind the following relevant orientational order parameters:

$$\begin{aligned}
\langle \mathcal{D}^{2}_{00} \rangle &= S = \langle R^{2}_{00} \rangle = \frac{1}{2} \langle 3\cos^2\theta - 1 \rangle \\
\mathrm{Re}\left\langle \mathcal{D}^{2}_{0\pm2} \right\rangle &= \frac{D}{\sqrt{6}} = \langle R^{2}_{02} \rangle = \sqrt{\frac{3}{8}} \left\langle \sin^2\theta \cos 2\psi \right\rangle \\
\mathrm{Re}\left\langle \mathcal{D}^{2}_{\pm20} \right\rangle &= \frac{P}{\sqrt{6}} = \langle R^{2}_{20} \rangle = \sqrt{\frac{3}{8}} \left\langle \sin^2\theta \cos 2\phi \right\rangle \\
\mathrm{Re}[\langle \mathcal{D}^{2}_{22} \rangle + \left\langle \mathcal{D}^{2}_{-22} \right\rangle] &= C = \langle 2R^{2}_{22} \rangle = < \frac{1}{2}(1+\cos^2\theta)\cos 2\phi \cos 2\psi \\
&\qquad - \cos\theta \sin 2\theta \sin 2\psi > \ .
\end{aligned} \tag{1.15}$$

Here R^{L}_{mn} are the symmetry adapted combinations of Wigner matrices for D_{2h} group [8] where the orientations are represented with respect to the director frame.

The meaning of first three order parameters are evident from the previous discussion. R^2_{22} or C quantifies the macroscopic biaxial symmetry arising from the molecular biaxiality.

Another representation lending a clearer physical description of these order parameters is accomplished by defining a supertensor [9, 10],

$$\mathcal{S}^{AA'}_{aa'} = \frac{1}{2}\left(3\boldsymbol{a}\otimes\boldsymbol{a}' - \mathbf{I}\right)_{AA'} . \tag{1.16}$$

Here the uppercase letters in the superscript and the lowercase letters in the subscript correspond to the laboratory and molecular axes, respectively. Then,

$$\begin{aligned} S &= \mathcal{S}^{ZZ}_{zz} \\ P &= \mathcal{S}^{XX}_{zz} - \mathcal{S}^{YY}_{zz} \\ D &= \mathcal{S}^{ZZ}_{xx} - \mathcal{S}^{ZZ}_{yy} \\ C &= (\mathcal{S}^{XX}_{xx} - \mathcal{S}^{XX}_{yy}) - (\mathcal{S}^{YY}_{xx} - \mathcal{S}^{YY}_{yy}) . \end{aligned} \tag{1.17}$$

Figure 1.3 shows the snapshots from a lattice-based simulation of isotropic, uniaxial and biaxial nematic phases formed by D_{2h} constituents. The distribution of molecular axes with respect to the laboratory frame is also shown. Orientational order of nematic LCs are experimentally obtained from the manifestations of the non-zero orientational order (S) on the inferences from the birefringence, nuclear magnetic resonance, fluorescence, Raman scattering, small angle x-ray scattering, infrared spectroscopy and infrared dichroism measurements [11, 12].

1.2 Phase transitions in nematics

Detection of a phase transition implies that at least one specific physical quantity differs qualitatively in the two phases, the identification of which is an important step in the description and understanding of the phase transition. Defining the symmetry of a phase as the set of geometrical transformations which leaves the equilibrium configuration of the particles constituting the system unchanged, a

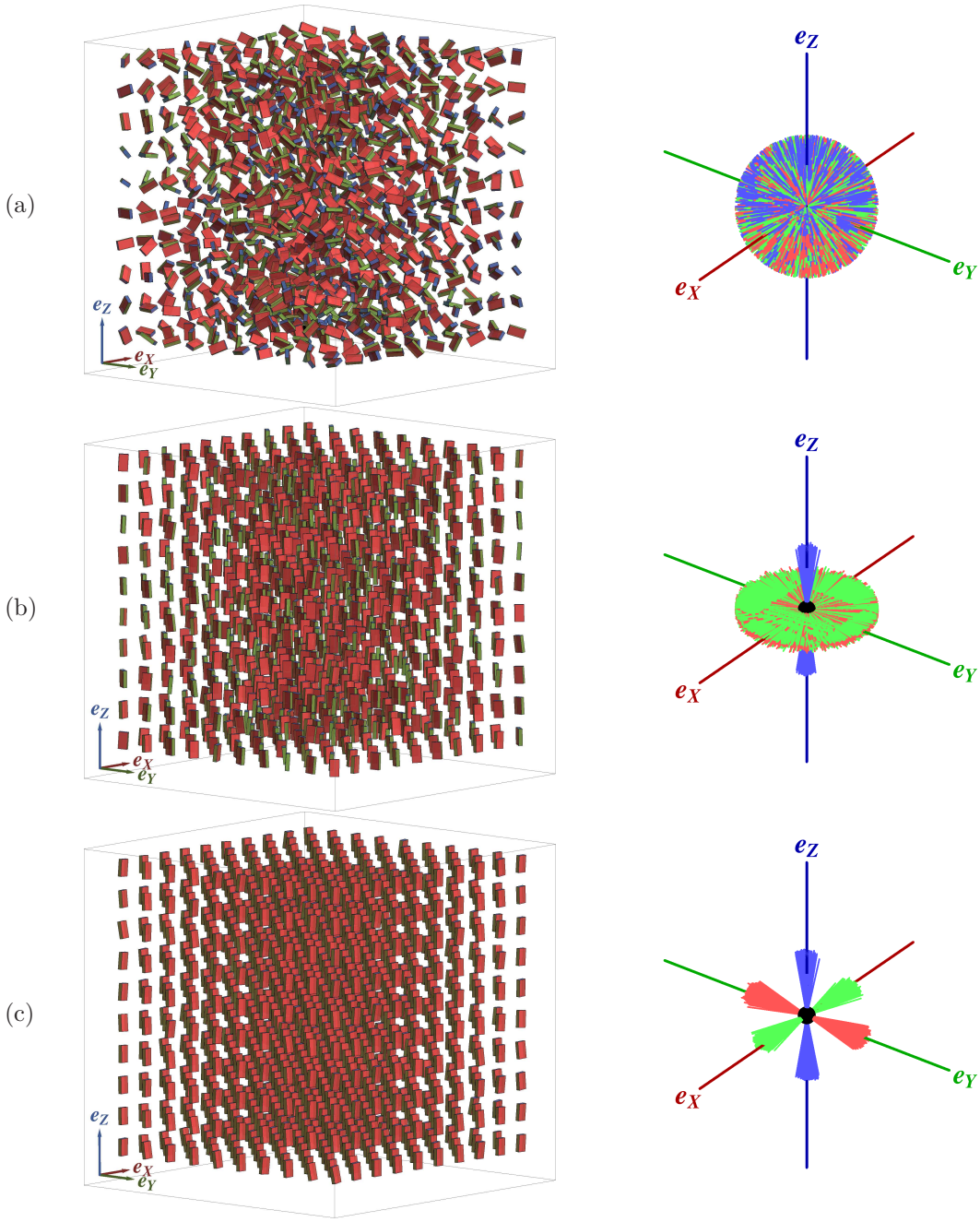

Figure 1.3: Snapshots from the simulation of a system of interacting D_{2h} constituents in (a) isotropic, (b) uniaxial nematic and (c) biaxial nematic phases. Distribution of molecular axes $\boldsymbol{e}$ (red), $\boldsymbol{e}_\perp$ (green) and $\boldsymbol{m}$ (blue) are also shown alongside. In the nematic phases, primary director is along the laboratory axis $\boldsymbol{e}_Z$. Please note the apolar nature of the nematic *spins*.

phase transition typically, but not necessarily involve a change in the symmetry of the system. An order parameter defined to characterize a given transition either could change discontinuously at a first order phase transition (as in the case of a solid to liquid transition), or continuously near a second order one (as for ferromagnetic to paramagnetic transition). A nematic to isotropic (NI) transition is associated with a very small change in the latent heat ($\sim 1.56 \times 10^3$ J/kg [13]) as compared to $\sim 3.34 \times 10^5$ J/kg for a first order transition of ice to water; the NI transition is identified as weakly first order in its nature. It is associated with pretransitional effects on either side of the transition.

1.2.1 Phenomenological Landau-de Gennes theory

Uniaxial constituents

Landau theory of phase transitions is a phenomenological treatment, which assumes that the phase transition in the system, is accompanied by a symmetry change across the transition point, and predicts the consequences through an analysis of the system free energy expanded in terms of its order parameters. The change from the disordered state to an ordered state is thought to be brought about by varying a suitable thermodynamic variable like temperature or pressure (control parameter). Landau theory tries to phenomenologically explain the occurrence of the transition by examining the behaviour of the free energy close to the transition temperature. Phase transition from an isotropic liquid to the nematic LC phase within the framework of the Landau theory was first described by de Gennes, and is usually referred to as Landau-de Gennes theory. Here it is assumed that the order parameter which is spatially invariant and dimensionless has a very small value closer to the transition point. Hence the free energy density can be Taylor-expanded in powers of the order parameter.

$$f(\mathbf{Q}, T) = f_0 + \frac{1}{2}a(T - T_c)Q_{\alpha\beta}Q_{\beta\alpha} - \frac{1}{3}BQ_{\alpha\beta}Q_{\beta\gamma}Q_{\gamma\alpha} + \frac{1}{4}C(Q_{\alpha\beta}Q_{\alpha\beta})^2\,, \quad (1.18)$$

where f_0 is the free energy of the isotropic phase, T is the absolute temperature, T_c is the temperature of the theoretical second order phase transition. Positive

constants a, B and C representing material properties of the nematic medium are assumed to be independent of the temperature. For a typical nematic liquid crystal like 5CB, the range of values for these constants at room temperature are [14]: $a \sim 10^5$ Jm^{-3}K^{-1} and $B \sim C \sim 10^6$ Jm^{-3}. All the terms in equation 1.18 are invariant with respect to arbitrary rotation of the laboratory frame. The second and third order invariants are given by,

$$Q_{\alpha\beta}Q_{\alpha\beta} = \frac{3S^2 + P^2}{2}, \qquad Q_{\alpha\beta}Q_{\beta\gamma}Q_{\gamma\alpha} = \frac{3S}{4}(S^2 - P^2)\,. \tag{1.19}$$

As $\mathrm{Tr}(\mathbf{Q}) = Q_{\alpha\alpha} = 0$ there is no linear invariant, implying that the state of minimum f is that of zero $\mathbf{Q}$ which is the isotropic phase. For uniaxial phase, $P = 0$ and hence equations 1.18 and 1.19 result in,

$$f = f_0 + \frac{3}{4}a(T - T_c)S^2 - \frac{1}{4}BS^3 + \frac{9}{16}CS^4\,. \tag{1.20}$$

Absence of the linear term in S ensures that $S = 0$ is a solution in the high temperature isotropic phase. The term quadratic in S, which is temperature dependent, drives the transition, the cubic term (or any odd powered terms if present) introduces the asymmetry of S and $-S$ states (as opposed to the case in magnetic systems where $B = 0$), and imparts the first order nature to the NI transition. A consequence of this is that the actual phase transition takes place at a temperature T_{NI}, which is (slightly) higher than its (second order) estimate T_c. The first order nature of the free energy pre-empts the progression of the pretransitional phenomena and condenses the system into a nematic phase on cooling the system. The term quartic in S is required to bound the value of f from below in the ordered phase. At equilibrium the free energy density of the system is minimized such that,

$$\frac{\partial f}{\partial S} = 0, \qquad \frac{\partial^2 f}{\partial S^2} > 0\,. \tag{1.21}$$

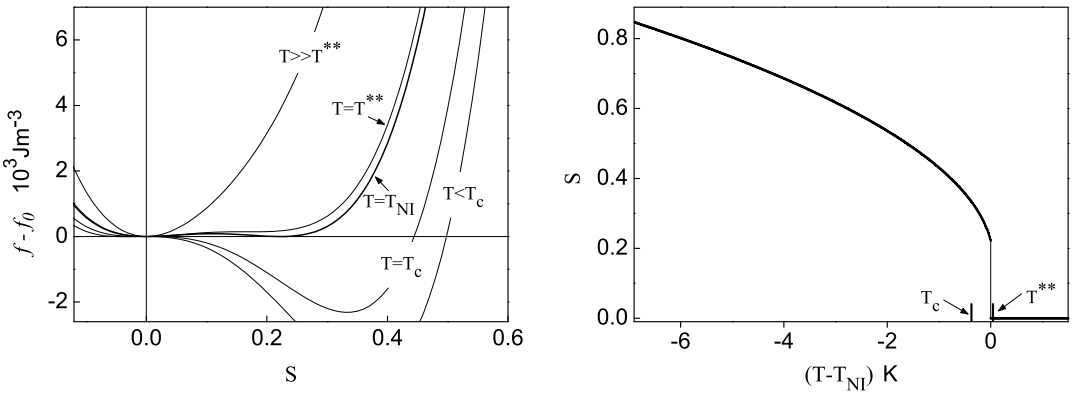

(a) (b)

Figure 1.4: (a) Dependence of free energy density on order parameter over a range of temperatures enveloping NI transition. (b) Temperature dependence of equilibrium order parameter. Temperature corresponding to the supercooling (T_c) and superheating (T^{**}) limits are marked.

This leads to,

$$S = \begin{cases} 0 & \text{if } T > T_{NI}, \\ \dfrac{1}{2}\left[\dfrac{B}{3C} + \sqrt{\left(\dfrac{B}{3C}\right)^2 - \dfrac{8a(T-T_c)}{3C}}\,\right] & \text{if } T < T_{NI}\,. \end{cases} \tag{1.22}$$

As free energies of both the phases are to be equal at the NI transition,

$$S_{NI} = \frac{2B}{9C}\,, \qquad T_{NI} = T_c + \frac{B^2}{27aC}, \qquad T^{**} = T_c + \frac{B^2}{24aC}\,. \tag{1.23}$$

where T^{**} is the absolute limit of superheating of nematic phase where the barrier height in free energy between the ordered and disordered phases vanish, such that $T_c < T_{NI} < T^{**}$. $S_{NI} \sim 0.3$ – 0.4 [7]. Latent heat per unit volume associated with the NI transition is given by,

$$\Delta H = -T\frac{\partial(f-f_0)}{\partial T}\bigg|_{T=T_{NI}} = \frac{3}{4}T_{NI}aS_{NI}^2 = \frac{aB^2T_{NI}}{27C^2}\,. \tag{1.24}$$

Biaxial constituents

Theories on biaxial nematics are still evolving and continuum theory incorporating all the four order parameters defined in section 1.1 describing a biaxial phase is yet to be appreciated. However a two-parameter extension of the Landau theory was given by Gramsbergen *et al.* [15] wherein for the possibility of a biaxial nematic phase, a sixth order term in the order parameter, of the form $\mathrm{Tr}(\mathbf{Q}^3)^2$ with a positive coefficient, is introduced in equation 1.18. The minimization of free energy is carried out with respect to both S and P. The theory predicts a biaxial phase N_B sandwiched between positive (N_U^+ with $B > 0$ for prolate molecules) and negative (N_U^- with $B < 0$ for oblate molecules) uniaxial phases, with a unique point, called the Landau point, where all the four phases (I, N_U^+, N_U^-, N_B) meet. The transitions to N_B phase could be of either type (first or second order), whereas the NI transition line remains first order. Extended studies along these lines have also been reported [16, 17]. Studies based on the two-order parameter tensors [18] and a single biaxial parameter [19] were also reported.

1.2.2 Molecular statistical theories

These theories are based on molecular mean field approach, which assume that each molecule is embedded in a sea of many other molecules, and that each of them experiences the same average potential. In nematics this potential originates from an average orienting field. Initial attempt based on such an approach for uniaxial nematics was due to M. Born [3], where an assembly of liquid crystals interacting *via* their permanent dipole moments was considered. Though it could predict a transition from a high temperature isotropic phase to a low temperature nematic one, its prediction that the ordered phase would be ferroelectric does not agree with the fact that such a phase is apolar even if the constituent molecules are polar. One of the successful theories which describes orientational order and NI phase transition is the Onsager theory based fully on entropic considerations [1]. This assumes the origin of orientational order to be the short range steric interactions. Molecules are considered to be asymmetric with rod shapes where the

only force acting between is steric repulsion that prevents interpenetration. Onsager's approach is based on an exact density expansion of the free energy, and it predicts the formation of an ordered nematic phase, as the density of the rods is increased. The volume fraction Φ occupied by the rods at the transition is $4.5D/L$ and $3.3D/L$ for the isotropic and nematic phases, respectively, which evidently are independent of temperature. The predicted order parameter in the nematic phase at the transition is ~ 0.84 which is rather high. Hence with only excluded volume effects playing a role in the ordering phenomena, the model is athermal and is exact in the limit of infinitely long molecules at extremely low concentrations, and is found applicable in the cases of lyotropic liquid crystals like tobacco mosaic virus, DNA, *etc.*

Maier-Saupe theory for uniaxial nematics

The theory by Maier and Saupe (MS) [20] is the most widely used, based on molecular field approximation and is entirely formulated in terms of anisotropic long-range attractive interactions, with temperature serving as the control parameter. It is based on the following assumptions: (i) each molecule is subjected to an average internal field independent of any local variations or short-range ordering; (ii) unlike the model proposed by Born, here it is assumed that the interactions between permanent dipoles are not particularly important for the orientational order. The interaction is based purely on anisotropic van der Waals forces, or the attractive anisotropic dispersion forces which are second-order perturbation terms of Coulomb interactions, originating from the interaction between momentary induced dipoles of the neighbouring molecules; (iii) further, consistent with the apolar nature and symmetry of the nematic phase which has a cylindrical distribution of oriented molecules about the preferred direction $\boldsymbol{n}$, the constituent molecules are also considered to be apolar and cylindrically symmetric about their long axes; and (iv) the degree of order enters into the potential in a linear way. With these assumptions, the orientation dependent part of the potential energy of the i^{th} molecule is,

$$u_i = -\frac{A_m}{V^2} S \left(\frac{3\cos^2\theta_i - 1}{2} \right) , \tag{1.25}$$

where θ_i is the angle between the long axis of the molecule and the director, V is the molar volume and A_m is a constant. The internal energy per mole is,

$$U = \frac{N_A}{2} \frac{\int_0^\pi u_i \exp(-u_i/k_BT) \sin\theta_i \, \mathrm{d}\theta_i}{\int_0^\pi \exp(-u_i/k_BT) \sin\theta_i \, \mathrm{d}\theta_i} = -\frac{1}{2} N_A k_B T B_m S^2 \,, \tag{1.26}$$

where $B_m = A_m/k_BTV^2$ and N_A is the Avogadro number. The integral in the denominator of equation 1.26 is the partition function, Z_i for a single molecule. Using the expression, $\Sigma = T\partial(\log Z_i)/\partial T$ for entropy, and $F = U - T\Sigma$ for free energy of the system,

$$F = N_A k_B T \left[\frac{B_m S(S+1)}{2} - \log \int_0^\pi \exp\left(\frac{3}{2} B_m S \cos^2\theta_i\right) \sin\theta_i \mathrm{d}\theta_i \right]. \tag{1.27}$$

Dependence of free energy on S at various temperatures obtained from equation 1.27 is shown in Figure 1.5(a). At the transition temperature which is given by $A/k_BT_{NI}V^2 = 4.541$, there occur two minima with equal free energies, signalling a first order phase transition. The temperature dependence of S is shown in Figure 1.5(b), and can be obtained from $S = \langle (3\cos^2\theta_i - 1)/2 \rangle$ using the partition function Z_i, along with the substitutions, $t = \cos\theta_i$, $y = t\sqrt{m}$ and $m = 3A_mS/2k_BTV^2$ as,

$$S = \frac{3}{4m} \left[\frac{e^m \sqrt{m}}{\int_0^m e^{y^2} \mathrm{d}y} - 1 \right] - \frac{1}{2} \,. \tag{1.28}$$

At the transition, $S_{NI} \sim 0.43$ and the order increases continuously as the temperature is further decreased. For $S \lesssim 0.43$ (shown as dashed lines in Figure 1.5(b) which do not correspond to the minimum of free energy) isotropic phase is stable. The theory gives a universal value of S_{NI} for all nematic liquid crystals as there are no parameters in this model that map to any of the material properties. Predictions of this theory are in fair agreement with the experiments, showing that the model captures the most important form of the molecular interactions.

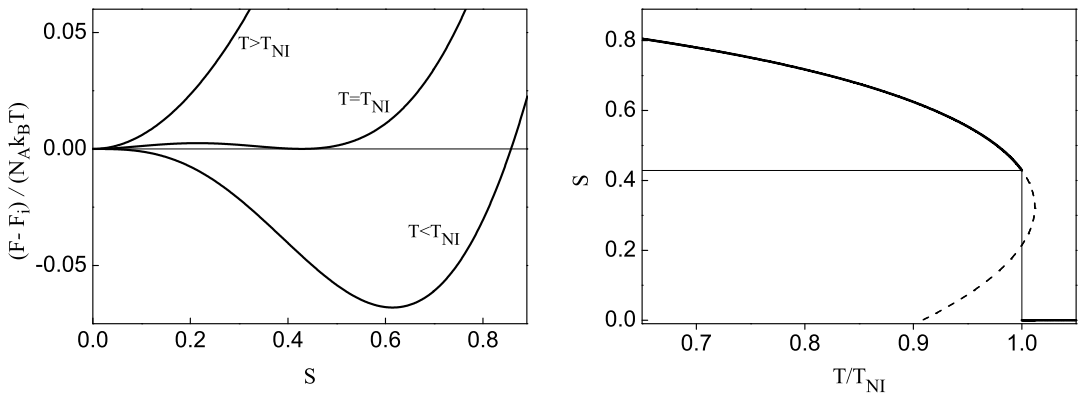

(a) (b)

Figure 1.5: (a) Dependence of free energy density on order parameter at different temperatures, obtained from Maier-Saupe theory. (b) Temperature dependence of equilibrium order parameter.

However the theory is exact in the limit of infinitely long-ranged molecular interactions. It does not consider long wave length orientational fluctuations that diminish the effective order in the system. Minor deviations from the universal behaviour observed in experiments indicate that short-range steric interactions are also important.

Biaxial nematics

In the biaxial nematic phase, orientational correlations between molecules exist not only between their long axes but also among their short axes. The molecular field theory by Maier and Saupe, where the interactions are derived from the lowest order London approximation (considering the multipolar interactions), assumes the molecules to be entities with axial symmetry. A generalization of this approach for elongated, but and flat molecules is given by Freiser [21, 22], by introducing an interaction of a more general angular form, consistent with the pronounced asymmetric structure of the nematogenic molecules. Here two order parameters are used to distinguish the phases and the approach predicts a first order NI transition followed, at a lower temperature, by a second order (or first order with an alternate possibility) transition to a biaxial state. At this second transition the rotation of the molecules along their long molecular axes gets hindered and the mesogens achieve a planar alignment. Shih and Alben [23] studied

a lattice based discrete orientational model of rectangular plates where the mechanism of interactions is steric repulsion which keeps them from overlapping. Plates which are sufficiently asymmetrical (neither square-like nor rod-like) are found to form a phase, characterizing biaxial long range order at high pressure, followed subsequently by uniaxial and isotropic phases at lower pressures. Here the phases are distinguished based on the fraction of molecules with each permissible orientation, which minimizes the free energy. Though the model is a variation of the molecular mean field approximation and hence is prone to an overestimation of the long range order, it is expected to describe some of the features of these ordered phases. The model also predicts a smaller discontinuity in the order parameter at the NI transition for systems with large biaxial steric interactions (and hence large biaxial multipolar interactions). Further calculations based on a mean-field model were carried out, and a comparison with Landau theory was made for a fluid of elongated wide biaxial molecules as a function of effective molecular asymmetry and effective pressure [24], and for a mixture of rod-like and plate-like particles as a function of effective temperature and concentration of the plates [25]. A new subsidiary order parameter (equivalent to D in section 1.1) was also proposed [26] for uniaxial liquid crystals, which was determined and compared with the experimental value obtained from the quadrupole splitting of the magnetic resonance spectrum of partially deuterated samples [27].

A molecular field approximation generalizing the MS theory was proposed by Straley [28], considering an orientational dependent inter-particle potential which has a symmetry appropriate to the interaction between a pair of rectangular blocks. A phase diagram with temperature and shape dependence is obtained alongwith the temperature dependence of the four order parameters identified to describe the ordered phase. Luckhurst *et al.* [29] proposed a theory based on deviations from cylindrical symmetry treated within mean field approximation, using a general expansion of pairwise intermolecular potential for non-cylindrically symmetric molecules, assuming the anisotropic potential to originate solely from dispersion forces. With the deviation from cylindrical symmetry being a parameter at hand, the model predicts improved values for changes in entropy and order parameter at the transition, in accord with the observed values, unlike the case of MS model.

The order parameter D is determined and compared with the experimental values [26] over more data points.

Monte Carlo simulations of lattice system of biaxial particles also predicted the existence of biaxial phases [30–33]. Within the dispersion approximation (a single dipole approximation), Biscarini *et al.* [8] obtained a phase diagram of a collection of interacting biaxial particles as a function of temperature and biaxiality parameter, predicting the temperature dependence of the various order parameters. This study was later followed by a detailed investigation near the tricritical region [34].

Sonnet *et al.* [35] studied a general quadrupolar orientational Hamiltonian for biaxial particles, based on the pair potential proposed by Straley [28] which represents the general nematogenic interaction between molecules with frequency dependent biaxiality. The molecular distribution is assumed to be homogeneous in space and isotropic with respect to the intermolecular vector, for any given relative orientation of the interacting molecules. Each molecule is represented by a parallelopiped with major axis $\boldsymbol{m}$ and minor axes $\boldsymbol{e}$ and $\boldsymbol{e}_\perp$. Any symmetric and traceless tensors with D_{2h} symmetry about the molecular axes $\{\boldsymbol{e},\ \boldsymbol{e}_\perp,\ \boldsymbol{m}\}$, such as molecular polarizability tensor, can be written as linear combinations of traceless orthogonal tensors, (please note a scale factor of $2/3$ compared to the definition in section 1.1)

$$\mathbf{q} = \boldsymbol{m} \otimes \boldsymbol{m} - \frac{1}{3}\mathbf{I}\,, \tag{1.29}$$

$$\mathbf{b} = \boldsymbol{e} \otimes \boldsymbol{e} - \boldsymbol{e}_\perp \otimes \boldsymbol{e}_\perp\,, \tag{1.30}$$

where $\mathbf{I}$ is the identity tensor. $\mathbf{q}$ is uniaxial about the unit vector $\boldsymbol{m}$ in the direction of the long molecular axis, representing dominant geometric feature of molecules, while $\mathbf{b}$ is biaxial representing the molecular biaxiality. These two tensors represent the anisotropic dielectric susceptibilities. The molecules are considered to have been composed of independent oscillators whose fluctuating dipoles resonate at different frequencies. A general quadrupolar orientational interaction energy between two molecules described by a pair of tensors ($\mathbf{q}$, $\mathbf{b}$) and ($\mathbf{q}'$, $\mathbf{b}'$), linear in

each pair of tensors and invariant under their exchange, is given by,

$$H = -U_0\{\xi \mathbf{q}\cdot\mathbf{q}' + \gamma(\mathbf{q}\cdot\mathbf{b}' + \mathbf{b}\cdot\mathbf{q}') + \lambda \mathbf{b}\cdot\mathbf{b}'\}\,. \tag{1.31}$$

$U_0 > 0$ is a scaling interaction energy, whereas ξ, γ and λ are dimensionless parameters. $\gamma = \lambda = 0$ corresponds to the Maier-Saupe potential depending only on the uniaxial molecular components. In the special case of $\lambda = \gamma^2$ the above equation reduces to,

$$V = -U_0(\mathbf{q} + \gamma\mathbf{b})\cdot(\mathbf{q}' + \gamma\mathbf{b}')\,, \tag{1.32}$$

which corresponds to the dispersion approximation [8, 29], where the uniaxial and biaxial polarizabilities are proportional at all frequencies of an applied polarizing field; *i.e.*, the molecules have a single absorption frequency. Hence each fluctuating dipole of a molecule interacts with all induced dipoles of another molecule. The restriction on the ground state of V to be at $(\mathbf{q}, \mathbf{b}) = (\mathbf{q}', \mathbf{b}')$ and on the torque tending to restore the misaligned long axes is larger in comparison to that of the shorter axes, requires γ and λ to satisfy $\lambda > 0$ and $\lambda - |2\gamma| + 1 > 0$. Further symmetries induced by the permutations of the molecular axes and an appropriate rescaling of U_0 implies that all inequivalent interactions are represented by points in the *essential triangle* [36] shown in Figure 1.6 which is represented by $\xi = 1$ in the (γ, λ) space bounded by the lines,

$$\gamma = 0, \quad \lambda = 0, \quad 1 - 2\gamma - 3\lambda = 0\,. \tag{1.33}$$

The point $C_1 \simeq (0,\, 0.20)$ is a tricritical point for the uniaxial to biaxial transition, $C_2 \simeq (0,\, 0.22)$ is a triple point between isotropic, uniaxial and biaxial phases. C_3 is a tricritical point for the isotropic to biaxial transition. Within the triangle, there is a line of tricritical points joining C_1 and C_3 and a line of triple points joining C_2 and C_3. When $\gamma = 0$ the potential is invariant under the $\pi/2$ rotations about $\boldsymbol{m}$ and $\boldsymbol{m}'$ in the individual molecular frame, hence characterizing D_{4h} symmetry. Two independent order tensors $\mathbf{Q}$ and $\mathbf{B}$ are defined as the ensemble averages $\langle\mathbf{q}\rangle$ and $\langle\mathbf{b}\rangle$, respectively. Let the Euler angles $\{\phi, \theta, \psi\}$ represent the rotation of an individual molecule with respect to the laboratory common eigen

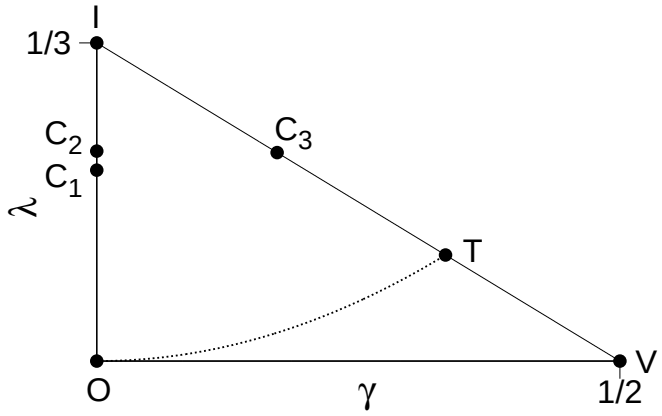

Figure 1.6: Essential triangle with vertices O, I and V having the coordinates (0, 0), (0, $\frac{1}{3}$) and ($\frac{1}{2}$, 0) in the (γ, λ) space. At point T ($\frac{1}{3}$, $\frac{1}{9}$), the dispersion parabola (dashed lines) meets the section IV of the triangle.

frame $\{\boldsymbol{e}_X, \boldsymbol{e}_Y, \boldsymbol{e}_Z\}$ of $\mathbf{Q}$ and $\mathbf{B}$. Then,

$$\boldsymbol{m} = \cos\phi\,\sin\theta\,\boldsymbol{e}_X + \sin\phi\,\sin\theta\,\boldsymbol{e}_Y + \cos\,\theta\,\boldsymbol{e}_Z\,, \tag{1.34}$$

$$\begin{aligned} \boldsymbol{e} \;=\; & (\cos\psi\,\cos\phi\,\cos\theta - \sin\psi\,\sin\phi)\,\boldsymbol{e}_X \\ & +(\cos\psi\,\sin\phi\,\cos\theta + \sin\psi\,\cos\phi)\,\boldsymbol{e}_Y - \cos\psi\,\sin\theta\,\boldsymbol{e}_Z\,, \end{aligned} \tag{1.35}$$

$$\begin{aligned} \boldsymbol{e}_\perp \;=\; & -(\sin\psi\,\cos\phi\,\cos\theta + \cos\psi\,\sin\phi)\,\boldsymbol{e}_X \\ & -(\sin\psi\,\sin\phi\,\cos\theta - \cos\psi\,\cos\phi)\,\mathbf{e}_Y + \sin\psi\,\sin\theta\,\boldsymbol{e}_Z\,. \end{aligned} \tag{1.36}$$

$\mathbf{Q}$ and $\mathbf{B}$ are symmetric traceless tensors; the former representing the contribution to the macroscopic nematic order from molecular long axis,

$$\mathbf{Q} = S\left(\boldsymbol{e}_Z \otimes \boldsymbol{e}_Z - \frac{1}{3}I\right) + P\left(\boldsymbol{e}_X \otimes \mathbf{e}_X - \boldsymbol{e}_Y \otimes \boldsymbol{e}_Y\right)\,. \tag{1.37}$$

The tensor $\mathbf{B}$ describes the macroscopic manifestation of the intrinsic biaxiality of the molecules and is given by,

$$\mathbf{B} = D\left(\boldsymbol{e}_Z \otimes \boldsymbol{e}_Z - \frac{1}{3}I\right) + C(\boldsymbol{e}_X \otimes \boldsymbol{e}_X - \mathbf{e}_Y \otimes \boldsymbol{e}_Y)\,. \tag{1.38}$$

The order parameters S, P, D and C are the order parameters defined in section 1.1, (please note a change in the scale by a factor of 3/2). S and D are

measures of uniaxial order whereas P and C are those of biaxial. When P and C vanish, the above tensors and the phase they describe, are uniaxial without collectively revealing the presence of the intrinsic molecular biaxiality. D corresponds to an anisotropy in the distribution of the short molecular axes. It measures the difference in the degree of alignment of the short molecular axes along the uniaxial director. In a similar way, P represents the lack of cylindrical symmetry in the distribution of the long axis $\boldsymbol{m}$, whereas C represents the contribution to the biaxiality originating from the alignment of the minor axes.

The pseudo potential U of a molecule in the mean field approximation is given by,

$$U = -U_0\{\mathbf{q}\cdot\mathbf{Q} + \gamma(\mathbf{q}\cdot\mathbf{B} + \mathbf{b}\cdot\mathbf{Q}) + \lambda\mathbf{b}\cdot\mathbf{B}\}\,. \tag{1.39}$$

The model predicts a range of parameters where a direct first-order transition occurs between biaxial and isotropic phases, and also a tricritical point in the transition from uniaxial to biaxial phase, where the transition changes from first order to second order. The dependence of this model potential on λ was further investigated to observe another tricritical point by minimizing the free energy minimization with respect to the order parameters [37] and bifurcation analysis [38]. A universal phase diagram was proposed within the mean-field approximation using minimax principle to determine the minimum of the free energy, based on the general Hamiltonian encompassing the model parameter space spanned by the essential triangle [39, 40]. Within the triangle all partly repulsive interactions fall below the dispersion parabola $\lambda < \gamma^2$ whereas the Hamiltonian is fully attractive above it: $\lambda > \gamma^2$. The phase diagram was depicted as a function of parameters λ^* and β^*. Here λ^* parametrizes the arc length along the folded line OIT of the essential triangle (Figure 1.6) in the γ, λ space.

$$\lambda^* = \begin{cases} \lambda \in \left[0,\, \frac{1}{3}\right] & \text{if } \gamma = 0, \\ \frac{1}{3}\left(1 + \sqrt{13}\gamma\right) & \text{if } \gamma = \frac{1}{2}\left(1 - 3\lambda\right) \in \left[0,\, \frac{1}{3}\right]\,. \end{cases} \tag{1.40}$$

The dimensionless temperature $1/\beta^* = k_B T/U^*$ (where $U^* = \frac{2}{3}U(1+3\lambda)$ is determined by the ground state energy of the ordered biaxial phase, where use has been

made of the equalities, $\mathbf{q} \cdot \mathbf{q} = \mathrm{tr}(\mathbf{q}^2) = \frac{2}{3}$ and $\mathbf{b} \cdot \mathbf{b} = \mathrm{tr}(\mathbf{b}^2) = 2$. An experimental realization is predicted for the molecules with fully attractive interactions and the highest transition temperature is attained at the point T in the essential triangle (or its counterparts *via* permutation of axes). The symmetry properties of the Hamiltonian also showed a reduction in the number of order parameters sufficient to describe the stable phases, and studies based on constrained stability analysis within these reduction classes extended the phase diagram along the section TV of the essential triangle, where all the points along this section are found to be Landau triple points facilitating a second order isotropic-biaxial transition [41]. Here it was also noted that this direct transition to the biaxial phase at V is counterintuitive, as the biaxial state is not stable on the γ-axis ($\lambda = 0$) for the interaction Haimiltonian.

Monte Carlo simulations were been performed using the Cartesian representation of the potential in equation 1.39 [42], and in mixtures of rods and discs [43] which reported the possibility of exhibiting a biaxial phase [25]. Here the rods and discs are considered to be of cylindrical symmetry, with their interactions favouring mutually parallel orientation of rods and discs among themselves, and mutually perpendicular orientations between rods and discs. Further studies involved the investigation in the dispersion approximation [44] and on the dependence of the model on the parameter λ [38, 42]. In these calculations, the nature of the order of the transition is inferred to be first order if the observable such as energy and order parameters show a pronounced jump in their values near the transition, with no appreciable size dependence of the system. On the other hand, the second order transitions are characterized by gradual temperature dependence of these observables, along with a pronounced decrease in the order parameters as the system size increases. Increasing number of simulations were also reported on biaxial systems using off-lattice potentials based on Gay-Berne model [45–48] or steric interactions [49, 50]. Bent-core molecules which are prospected candidates for biaxial nematics have been also the subject of recent simulation studies [51–53]. The consistent challenges in realizing spontaneous condensation of these systems in the laboratory, despite many theoretically favourable predictions,

have recently prompted more detailed investigation of the general (lattice) Hamiltonian model with versatile Monte Carlo simulations, attempting to appreciate the role of different interaction terms in mediating the transition to a macroscopic biaxial phase [54].

On the experimental side, the first proof of observation of biaxial phases was reported in a lyotropic ternary system [55] which was followed by studies in nematic liquid crystalline side chain polymers with mesogenic groups laterally attached to the polymer backbone [56, 57]. The occurrence of biaxial nematic phase in single-component thermotropic liquid crystals seem to remain elusive. There have been however recent reports on biaxiality in systems composed of non-linear V-shaped molecules (bent-core) [5, 58–60] and molecular tetrapodes [61–63] are reported using experimental methods such as small angle X-ray scattering, birefringence measurements, conoscopy, dueterium nuclear magnetic resonance and polarizing optical microscopy [64].

In general difficulty in realizing readily biaxial states is attributed to various reasons. It could be due to the thermal fluctuations which prevents the microscopic symmetry from emerging at the macroscopic scale. Such a situation arises when the rotation of a molecule about its long axis is efficient enough to create a rotationally symmetric molecule in effect which replaces the actual flat molecule in its interactions with the neighbours. The non-observance of biaxial phase could also be due to a very narrow temperature range of their stability or due to the possibility of preemption of smectic or crystalline phases or an intervening glassy state in polymers.

1.3 Elasticity and static director deformations

In most practical applications an ideal conformation, where the nematic organizes as a single domain with the molecules aligned along one common director $\boldsymbol{n}$, may not be compatible with the constraints due to surface interactions, influence of external fields *etc.* Deformations to the orientations can occur over space. The

distance over which such deformations occur are much larger (~ 1 μm) compared to the molecular dimensions (~ 2 nm), and hence are usually described by a continuum theory. Within the nematic phase, away from the transition temperature, the order parameter variations do not play an important role and hence only the deformations of the director field, $\boldsymbol{n}(\boldsymbol{r})$ needs to be considered, which itself is assumed to vary slowly and smoothly over distance. Oseen [65], Zocher [66] and Frank [67] introduced a distortion free energy density f_d of a deformed liquid crystal relative to that of uniform orientations, by expanding it in powers of $\nabla \boldsymbol{n}$ [1]. The requirement of apolar nature of the nematic director allows only terms even in $\boldsymbol{n}$. Also, invariance of f_d under rotations implies no terms linear in $\nabla \boldsymbol{n}$. The general form of bulk distortion energy density based on the continuum theory of nematics is,

$$f_d = \frac{1}{2}K_1(\nabla \cdot \boldsymbol{n})^2 + \frac{1}{2}K_2\left[\boldsymbol{n} \cdot (\nabla \times \mathbf{n})\right]^2 + \frac{1}{2}K_3\left[\boldsymbol{n} \times (\nabla \times \boldsymbol{n})\right]^2 . \tag{1.41}$$

The constants $K_i > 0$ are known as Frank elastic constants associated with the three basic modes of deformations in nematic liquid crystals as shown in Figure 1.7: splay (K_1), twist (K_2) and bend (K_3). In 5CB their values are found to be of the order of $\sim$ pN [68] such that $K_3 > K_1 > K_2$, and this relative variation can be qualitatively inferred from the rigid rod models for uniaxial nematics. Twist deformation is always smaller and therefore is favoured, if allowed by the boundary conditions. K_i's decrease with increasing temperature and are taken to be proportional to S^2. The magnitude of distortion energy per molecule is estimated to be much less than the typical interaction energy between the molecules [1], and hence it is inferred that distortions do not modify significantly the phase sequences and order parameter. Usually equation 1.41 is used within the one-constant approximation for elastic constants, such that, $K_1 = K_2 = K_3 = K$. In addition to the afore mentioned contributions to f_d, two more terms which can influence the equilibrium director near the surfaces through boundary conditions are identified as,

$$f_{13} = K_{13}\nabla \cdot \left[\boldsymbol{n}(\nabla \cdot \boldsymbol{n})\right], \tag{1.42}$$

$$f_{24} = -K_{24}\nabla \cdot \left[\boldsymbol{n}(\nabla \cdot \boldsymbol{n}) + \boldsymbol{n} \times (\nabla \times \boldsymbol{n})\right]. \tag{1.43}$$

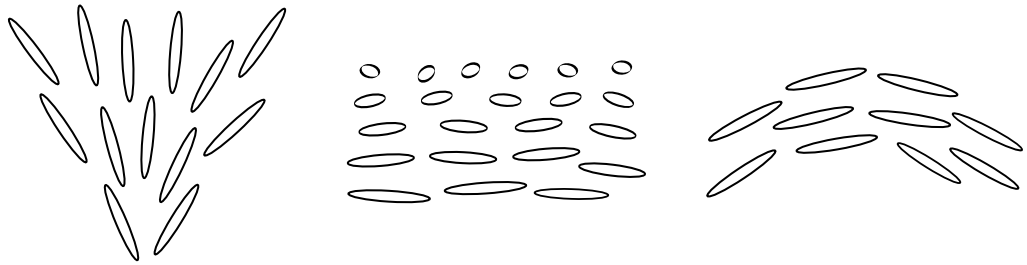

(a) (b) (c)

Figure 1.7: Modes of elastic deformation in nematic liquid crystals: (a) splay, (b) twist and (c) bend.

The contribution f_{13} proposed by Nehring and Saupe [69], which is linear in the second gradient of $\boldsymbol{n}$, is called second order or mixed splay-bend term. The second surface term f_{24} corresponds to saddle-splay deformations and K_{24} is called the saddle-splay constant. By Gauss theorem the volume integrals of these terms become surface integrals and can often be neglected.

1.4 Effect of external fields

1.4.1 Surface fields from external anchoring

For most of the practical applications — scientific or technological — nematic liquid crystals are deliberately confined within boundaries, more often sandwiched between two plates. Due to long range orientational order in nematic liquid crystals, the macroscopic behaviour of such systems is greatly dependent on the orientational alignment of the nematic director imposed by these limiting surfaces, called surface anchoring. This anchoring imparts easy directions (θ_0, ϕ_0) at the interfaces, characterized by surface polar angle θ_s and surface azimuthal angle ϕ_s, by minimizing the surface free energy. With a free boundary or a substrate which is an isotropic medium, all directions in the plane are preferred equally and hence θ_0 alone can define the easy axis. On the other hand, with an anisotropic substrate like a crystal, surfaces rubbed along one direction, or substrates treated

with polyamides, ϕ_0 is also required to define the easy axis. Based on the values of θ_0 the surface alignment of director is termed as homeotropic ($\theta_0 = 0$), tilted ($0 < \theta < \pi/2$) or planar ($\theta_0 = \pi/2$) [70]. In addition to the orientational anchoring effect, variations of the order parameter and the director can also occur near the bounding surface, and the molecules could lose their translational symmetry. However, these variations happen within a very thin layer ($\sim$ 2 nm), which is much smaller than the characteristic length associated with bulk distortions. The energy associated with the distortion is given by [71],

$$f_s = \frac{W'}{2} \left(Q_{\alpha\beta} - Q_{0\alpha\beta}\right)^2 , \tag{1.44}$$

which is the generalization of Rapini-Papoular form [72]. Here W' is the anchoring strength, and $Q_{0\alpha\beta}$ is the surface ordering field with a preferred surface order S_0 and orientation $\boldsymbol{n}_0$. In the limit of non-varying scalar order parameter equation 1.44 becomes,

$$f_s = \frac{9S^2W'}{4} \left[1 - (n_\alpha n_{0\alpha})^2\right] = \frac{W}{2} \left[1 - (\boldsymbol{n} \cdot \boldsymbol{n}_0)^2\right] , \tag{1.45}$$

whose angular dependence is of the Rapini-Papoular form, with $W = 9S^2W'/2$ being the surface anchoring coefficient. W can also be characterized in terms of the extapolation length $b = K/W$ [1], where K is the effective elastic constant. This is done by considering a planar nematic film with a large thickness, d along z direction, with the easy direction at $z = 0$ set by $\theta_0 = 0$. Let the other surface have an infinite anchoring set by an easy direction with non-zero value of θ, thereby introducing a director distortion in the bulk. The total free energy from the bulk and surface contributions is given by,

$$f = \int_0^d \frac{K}{2} \left(\frac{\partial\theta}{\partial z}\right)^2 \mathrm{d}z + \frac{W}{2} \sin^2\theta(0) . \tag{1.46}$$

Here K is the relevant elastic constant depending on the type of deformation. For small deviations from easy direction, $\sin\theta \sim \theta$ holds. At equilibrium f should be a minimum with respect to the profile $\theta(z)$, implying $(\partial\theta/\partial z)$ to be a constant

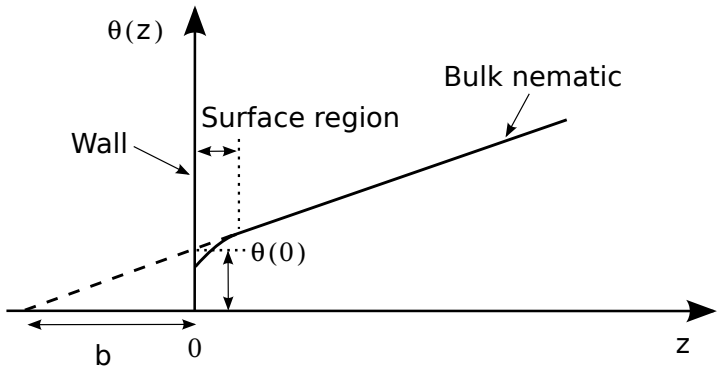

Figure 1.8: Profile of $\theta(z)$ near a surface of the nematic film in the geometrical arrangement set to determine the extrapolation length b.

(giving a uniform distortion of the director in the bulk). Further minimization with respect to $\theta(0)$ yields $\theta(0) = (\partial\theta/\partial z)(K/W)$. From Figure 1.8 the geometrical interpretation of extrapolation length yields $b = K/W$, which ignores the small deviation from the linear behaviour, of the director near the surface. For strong anchoring, where the orientational interaction energy between the liquid crystal molecules and the substrate is comparable to that of the interaction between the liquid crystal molecules, b is of the order of molecular dimension ($\sim$ a few nm). In the case of weak anchoring b can be comparable to the characteristic length of the bulk distortion ($\sim$ a few μm).

1.4.2 Bulk fields

Liquid crystalline materials are mostly made of organic molecules with one or more aromatic rings, and hence are diamagnetic. A magnetic field normal to the plane of the ring builds up a current inside the ring tending to distort and expel the magnetic lines of force thereby increasing the energy. When the field is parallel to the ring no currents are induced and hence the lines of force are least distorted giving rise to a minimum energy configuration. Thus $\chi_{\parallel}$ and $\chi_{\perp}$ are themselves negative and small ($\sim 10^{-6}$ in SI unit convention) whereas $\Delta\chi = \chi_{\parallel} - \chi_{\perp}$ is positive. Here $\chi_{\parallel}$ and $\chi_{\perp}$ are the the eigen values of the susceptibility tensor representing its parallel and perpendicular components respectively, along the symmetric axis (nematic director). When the magnetic field $\boldsymbol{H}$ makes an

arbitrary angle with the nematic director $\boldsymbol{n}$, the magnetization is given by,

$$\boldsymbol{M} = \chi_{\perp}\boldsymbol{H} + \Delta\chi(\boldsymbol{H}\cdot\boldsymbol{n})\boldsymbol{n}\,, \tag{1.47}$$

and the associated magnetization energy contribution to the free energy is given by

$$f_m = -\mu_0\int_0^H \boldsymbol{M}\cdot d\boldsymbol{H} = -\frac{\mu_0}{2}\left[\chi_{\perp}H^2 + \Delta\chi(\boldsymbol{n}\cdot\boldsymbol{H})^2\right]\,. \tag{1.48}$$

The first term on the right hand side of the above equation is independent of the molecular orientation and hence it is the second term that is of interest here (*i.e.*, $-\mu_0\Delta\chi_0 S(\boldsymbol{n}\cdot\boldsymbol{H})^2/2$, where $\Delta\chi_0 = \Delta\chi/S$ is the maximum anisotropy that would be observed for a nematic phase with $S = 1$). It is seen that for $\Delta\chi > 0$ the effect of the $\boldsymbol{H}$ is to align the nematic director along with it thereby reducing the energy. The competing effects of the magnetic field and any other perturbing force on the orientational alignment of a nematic sample can be considered by introducing a length $\xi(H) = \sqrt{\frac{K}{\mu_0\Delta\chi}}/|H|$, the magnetic coherence length which is defined as the distance of a region from perturbing center, at which $\boldsymbol{n}$ is completely reoriented by $\boldsymbol{H}$. $\xi(H)$ is inversely proportional to the applied field. Here K corresponds to the elastic constant representing the director deformation. For a magnetic field of 1 Tesla, $\xi(H) \sim$ a few μm and hence in the usual cells (thickness $d = 5 - 100\,\mu$m) used to study the properties of liquid crystals, $d \gg \xi(H)$. The angle between $\boldsymbol{n}$ and $\boldsymbol{H}$ is seen to decrease at large distances r from the perturbing center, as $\frac{1}{r}\exp[-r/\xi(H)]$. A special case of such an effect is seen by considering a nematic sample between two aligning substrates. For cells with thickness $d \gg \xi(H)$, the application of a field in a direction unfavoured by substrate-aligning direction distorts the nematic medium if $\boldsymbol{H} \geq \boldsymbol{H}_c$, the critical value of field. At this field a phase transition (Fréedericksz) occurs between the unperturbed original configuration and the distorted configuration where the molecules are aligned along $\boldsymbol{H}$ in most of the cell except for the two thin transition regions of thickness $\xi(H)$ near the cell walls. The critical field H_c is inversely proportional to the sample thickness.

An analogous treatment has been used in the electrical properties of the LCs. The measured values of static dielectric constants along ($\epsilon_{\parallel}$) and normal ($\epsilon_{\perp}$) to the

nematic director are different. The dielectric anisotropy ($\Delta\epsilon = \epsilon_{\parallel} - \epsilon_{\perp}$, $\Delta\epsilon_0 = \Delta\epsilon/S$, where $\Delta\epsilon_0$ is the maximal delectric anisotropy) of a rod-like liquid crystal depends on molecular polarizabilities and the angle between the molecular dipole moment and the long axis of the molecule. When this angle is small the material has $\Delta\epsilon > 0$, and $\Delta\epsilon$ is negative when the dipoles are normal to the molecular axis. Such molecular dipoles have their origin from polar groups such as cyano radicals ($-$C≡N). The orientational part of the free energy associated with the electric field applied to a uniaxial dielectric material is $f_{el} = -\frac{\epsilon_0}{2}\Delta\epsilon_0 S(\boldsymbol{n}\cdot\boldsymbol{E}_f)^2$, where ϵ_0 is the permittivity of vacuum and $\boldsymbol{E}_f$ is the electric field. Hence for materials with $\Delta\epsilon > 0$ the effect of $\boldsymbol{E}_f$ is to align the director parallel to it. Similarly, for $\Delta\epsilon < 0$ the free energy is minimized when the director is aligned perpendicular to the field. For a typical liquid crystal material like 5CB, $\Delta\epsilon \sim 11.5$ [73] and can be larger for the ones with stronger dipoles. Akin to the case of magnetic field, the application of an electric field in a direction disfavoured by the substrates of a nematic cell, induces a torque within the sample tending to align the sample director along $\boldsymbol{E}_f$. On the removal of the field the director relaxes to the original direction, which is the working principle of most of the LC-based electro-optic display devices. Again, an electric coherence length is defined by $\xi(E_f) = \sqrt{\frac{K}{\epsilon_0\Delta\epsilon}}/|E_f|$. An electric Fréedericksz transition is induced when $\boldsymbol{E}_f$ is greater than the threshold field. Comparing the contribution to the free energy by electric and magnetic fields, it can be estimated that a magnetic induction of 10 Tesla (which is harder to be achieved continuously in a laboratory) gives the same effect as by an electric field of $10\sqrt{\Delta\chi/\Delta\epsilon}/\sqrt{\mu_0\epsilon_0} \sim 10^6$ V/m which can readily be realized to thin films of thickness $\sim \mu$m. Hence electric fields are more practical in such films to cause reorientations. However, it may be noted that higher electric fields can induce ionic currents, electrohydrodynamic instabilities or flexoelectric effects in the medium while, magnetic fields are free from such effects.

The Landau theory for NI transition in the presence of an external field is presented by Gramsbergen *et al.* [15] where a term linear in the order parameter, of the form, $-Sh/2$ is included in the free energy given in equation 1.18. This term gives the ordering energy of field as mentioned above, and here $h = \mu_0\Delta\chi_0 H^2$ (or $\epsilon_0\Delta\epsilon_0 E_f^2$ as the case may be). The linearity in S inhibits $S = 0$ as a solution which

minimizes the free energy. Hence for $h > 0$ the isotropic phase no more exists and it becomes a paranematic phase with a non-zero degree of order. The transition weakens with an increasing value of h until it vanishes at a critical value of the field where it becomes second order. The transition temperature shifts to higher values and is given by (for the magnetic case) ,

$$\Delta T_{PN} = \frac{3C\mu_0\Delta\chi_0 H^2}{aB}\,, \tag{1.49}$$

and the critical field is given by $H_c = \sqrt{B^3/(162\mu_0\Delta\chi_0 C^2)}$, where a, B and C are the Landau coefficients. Thus the shift is predicted to be quadratic in field. Experimental observations show that these field induced effects are better manifested in rod-like molecules through electric fields [74–77] than magnetic fields [78]. The critical electric field is estimated to be of the order of $\sim 10^7$-10^8 V/m, which are realizable compared to 10^3 T in the case of magnetic field. However more recent works report increased sensitivity to both the fields exhibited by unconventional LC molecules such as bent-core molecules [79–81]. The reason for this behaviour is attributed to the presence of cybotactic clusters of short range positional and orientational order, and the decrease in the value of the Landau coefficient B with a reduced jump in order or latent heat at the transition.

In the case of biaxial nematics the effect of field on the transition to the N_U^+ phase is similar to that of the uniaxial systems [15]. On the other hand, for $B < 0$ the zero field isotropic and N_U^- phases transform under field respectively to a negative paranematic phase (N_p^-) and an induced biaxial phase with a small amount of biaxiality compared to the spontaneously biaxial N_B phase. With increasing field, the first order transition from N_U^- to the induced biaxial phase reaches a tricritical point, the transition remaining second order thereafter. Though the induced and spontaneously biaxial phases remain distinguishable, a sharp transition line between them was not observed. An extended study of this formalism was carried out by Trojanowski *et al.* [17] where it was observed that for positively anisotropic materials the shift in the transition temperature to the biaxial phase could either be positive or negative, being sensitive to the coefficients of the Landau expansion. They had also used a single parameter (dispersion approximation) molecular mean

field approach, and Monte Carlo simulations to study the field effect. An extended study based on molecular mean field theory and Landau free energy analysis was performed on such systems by To *et al.* [19].

1.5 Disclinations in nematics

Other than the possible distortions mentioned in section 1.3 there can be physical situations where **n** is not a smooth function of space co-ordinates. Often in fairly thick cells of nematic liquid crystal, thread-like flexible structures floating freely or attached to the wall are observed under polarizing optical microscope, with or without crossed polarizers. These are due to singularities in the molecular alignment and hence of order parameter, called disclinations [1, 82, 83], around which a symmetry of rotation is broken. When these defects cannot be eliminated by continuous variations of the order parameter, they are called topologically stable or topological defects. The general texture resulting from these singular points is called schlieren texture with dark brushes, which is a signature of a nematic phase. As for most of the condensed matter systems, behaviour of these defects affect the kinetics of phase transitions, the properties of the medium in the ordered phase and its behaviour under external fields. Defects can also arise from constrained geometries. Every defect can be assigned a topological charge which is conserved for a system, analogous to electric charges. The law of conservation of these topological charges controls the creation, annihilation, merging and transformation of these defects. The relatively easier experimental access to study the defects in liquid crystals enables the testing of the theories of topology in physics. Also, the use of these systems as models to study other less accessible systems such as those in the areas of quantum physics, elementary particle physics, cosmology *etc.* is becoming popular and informative [84].

Consider the nematic director to lie in (xy) plane with $\boldsymbol{r}$ being the distance between the singularity and the observation point. Let $\phi(\boldsymbol{r})$ be the angle between $\boldsymbol{r}$ and $x-$axis so that $\tan(\phi) = y/x$, and let the angle between $\boldsymbol{n}$ and x axis be $\theta(\boldsymbol{r})$ (see

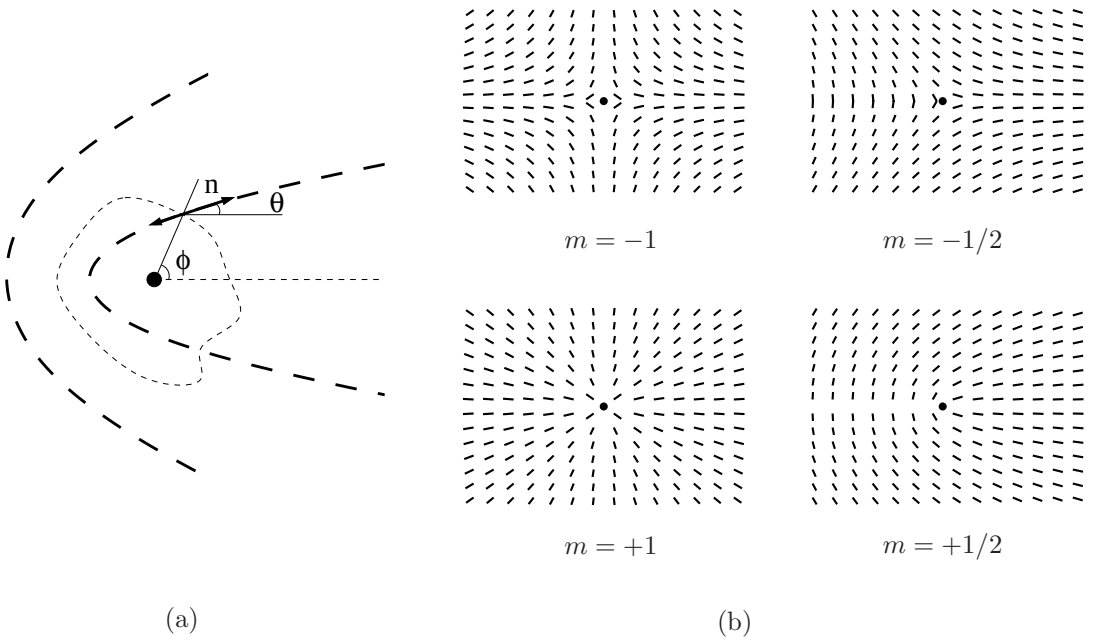

Figure 1.9: (a) Determination of defect strength by traversing along a closed loop encircling the defect core. (b) Director profile near defects of various strengths m generated using equation 1.50.

Figure 1.9(a)). Then the singularity can be quantized as,

$$\theta(\boldsymbol{r}) = m\,\phi(\boldsymbol{r}) + \text{const}\,. \tag{1.50}$$

Following a closed loop around the singular point such that $\Delta\phi = 2\pi$ the director rotates by an amount $\Delta\theta = 2\pi m$, where m can be an integer or a half-integer. m is called the strength of the defect which is a characteristic of each line, and is conserved all along its length. Conventionally a disclination is assigned a sign positive or negative depending on the direction of rotation of the director as one passes in a particular direction along the closed loop enveloping the singularity. In a three dimensional system, these defects can be one-dimensional (points), two-dimensional (lines) or three-dimensional (walls), the latter only possible under strong confinement [85]. Disclination walls are unstable and hence usually line and point disclinations exist in nematics. Defects of half-integer are always lines, and integer ones can be lines or points. In one-constant approximation, the energy

per unit length of line (when the distortion is in a plane perpendicular to the length of the line), also known as the line tension, is given by,

$$F_d = \pi K m^2 \ln\left(\frac{R}{r_c}\right) , \tag{1.51}$$

where K is the elastic constant in one-constant approximation, R is the distance between the line and the boundary (of the order of system size), and r_c is the core radius of the disclination which is of the order of molecular dimensions. Thus most stable planar rotation disclinations are of low strength ($m = \pm 1/2$). Distortions around a line of integral strength may always be continuously transformed into a smooth structure with no singular line. When lateral dimension of the container (R) is sufficiently large, splay-bend deformations with escape into the third dimension are favourable. On the other hand, lines of half-integer strength are stable as there is no way for them to escape into a smooth structure while retaining the same m. The energy of a pair of defects lying at a distance d from one another is $F_d = -2\pi K m_1 m_2 \ln(d/r_c)$. Hence defects with opposite signs of strengths tend to attract and annihilate. The orientational Burger's vector characterizing the disclination, is locally always parallel or anti-parallel to the line in the case of wedge disclinations, and perpendicular in the case of twist disclinations. One of the most common experimental methods used to study defects in liquid crystals is polarizing microscopy, which is simple and reliable. Usually a thin layer of liquid crystal sandwiched between two transparent plates in parallel or wedge geometry is used. Defects are associated with dark extinction bands that cover the regions in which the local optic axis lies in the plane of polarization of either the polarizer or the analyser. As the distribution of the optic axes is associated with that of the axes of molecules (and hence of the order parameter field), distribution of molecules can be determined from the texture observed. In schlieren textures two types of centres from which two or four extinction bands emerge, are observed. The centres with two bands have a singular core corresponding to disclinations of strength $m = \pm 1/2$. The centres with four extinction bands are usually diffusive over distances ~ 1 μm, and correspond to strength $m = \pm 1$. Different

microscopic techniques based on dark-field, phase-contrast, interference and electron microscopy are also used. Dynamic light scattering is a preferred method to measure the mean velocity of the disclinations in the regions of electrohydrodynamic instabilities, derived from the magnitude of Doppler shift in the frequency of reflected light from moving scatterers, the disclinations [83].

1.5.1 Colloidal particles in nematics

Colloidal dispersions with particles ranging from micrometer to nanometer sizes are widespread in the form of emulsions, gels, foams, *etc.* Liquid crystal-colloidal systems are gaining importance in view of their topological interest and photonic applications due to the interesting hierarchical structures formed by them [4, 86, 87]. In a different scenario, liquid crystal nanoparticles are found to be employable in directional drug delivery where monitoring is aided by dye-doped particles [88]. Spatial aggregation of colloids in an isotropic solvent is mediated by interactions of various origins such as electrostatic, dispersive, steric, entropic *etc.* On the other hand a nematic medium has long range orientational order and hence the inclusion of colloidal particles introduces distortion of director field over distances of the order of particle size, due to the interaction with the surfaces of the inclusions. Topological defects can arise under those conditions, or due to constrained geometries imposed by the boundaries. In such cases the ground state of the system can have defect structures in compliance with the topological charge conservation.

When a spherical colloidal particle with rigid homeotropic surface anchoring corresponding to a radial hedgehog of +1 point defect (in three dimensions) is introduced to a nematic cell whose substrates induce a parallel orientation, another compensating defect of the opposite charge is created in the vicinity of the particle [89]. With such a particle in a thick nematic cell, the director deformation corresponds to a hyperbolic hedgehog point defect (also called satellite defect) with a charge of -1, having a symmetry corresponding to that of an electric dipole [89], as shown in Figure 1.10(a). Another compatible defect configuration having higher energy corresponds to a -1/2 wedge disclination loop around the particle (also

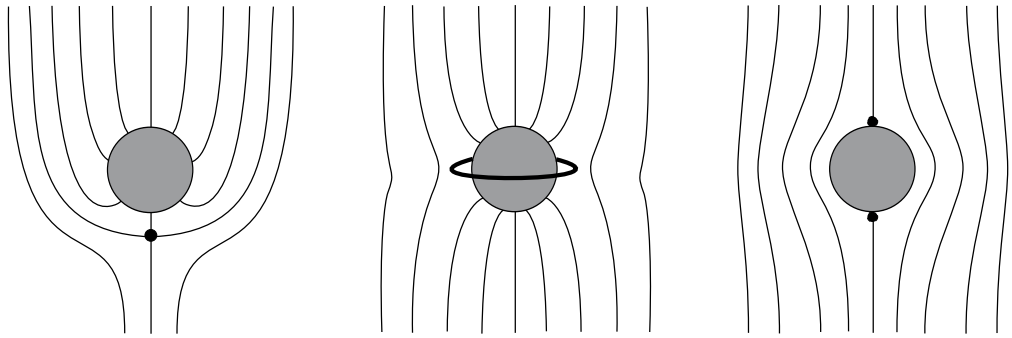

Figure 1.10: Director profile around a colloidal particle in an otherwise uniform nematic. Thick black regions mark the defect region. (a) and (b) respectively show elastic dipolar and quadrupolar configurations formed by a colloid with homeotropic surface anchoring. (c) shows two surface boojum defects formed by a colloid with tangential surface anchoring.

called a Saturn ring) with the symmetry of an electric quadupole [86, 89, 90], as seen in Figure 1.10(b). This can be realized with a stronger confinement and/or a weaker surface anchoring of the particle. A tangential boundary condition on the surface of the colloidal particle, results in a pair of surface defects called boojums with bipolar structure at the poles [90] as shown in Figure 1.10(c).

Macroscopic particles immersed in liquid crystal medium exert long-range forces on each other by distorting order parameter field around them, thereby increasing the orientational elastic energy. Interaction between two such particles originate from the overlap of their director fields, arising from the broken-symmetry nature of nematic elasticity. Interaction between them can be attractive or repulsive depending on the separation of the particles, and angle made by the inter-particle vector with the far field director [89, 91]. This leads to the arrangement of particles into chains, and in favourable circumstances to form colloidal crystals [86].

1.6 Interaction models used in simulations

Computer simulations (described in Chapter 2) using appropriate interacting potentials given by differing microscopic models are of great interest to study the

macroscopic behaviour of the system. In addition to obtaining information on different physical observables, such models are advantageous in extracting a more realistic temperature dependence of the underlying physical phenomenon, through fluctuations which are usually neglected in mean-field or continuum-based approaches. Simulation studies on liquid crystalline systems were initiated by the seminal works of Lebwohl and Lasher [92, 93] (described below) and has been since then used widely to study bulk or confined systems, phase transitions and pretransitional effects [94–104]. More generalized potentials incorporating the unequal nature of elastic constants [105–107] or elongation parameters [108, 109] were also suggested. Simulations using off-lattice [110, 111] and atomistic models [112] are more informative in that they are progressively closer to real LC systems due to the detailed nature of the interactions, leading to their ability to reproduce various phases. Despite their simplicity, lattice-based interaction models are successfully used to capture the orientational phase transitions and other phase properties in uniaxial and biaxial systems. They are also attractive due to lower computational cost, and the relative ease with which they handle larger system sizes. In our studies we use lattice-based models where the nearest neighbour sites on a simple cubic lattice interact *via* orientation-dependent potentials.

Uniaxial interaction

To study systems with uniaxial constituents Lebwohl-Lasher [93] model (which is a lattice discretized version of the Maier-Saupe anisotropic dispersion interaction) is used. Here the nearest neighbour sites interact *via* a second rank pair potential given by,

$$E = -\epsilon \sum_{\langle ij \rangle} P_2(cos\theta_{ij}) \tag{1.52}$$

where ϵ is the positive coupling constant, P_2 is the second rank Legendre polynomial and θ_{ij} is the angle between the spins at i^{th} and j^{th} sites. Here each lattice site is associated with a headless spin which could represent a microcluster of rigid rod-shaped molecules. ϵ (~ 0.023 eV) sets the energy scale and the temperature in reduced units is given by $T^* = k_B T/\epsilon$ where T is the actual sample temperature. The model predicts a weakly first order transition from the isotropic to a nematic

phase at $T^* = 1.1232$ [94] for a bulk system. Correlation and pretransitional studies using this model [94, 98, 113] indicate that the lattice parameter is in the range of a few nm. In the presence of an external field tending to align the long axes of the molecules with the field (positive dielectric anisotropy), the interaction becomes,

$$E = -\epsilon \sum_{\langle ij \rangle} P_2(cos\theta_{ij}) - \epsilon E_a^2 \sum_i P_2(cos\theta_i)\,, \tag{1.53}$$

where, θ_i is the angle between the local director at i^{th} site and the field direction. Comparing the orientational part of the electric field contribution to the free energy density (section 1.4.2), the quantity $E_a^2 = [\epsilon_0 \Delta\epsilon_0 a^3/(3\epsilon)]\, E_f^2$ where, E_f is the magnitude of electric field in V/m. Taking $\Delta\epsilon \sim 10$ and $a \sim 3$ nm, a value of $E_a = 0.1$ corresponds to $E_f \sim 7 \times 10^6$ V/m (or equivalently to ~ 70 Tesla of magnetic induction).

Biaxial interaction

Systems with biaxial constituents are studied using the Cartesian representation of the potential given in equation 1.39 [42],

$$E' = \epsilon\{-G_{33} + 2\gamma(G_{11} - G_{22}) - \lambda[2(G_{11} + G_{22}) - G_{33}]\}\,. \tag{1.54}$$

Here $\{1, 2, 3\} \Rightarrow \{\boldsymbol{e}, \boldsymbol{e}_\perp, \boldsymbol{m}\}$ and $G_{jk} = \mathrm{P}_2(\langle j \,|\, k \rangle)$. $\epsilon > 0$ sets the temperature and energy scales. $|\gamma|$ and $|\lambda|$ are often taken to be smaller than 1. When $\gamma = \lambda = 0$ the potential reduces to Lebwohl-Lasher model. $\lambda = 0$ and $\gamma \neq 0$ is shown to imply an absence of the biaxial order [30]. This model is equivalent to the dispersion approximation [8] with a single parameter λ_d when the parameters are chosen such that $(\gamma, \lambda) = (\sqrt{\frac{2}{3}}\lambda_d, \frac{2}{3}\lambda_d^2)$. Numerous simulation studies have been carried out using this model [40, 42–44, 54, 114]. Details of these lattice models are further developed in the subsequent chapters.

Chapter 2

Monte Carlo techniques for statistical physics

For problems in Physics, exact analytic solutions are impractical whenever one deals with more than two interacting bodies. It becomes very readily quite complex if one were to calculate physical properties of a system of very many particles, equilibrated to the surrounding via energy exchanges. One gets around this issue by determining the thermal average properties (using expectation values) of large many-body systems in a probabilistic approach via the machinery of statistical mechanics. As coined by Gibbs, at thermodynamic equilibrium, the expectation of a quantity O is,

$$\langle O \rangle = \frac{\sum\limits_i O_i e^{-\beta E_i}}{\sum\limits_i e^{-\beta E_i}} \,, \tag{2.1}$$

where the summation is over all possible microstates of the system, and the quantity in the denominator is the partition function, Z. Here E_i is the energy of the system in microstate i and $\beta = 1/k_B T$, where T is the temperature and k_B is the Boltzmann constant. Various physical observables of a system can be derived directly from Z. Except for small systems whose constituents have a simple interaction model with discrete energy spectra, determination of the sum leading to Z becomes difficult as the number of possible available microstates turns out to be enormous. An exact analytic determination of Z is also not practical for most of the models. Simulations based on numerical methods come as an excellent resort under these circumstances, in an attempt to provide closer-to-accurate solutions to problems. Advent of computers and advances in integrated circuit technology in fact stimulated a breakthrough in numerical solutions to problems in diverse areas, within reasonable cost and time. Advantages of such methods are many fold: they act as virtual experiments designed to test a proposed theory, can be performed under various extreme conditions unlike in a real experiment and can

act purely as an exploratory tool. They provide means to determine the macroscopic properties of a system from its microscopic details. Molecular dynamics (MD) and Monte Carlo (MC) techniques [115–119] are two of the widely used computational methods in statistical physics problems. While MD is based on solving Newton's equations of motion, MC is a prescription of sampling configurations from a statistical ensemble. As the name suggests, MC technique extensively uses random numbers and is known to have been employed in its early stages for neutron scattering studies during the second world war. MC methods are also used in diverse fields such as computational biology, weather forecasting, finance and artificial intelligence to name a few. Monte Carlo is a numerical integration tool and uses *the law of large numbers* according to which the determination of a quantity becomes more accurate with the increase in the sample size. According to the *central limit theorem* the error in measurement is proportional to $1/\sqrt{N}$, where N is the number of sampled data points, provided the variance of the data set finite. In MC, an effective way of computing accurate results faster and with reduced variance is by *importance sampling*.

2.1 Metropolis Importance sampling

The objective of important sampling method is to guide the system to sample microstates from a chosen probability distribution. If N microstates are sampled from a probability distribution p then equation 2.1 approximates to,

$$\langle O \rangle = \frac{\sum_{i=1}^{N} O_i \; p_i^{-1} e^{-\beta E_i}}{\sum_{i=1}^{N} p_i^{-1} e^{-\beta E_i}} \,, \tag{2.2}$$

where p_i is the probability of sampling a microstate i. If a particular microstate is chosen with a Boltzmann probability $e^{-\beta E_i}/Z$ then the above equation becomes a simple arithmetic mean,

$$\langle O \rangle = \frac{1}{N} \sum_{i=1}^{N} O_i \,. \tag{2.3}$$

Hence determination of physical observables are made easier, provided the sampling criterion is adequate. Generation of new states in a Monte Carlo procedure is performed via a *Markov process*, wherein a given system in a state i transits to a new state in j without reference to its earlier states. This transition probability $\pi(i \to j)$ which is an element of the stochastic matrix (or Markov matrix) $\boldsymbol{\pi}$, depends only on the properties of the states i and j, and is time independent (homogeneous process). It is chosen such that a long enough Markov chain so generated leads to collection of states with Boltzmann probability, guiding the system to equilibrium. Let $w_i(t)$ be an element of the vector $\mathbf{w(t)}$, representing the probability that the system is in a state i at time t, assuming a continuous time Monte Carlo, such that $\sum_i w_i(t) = 1$. Evolution of $w_i(t)$ is then given by the *Master equation*,

$$\frac{\mathrm{d}w_i(t)}{\mathrm{d}t} = \sum_j \left[w_j(t)\pi(j \to i) - w_i(t)\pi(i \to j) \right] . \tag{2.4}$$

As the system reaches a steady state, the right-hand side of equation 2.4 vanishes leading to constant values of weights thereafter, which represent the equilibrium. If the time steps are measured along the Markov chain, the probability of being in a state j at a time $t + 1$ is given by,

$$w_j(t+1) = \sum_i w_i(t)\, \pi(i \to j) \, . \tag{2.5}$$

$\mathbf{w}(t)$ can be expressed in terms of a basis set comprising the eigen vectors of $\boldsymbol{\pi}$ with appropriate weight coefficients. Repeated application of $\boldsymbol{\pi}$ on $\mathbf{w}(t)$ thus asymptotically tends the Markov chain to equilibration, resulting in the eigen vector of $\boldsymbol{\pi}$ corresponding to its largest eigen value (which is 1), satisfying,

$$\mathbf{w}(\infty) = \boldsymbol{\pi} \cdot \mathbf{w}(\infty) \, . \tag{2.6}$$

Hence as $t \to \infty$ the probability p_i of choosing a state in i corresponds to the desired equilibrium probability,

$$p_i = \lim_{t \to \infty} w_i(t) \, . \tag{2.7}$$

For set parameters of the system, this requires that the Markov processes satisfy the conditions of *detailed balance* and *ergodicity*. Detailed balance demands that in equilibrium the average number of transitions from a state i to any other state j and that of the reverse transitions are equal. *i.e.*,

$$p_i \pi(i \to j) = p_j \pi(j \to i)\,, \tag{2.8}$$

where p_i is the probability of being in a state i. As equilibrium distribution needs to follow Boltzmann probability,

$$\frac{\pi(i \to j)}{\pi(j \to i)} = \frac{p_j}{p_i} = e^{-\beta(E_j - E_i)}\,. \tag{2.9}$$

Transition probability $\pi(i \to j)$ is a product of two factors namely: the selection probability $\alpha(i \to j)$, which is the probability of performing a trial move from state i to j, and the acceptance probability $acc(i \to j)$ of this attempted move. Selection probability is usually symmetric and hence the evolution of Markov chain depends on the choice of the acceptance probability. In compliance with the condition of detailed balance, Metropolis *et al*. [120] proposed,

$$acc(i \to j) = \begin{cases} e^{-\beta(E_j - E_i)} & \text{if } E_i < E_j\ , \\ 1 & \text{otherwise}\ . \end{cases} \tag{2.10}$$

The algorithm is implemented as follows:

Metropolis algorithm:

- From an initial state i generate a new trial state j.
- **if** $E_j \leq E_i$, **then** accept the new state;

  else
  - Generate a random number r such that $0 < r < 1$.
  - **if** $r < e^{-\beta(E_j - Ei)}$, accept the new state.
  - **else** reject the new state, and set i as the next state j.
- Set the accepted new state, j as the initial state for the next iteration (or the same state i if the move is rejected), and repeat the entire process.

Random number sequence used in these computations should not be correlated and are usually sampled from a uniform distribution. In interaction models for liquid crystals (LCs) each lattice site accommodates a freely rotating headless unit vector (LC spin) $\boldsymbol{u}$ denoting the orientation of the local director, and is represented by the polar angle θ and azimuthal angle ϕ with respect to the laboratory frame. A configuration with random orientations of these vectors can be generated by sampling $\cos(\theta_i)$ and ϕ_i from uniform distributions within ranges [-1, 1] and [0, 2π], respectively. The trial move to generate a new state then involves reorientation of these spins using Barker-Watts technique [121]:

Trial move procedure:

- Select an LC spin (this may be done at random or in sequence).
- Randomly select $\cos\delta$ from the interval [-1, 1].
- Select x, y or z axis at random.
- Rotate the selected spin through δ about the chosen axis.

The Markov chain is continued by performing a trial move on the next lattice site. This is repeated till all the N_s lattice sites have participated in a trial move, and is called an MC lattice sweep. With the set parameters of the system, a large number of MC sweeps are done while monitoring energy or other relevant properties of the system, until equilibration is reached. This is followed by a long production run

generating a canonical ensemble of N states, at a given temperature, from whose statistics average properties of system are computed using equation 2.3. Estimate of observables become accurate with more statistics.

Ergodicity demands at least one path of non-zero transition probability between every pair of accessible microstates, as the Markov chain progresses. Metropolis method updates a single spin at a time and hence a state can in principle be reached from any other state after a finite number of successive moves, thus ensuring ergodicity, provided that the transition matrix is irreducible. Another parameter of concern is the acceptance ratio, *i.e.*, the ratio of number of accepted moves to the total number of MC trial moves. A very low value for this means an inefficient and slow sampling in the configuration space, while a value close to one means that all trial states are in the immediate neighbourhood of the initial energy, and hence the sampling is not effective in accessing useful new states, commensurate with the computational effort. We regulate the acceptance ratio dynamically during the simulations to keep it close to 0.5, by controlling the amplitude of the trial reorientational step, δ.

Metropolis sampling method has been used in the area of liquid crystals to study phase transitions [93, 94], films [122, 123], droplets [124, 125], nematic elastomers [126–128], topological defects in nematics [102, 122, 129], biaxial phases [8, 114, 130], *etc*. Even though the algorithm is very elegant, powerful and simple to implement, Metropolis sampling has its disadvantages too. The entire simulation needs to be repeated for any change in the system parameters such as temperature, which is time consuming. Also, the method becomes inefficient near the phase transition regions or while dealing with systems with multiple metastable states.

2.2 Improvements and further evolution of sampling methods

Cluster flipping algorithms

Cluster flipping algorithms were proposed to overcome the disadvantages of single

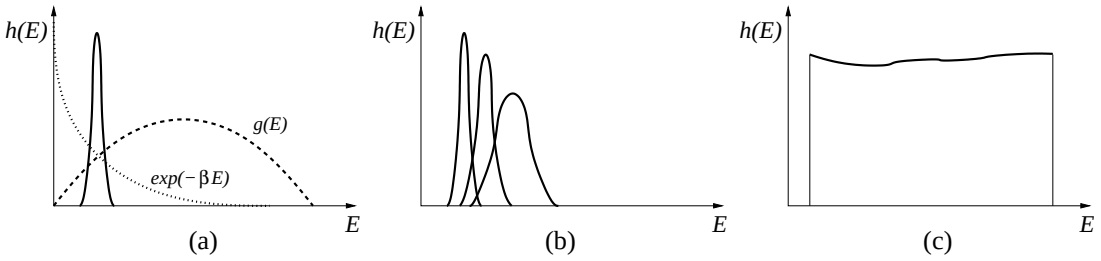

Figure 2.1: Schematic of energy histograms (solid lines) corresponding to the ensemble of states collected during (a) Boltzmann sampling at a given temperature, (b) histogram reweighting method extended to different temperatures, and (c) entropic sampling.

spin flip Boltzmann sampling methods. A major issue near critical regions is the increase in the correlation time resulting in critical slowing down. Single spin flip methods cannot flip over at once, large regions of correlated spins forming domains within the system. Also there is an increased probability of rejecting these moves. Fortuin and Kasteleyn [131, 132] showed that this can be tackled by generating trial states in uncorrelated fashion. The idea was first applied in Monte Carlo methods by Swendsen and Wang [133], known as Swendsen-Wang method. Here bonds are created between lattice sites with certain probability, and clusters are identified and systematically flipped. This was improved in Wolff method [134] which accelerates the process by creating a single cluster and flipping it.

First order transitions show notable hysteresis due to the barrier height which is proportional to the interfacial area between the coexisting phases. The system switches from one to other via a rare interface event. The correlation time here is proportional to the residence time in these phases. This results in super-critical slowing down. The important sampling methods based on Boltzmann probability cannot handle this and urges one to go beyond such methods.

Reweighting methods

Canonical simulations based on Boltzmann probability need to be repeated with every changing parameter of the system such as temperature. It was realized that the distribution of states at a set of state variables can be used to get the system properties at another. Reweighting methods emerged with this idea of determining

system properties from a distribution function in an appropriate ensemble, such as the density of states in the case of canonical ensemble.

Umbrella sampling suggested by Torrie and Valleau [135] is an improvement of *overlapping distribution method* by Bennet [136]. The method enables determination of free energy difference between two systems which differ by a certain parameter, usually referred to as a *reaction coordinate*. Configuration space accessible to both the systems is sampled by modifying the Markov chain through a replacement of the Boltzmann weight factor with a non-negative weight factor which is not known a priori. This in fact is constructed from Boltzmann weights and have an overlap with the equilibrium regions sampled by both the systems. The name of the method comes from this bridging between the configuration spaces, and usually several umbrellas with partially overlapping regions are used. The accuracy of the method is independent of the choice of the umbrella potential, though the efficiency depends on it.

Single histogram method has been successfully applied in the study of critical phenomena [109, 137, 138]. Here a long enough run of Boltzmann simulation performed at a single temperature $T_\circ$ generates a histogram which gives an estimate of the equilibrium probability distribution. The density of states which is independent of temperature can be estimated, for an energy window near the equilibrium energy value corresponding $T_\circ$. Hence the data from a single run can be used to get probability distribution or properties at another temperatures by appropriate reweighting (Figure 2.1 (b)). At sufficiently far away temperatures from $T_\circ$ results become unreliable and also the reliable temperature range gets limited as the system size increases. *Multi-histogram* method which deals with data from more than one value of parameter were efficiently used [139] over a much larger range of temperatures.

The applicable range of temperatures is extended by the introduction of *multicanonical* methods [140, 141]. These were successfully applied in the cases where the probability distributions have multiple maxima (or correspondingly free energy minima) such as Potts model having first order transition [142] and spin

glasses [143]. Using temperature as a dynamical variable *expanded ensemble* methods [144] like *simulated tempering* [145] and its parallel form, *parallel tempering* [146] were successfully employed to study the complicated energy landscapes of spin glasses. Here concurrent simulations are performed to get the properties of the system at a finite number of temperatures. More recent multicanonical methods like *entropic sampling*, where the basic idea is to estimate the density of states, are becoming popular as they can yield system properties at practically any temperature.

2.3 Entropic sampling

Entropic sampling methods [147] evolved with the basic idea of sampling from a distribution other than Boltzmann. The method is being widely accepted due to its simplicity, straightforwardness and potential. Here sampling is done with a probability which biases the random walk according to the inverse of density of states $g(E)$, which itself is not known *a priori*. If the states are sampled such that $p(E) \propto g(E)^{-1}$ then the chances of picking a state within certain energy range is independent of the value of the energy itself. This results in a flat histogram of the energy states visited (Figure 2.1 (c)). Now the condition for detailed balance becomes,

$$\frac{\pi(i \to j)}{\pi(j \to i)} = \frac{p_j}{p_i} = \frac{g(E_i)}{g(E_j)}\,. \tag{2.11}$$

The acceptance probability is,

$$acc(i \to j) = \begin{cases} \frac{g(E_i)}{g(E_j)} & \text{if } g(E_i) < g(E_j), \\ 1 & \text{otherwise}\,. \end{cases} \tag{2.12}$$

As any energy state is equally likely to be selected as any other, the algorithm can cross energy barriers easily, overcoming the problem of quasi-ergodicity experienced by simpler sampling procedures. Here density of states is determined in an adaptive way as follows: $g(E)$ is initially assumed to be of a simple form (usually

a constant) and is computed in an iterative manner as the simulation proceeds. The energy range to be spanned is divided into N_b number of bins and an energy histogram h_k ($k = 1, 2, ... , N_b$) is maintained with its entries being the number of visits to states with energy E_k. The corresponding density of states, g_k, which is initially assumed to be a constant, is updated based on the energy histogram at the end of each iterative run, which consists of certain number of MC sweeps. For the $(n+1)^{\text{th}}$ run,

$$g_k^{n+1} = \begin{cases} g_k^n & \text{if } h_k = 0, \\ g_k^n \; h_k & \text{otherwise}\,. \end{cases} \tag{2.13}$$

The process is repeated until a flat energy histogram is obtained, which is a confirmatory check for the convergence of $g(E)$. This constitutes the 'preliminary run'. As the values of $g(E)$ are usually large and cannot be handled well by computers, often it is preferable to work with its logarithm, $S(E) = k_B \ln g(E)$, in order to avoid numerical inaccuracies. Here $S(E)$ is the microcanonical entropy and it plays an important role here as energy does in Boltzmann sampling. In its initial form the algorithm was expressed in terms of entropy and hence the name. Once we are left with a good estimate of $g(E)$, another long run is performed called the 'production run' collecting an entropic ensemble of N states, of course with an expected flat energy histogram. Now following equation 2.2 determination of any physical observable is rather straight forward,

$$\langle O \rangle = \frac{\sum_{i=1}^{N} O_i \; g(E_i) e^{-\beta E_i}}{\sum_{i=1}^{N} g(E_i) e^{-\beta E_i}}\,. \tag{2.14}$$

Hence the two stages of single simulation leaves behind a good estimate of $g(E)$ and a large set of sample states, from which any useful quantity could be extracted at a later stage, without the need for repeating the entire long simulation. The method permits forthright determination of entropy and free energy of the system (to within an additive constant of course), which are not directly computable using canonical methods. It may be noted that detailed balance is not satisfied in the early stages of the algorithm, but it is recovered as the density of states

converges. Entropic sampling has been successfully employed in the study of Ising systems [148–151], spin glasses [152], natural selection based algorithms for biological evolution [153, 154], *etc.* Despite its triumphs, this method proceeds rather slowly towards the convergence of density of states, and becomes time consuming and less efficient for larger and complex systems, particularly involving continuous variables of the configuration space. This led to further amendments of the method.

2.3.1 Wang-Landau sampling

Wang and Landau [155] ameliorated the above discussed entropic sampling method making it more powerful and efficient. The idea is to update the density of states after each MC step based on a convergence (or modification) factor, f. Here the energy histogram does not actively involve in the updation of $g(E)$, though its flatness is monitored in order to ensure the convergence of $g(E)$. Flatness of energy histogram leads to next iterative run with a modified value of f. This is repeated till $f \to 1$, *i.e.*, when $g(E)$ gets modified no more. Once $g(E)$ estimation is done, the standard procedure follows. Wang-Landau (WL) method is widely employed in the study of 2 and 3 dimensional Ising model and Potts spin models [155–159], 3d lattice and continuous chains of polymers [160–163], quantum systems [164, 165], glassy systems [166], protein folding [167], liquid crystal systems [54, 103, 168–170], off lattice models [171] and generalized reaction coordinates [172].

For interaction models like Heisenberg model or the ones used for liquid crystals, the orientational configuration a single spin can take is continuous in its coordinate space, unlike the discrete ones like Ising spins. The energy spectrum associated with such models is also continuous and this puts forward some concerns, especially for larger system sizes. Spanning the entire range of this continuous energy space for collection of equitably distributed microstates, especially the lower energy ones which are entropically restricted, becomes tedious, if not near impossible within practical timescales of computations. As there are now larger number of accessible energy states, accessing each of these energy bins and updating the corresponding

density of states becomes slower. WL method with further modifications were successfully employed to study LC systems [103], enabling a faster convergence of $g(E)$ and efficient spanning of energy states. The system sizes were still restricted to $N_s \lesssim 2000$. Zhou *et al.* [173] addressed these issues by defining dynamic *frontiers* which distinguishes the energy range over which $g(E)$ has already reached convergence, and those that are away from convergence. A global updation to $g(E)$ is given in the former range, forcing the algorithm to visit states belonging to the latter range. They also proposed a Gaussian kernel-based local updation scheme, wherein $g(E)$ belonging to the nearby bins of the currently accessed one are also updated with appropriate weights, thus enhancing the updation process. This improved method was then applied to obtain 2 dimensional joint density of states $g(E, \eta)$ for Heisenberg model of lattice size $10 \times 10 \times 10$ and protein model with a chain of 30 atoms, where the second reaction coordinate η is magnetization in the former case and end-to-end distance in the latter.

In our simulations of liquid crystal models, in order to go beyond system sizes larger than $12 \times 12 \times 12$, the above mentioned schemes are employed with further modification [174]. Initially the system is prone to access high energy states of lower order due to the larger availability of such states. The initial frontier is thus set in this region where the energy value is typically zero. This frontier is successively shifted towards lower energy regions based on the difference in the values of density of states obtained after successive iterations. It is expected that this difference is nearly uniform for the region where the density of states has already approached convergence, as further updations cannot alter it qualitatively. In order to avoid numerical overflow problems, estimation of density of states is exercised at logarithmic scales in terms of $\alpha_k = \log g_k$ and $\xi_k = \log \alpha_k$ [103, 175], where k represents bin index. Now the acceptance probability of a trial state j generated from an initial state i becomes,

$$acc(i \to j) = \begin{cases} 1 & if\ \xi_j \leq \xi_i, \\ \exp\left[-\exp\left(\xi_j + \log\left\{1 - \exp\left[-\left(\xi_j - \xi_i\right)\right]\right\}\right)\right] & \text{otherwise}, \end{cases} \tag{2.15}$$

where ξ_i and ξ_j are the bin entries of $\xi(E)$ corresponding to the energies of states i and j. After each MC step local updation to ξ is performed as,

$$\xi_k \rightarrow \xi_k + \gamma \exp\left[-\left(\frac{k-k_0}{\delta}\right)^2\right], \tag{2.16}$$

where k_0 is the bin number corresponding to the current state in the Markov chain after the MC step. Here γ sets the amplitude of increment to the bin entry during updation and δ sets the spread of updation to the nearby bins. Their optimum values depend on the system size, number of energy bins and the desired temperature precision. δ is kept constant whereas γ is systematically varied through the simulation from an initially set γ_0.

The simulation procedure is as follows. An initial reference energy bin B_{ref} is chosen in a higher energy region (at energy close to high temperature value, close to zero). Starting from an initial state, a Markov chain of N_{LS} number of MC lattice sweeps, long enough to adequately span the entire energy range involved, are performed following the acceptance criterion in equation 2.15. At the end of each MC lattice sweep, ξ is locally updated as per equation 2.16 and an updation of the histogram is done. After N_{LS} MC sweeps, γ is reduced and the entire process is repeated till the value of γ reaches a preset minimum value. This completes one iteration. For instance, while simulating a Lebwohl-Lasher (LL) [93] system of size $20 \times 20 \times 20$, typical values used are: number of energy bins, $N_b = 10N_s$, $N_{LS} = 3000$, $\delta = 16$, $\gamma = 30$ initially and reduced successively as $\gamma \rightarrow (0.95)\gamma$ till it reaches a value of 10^{-4}. After one iteration, γ is reset to its initial value and a similar second iteration is performed. Now we determine the difference in values of ξ after these iterations. It is assumed that within an energy window of certain width, if ξ has approached convergence, this difference will be fairly constant, as further updations to ξ would increase it only by a constant. Scanning down from the reference bin, an energy frontier is identified at the bin where the difference in ξ is no more within 95% of that of the reference bin, and is set as the next reference bin. This is the flatness criteria to be satisfied to define a new frontier. No new frontier would mean a non-convergence of ξ and hence two more iterations are performed and the flatness criteria is checked again.

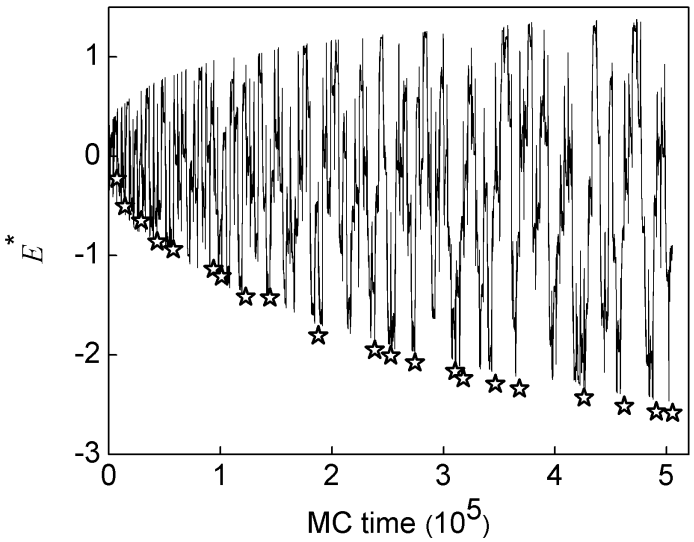

Figure 2.2: Monte Carlo time evolution of the energy (per LC spin) of microstates visited during the frontier sampling stage. Star symbols mark the minimum value of E^* during the introduction of each fresh frontier. The results are for a bulk Lebwohl-Lasher system of size $15 \times 15 \times 15$.

This is repeated till a new frontier is defined. Now ξ values of all the bins above the frontier bin is boosted by a constant. This in effect limits sampling states belonging to the converged ξ region and hence promotes more visits to the lower energy region. Further iterations are done to find a new frontier towards the lower energy region, and the procedure is repeated till the entire admissible energy range is covered. In liquid crystal systems visiting the lowest possible energy region is tedious and hence one is satisfied with a good estimate of ξ up till a lower energy cut-off bin $B_{cut-off}$, if it envelopes the region of interest of the problem studied. Thus one is left with a fairly good estimate to ξ. Figure 2.2 shows the evolution of the energy of microstates visited during the frontier sampling stage, where the MC time at which each new frontier is defined is marked.

In order to further refine ξ, long smoothening iterations are performed with smaller initial value of γ until it is successively reduced to a very small value $\sim 10^{-8}$. This step removes possible discontinuities in ξ resulting in a very good estimate of the density of states. This can also be confirmed by a flat energy histogram during the final stage. Even though a flatness of (80-90)% (meaning that the height of

each bin fluctuates within that amount of the mean height of the histogram) is preferable, this may not be practical, and hence often it suffices that the histogram is reasonable if all its entries are larger than a minimum value. After this confirmation follows a production run. In this step, a long Markov chain is generated using the converged value of ξ, thus performing a uniform walk in energy space. It is to be noted that no updations to ξ are done in this stage. During this walk, an entropic ensemble of typically $\gtrsim 4 \times 10^7$ states is collected, and then their desired properties are recorded. In the following reweighting step, the average of any macroscopic quantity is obtained using a transformed form of equation 2.14 as,

$$\langle O \rangle = \frac{\sum_{i=1}^{N} O_i W_i}{\sum_{i=1}^{N} W_i}\,, \tag{2.17}$$

where,

$$W_i = \begin{cases} \exp\left(\exp\left[\xi_i + \log\left\{1 - \exp\left(-\Delta_1\right)\right\}\right]\right), & \text{where } \Delta_1 = \xi_i - \log\left(\beta E\right) \geq 0, \\ \exp\left(-\exp\left[\log\left(\beta E\right) + \log\left\{1 - \exp\left(-\Delta_2\right)\right\}\right]\right), & \text{where } \Delta_2 = \log\left(\beta E\right) - \xi_i \geq 0\,. \end{cases} \tag{2.18}$$

The entire procedure can be summarized as follows:

Modified WL procedure:

Preliminary estimate of the density of states

1. Initialize: $\xi,\ h,\ \gamma,\ \delta,\ B_{ref}, B_{cut-off}$.
2. Perform an MC step with initial state i and trial state j using the acceptance probability as in equation 2.15.
3. Locally update ξ as in equation 2.16 and h.
4. Repeat steps 2 and 3 to perform N_{LS} number of MC lattice sweeps.
5. Reduce γ: $\gamma \rightarrow (0.95)\gamma$.
6. Repeat steps 4 and 5 till $\gamma \rightarrow 0.0001$. This constitutes an *iteration*. Store the current value of ξ as ξ^1.
7. Perform a second *iteration* and store the resulting ξ as ξ^2
8. Calculate the $\Delta\xi = \xi^2 - \xi^1$ for all bins.
9. Going down from B_{ref}, look for the lowest bin number with $\Delta\xi$ within 95% of that of B_{ref} and set this as the new B_{ref}.
10. If a new B_{ref} is set, globally update ξ by boosting it by a constant for all bins $> B_{ref}$, and proceed to the next step. Otherwise repeat steps 2 - 9.
11. Repeat steps 1 - 10 till $B_{ref} \leq B_{cut-off}$.

Smoothening density of states

1. Set γ to a lower value.
2. Repeat long *iterations* till $\gamma \lesssim 10^{-8}$.
3. Confirm convergence of ξ by monitoring flatness of histogram, h (or by ensuring minimum entries in it).

Generating entropic ensemble

- Generate a long Markov chain using converged value of ξ in equation 2.15 (without doing any updations), collecting the states by recording all its required properties.

Reweighting

- Extract the values of equilibrium physical quantities by reweighting at required temperatures using equation 2.18.

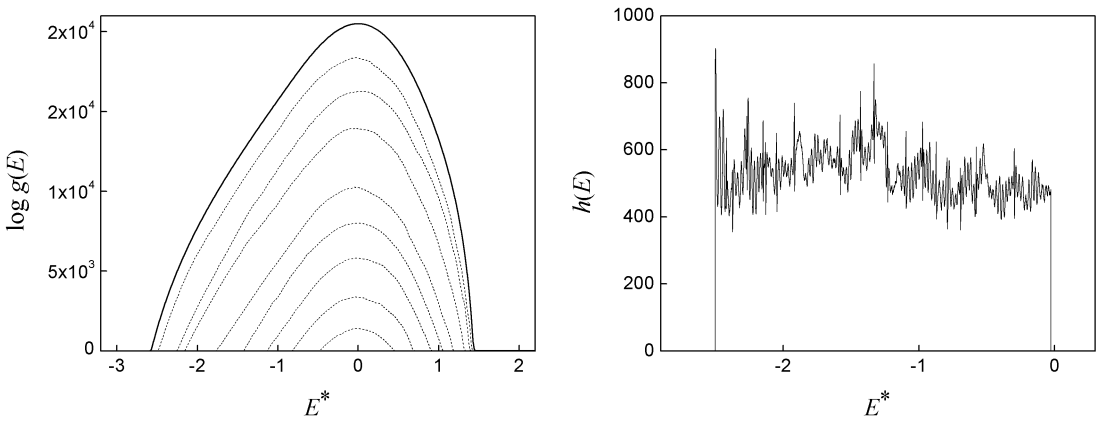

Figure 2.3: (a) Evolution of the density of states (inner dashed lines) until its final best estimation (thick solid line), (b) Histogram of energy (per LC spin) of the states collected in an entropic ensemble. The results are for a bulk Lebwohl-Lasher system of size $20 \times 20 \times 20$.

Figure 2.3 shows the evolution of $\log g(E)$ and the energy histogram of states from an entropic ensemble, performed on a Lebwohl-Lasher system of size $20 \times 20 \times 20$. The modified WL method has been successfuly employed in studying various liquid crystalline systems [54, 169, 170].

2.4 Simulating liquid crystal systems

The lattice models we employ to study liquid crystal systems have characteristic length scales of a few lattice units which translate to a few nanometers. This puts a restriction in simulating systems of sizes proportionate to real ones. The issue gets aggravated when the interactions become complex, or as the sample space become larger. There are however several ways to speed up the computing process itself. Using computing facilities with parallel architectures, jobs may be divided among the processors or each subsystem could be assigned to each processor. This purely depends on the nature of the problem. For instance, in lattice models non-interacting spins can be flipped simultaneously using checkerboard decomposition [117]. Such methods enable easier handling of systems with larger

sizes, or those with more involved calculations, provide faster results and reduce the waiting time to a large extent. In our simulations we employ appropriate parallelization techniques to Boltzmann sampling while simulating systems with complex biaxial interactions (as in Chapter 5) and while dealing with large lattice size used in the colloidal nematic system (as in Chapter 6).

Finite size effects

While simulating bulk systems, it still stays a challenge to obtain accurate measurements at par with the real systems. As opposed to the large numbers of interacting particles in a real system at thermodynamic limit ($\sim 10^{23}$), the maximum number of particles that can be dealt with in simulations using the computational resources so far is of the order of 10^6, which corresponds to nano or submicron regime depending on the characteristic length scales involved. It is still manageable as far as the simulation box is much larger than the correlation length of the interaction model used. But the finite size effects become inevitable and more pronounced near phase transitions as the correlation lengths diverge near critical regions [117]. For a second order phase transition this can be dealt with finite size scaling laws where the system behaviour in thermodynamic limit can be extrapolated from finite sized systems. This is applicable to liquid crystalline systems too as the NI transition is weakly first order in nature and that the transition is driven by pretransitional fluctuations while cooling the system.

Boundary conditions Another matter of concern is the larger surface effects due to small system size, and this raises the issue of the type of boundary conditions that need to be imposed to the simulation box. Periodic boundary condition [117] is a widely accepted one in order to approximate an infinite lattice with a finite lattice, wherein the boundaries of the lattice are effectively eliminated by wrapping them in the form of a torus. This often develops more correlations between the lattice sites, enhances order of the system, decreases the entropy and hence overestimates the transition temperature. Cluster algorithm where the lattice is surrounded by frequently updated ghost environment [176] was proposed to get results from smaller systems, that are comparable to those obtained from larger systems. On the other hand, free boundaries decrease the correlations and hence

has a reverse effect of the periodic ones. We use periodic boundaries for simulating the bulk systems as they are simpler to implement, are quite efficient to mimic an infinite system, and are well accepted. In the case of confined systems the boundaries along one or more directions are represented by fixed ghost LC sites with appropriate anchoring conditions [177].

2.4.1 *In silico* measurement of observables

Energy

Average of energy per spin is represented in its reduced dimensionless form as $\langle E^* \rangle = \langle E \rangle / (N_s \epsilon)$, where averaging is performed over the corresponding ensemble. ϵ is the nearest neighbouring coupling constant and N_s is the total number of spins in the system. In canonical simulations, microstates contributing to the above statistics are considered only after the system is allowed to equilibrate for a sufficiently long time.

Specific heat

Specific heat at constant volume is related to energy as, $C_V = \partial \langle E \rangle / \partial T$. Near a first order phase transition of an infinitely large system, this derivative has a discontinuity and hence specific heat diverges, helping to locate the phase transition. By fluctuation-dissipation theorem, this can be expressed in terms of the variance of energy,

$$C_V = \frac{1}{k_B T^2} \left[\left\langle E^2 \right\rangle - \langle E \rangle^2 \right] . \tag{2.19}$$

In dimensionless form,

$$C_V^* = \frac{C_V}{k_B} = \frac{1}{T^{*2}} \left[\left\langle E^{*2} \right\rangle - \langle E^* \rangle^2 \right] . \tag{2.20}$$

Binder cumulant

Fourth order energy cumulant, introduced by Binder [178, 179] is also used to

identify the phase transition temperature. It is given by,

$$U_4 = 1 - \frac{\langle E^4 \rangle}{3\langle E^2 \rangle^2} \,. \tag{2.21}$$

U_4 is related to *kurtosis*, which measures the $flatness$ of a bell-shaped distribution. At the thermodynamic limit, $U_4 \to 2/3$ for the ordered and disordered phases, and tends to a non-trivial value at the first order phase transition temperature. On the other hand, $U_4 \to 2/3$ at all temperatures, for a system with second order phase transition [137, 179].

Order parameter

Nematic order parameter in its tensor form is represented as,

$$\mathbf{Q} = \frac{1}{2N_s} \sum_{i=1}^{N_s} (3\boldsymbol{u}_i \otimes \boldsymbol{u}_i - \mathbf{I}) \,, \tag{2.22}$$

where $\boldsymbol{u}_i$ is the unit vector representing the spin at i^{th} lattice site. (Please refer to section 1.1 of Chapter 1 for the definition of all the relevant order parameters.) This gives $\mathbf{Q}$ with respect to the laboratory reference frame. In bulk systems without external influences, there exists a degeneracy in the direction of the nematic director and hence $\mathbf{Q}$ is diagonalized and represented in its principal eigen frame, with eigen vectors $\{\boldsymbol{v}_1,\ \boldsymbol{v}_2,\ \boldsymbol{v}_3\}$ and corresponding eigen values $\{e_1,\ e_2,\ e_3\}$, such that $e_1 \geq e_2 \geq e_3$. Now, scalar order parameter representing the degree of orientational order with uniaxial symmetry is calculated as,

$$S = e_1 \,. \tag{2.23}$$

Eigen vector $\boldsymbol{v}_1$ represents the orientation of nematic director. Phase biaxiality parameter which measures the extent of deviation from the uniaxial symmetry of the orientational order (along the director) is,

$$P = e_2 - e_3 \,. \tag{2.24}$$

Order Susceptibility

Order susceptibility χ is related to the S as $\chi = \partial \langle S \rangle / \partial H$ where H is an externally applied ordering field. As in the case of specific heat, zero-field χ can be expressed in dimensionless form in terms of the fluctuations in scalar order parameter as,

$$\chi^* = \frac{1}{T^*} \left[\langle S^2 \rangle - \langle S \rangle^2 \right] . \tag{2.25}$$

Near first order transitions, where the order parameter exhibits a sharp jump, susceptibility shows a notable divergence and hence can locate the transition.

Orientational correlation

The second rank orientational correlation function $G_2(r)$ which gives the correlation between the orientations of two particles separated by a distance r is [94],

$$G_2(r) = \frac{1}{2N_{sr}} \left[3(\boldsymbol{u}_c \cdot \boldsymbol{u}_{ir})^2 - 1 \right] , \tag{2.26}$$

where N_{sr} is the number of lattice spins falling within a spherical shell of certain thickness centered at a chosen lattice site with spin $\boldsymbol{u}_c$, at a distance r/a. $\boldsymbol{u}_{ir}$ represents all the spins within this shell. Usually the procedure repeated by choosing various random sites as center, and by performing yet another average over them. The value of $G_2(r)$ starts from one and decays to $\langle S^2 \rangle$ when the system has a long range order.

Nematic disclination

Disclinations in nematics are regions where nematic director cannot be defined, due to discontinuous orientations of nematic spins. This results in a reduced order in its vicinity. Such regions can be identified by determining an order parameter field $S_i(r)$ from an MC averaged local ordering tensor at every lattice site, $\langle 3\boldsymbol{u}_i \otimes \boldsymbol{u}_i - \mathbf{I} \rangle / 2$, where $\boldsymbol{u}_i$ represents spin unit vectors at each lattice point.

Figure 2.4 shows the above mentioned observables computed for a system with spins of uniaxial symmetry, using LL interaction model.

Orders for systems with biaxially symmetric molecules

For systems where the constituents have biaxial symmetry, each spin is represented

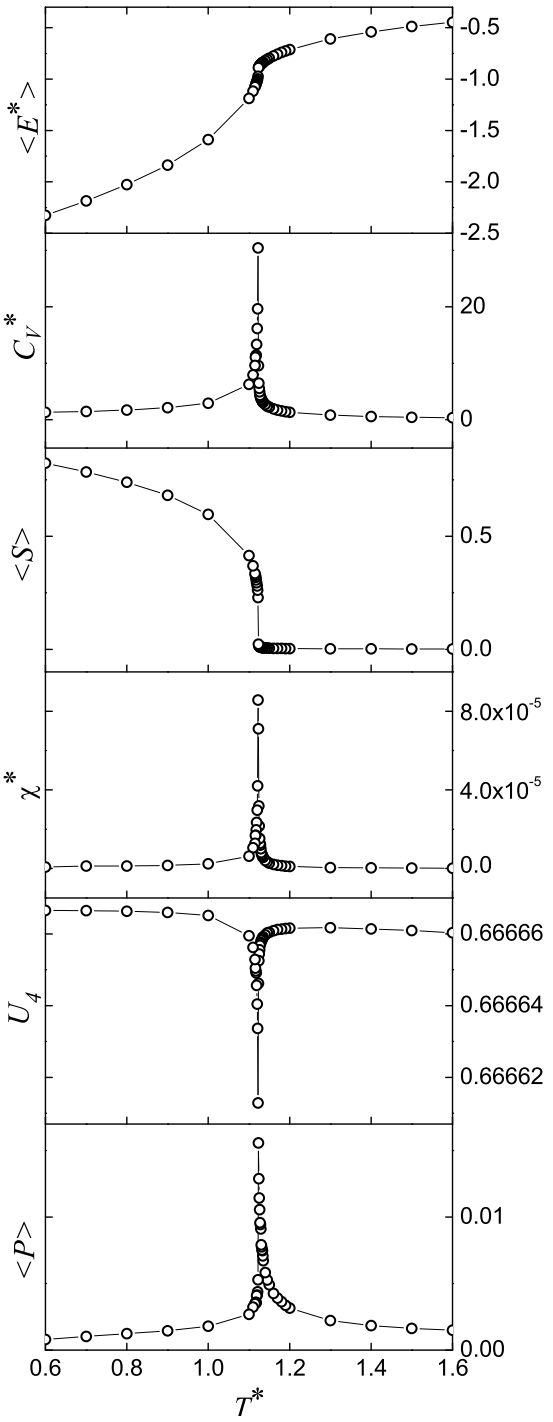

(a)

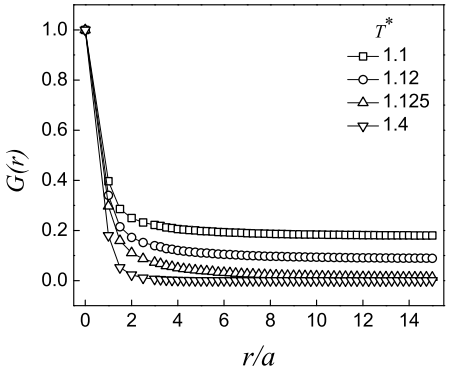

(b)

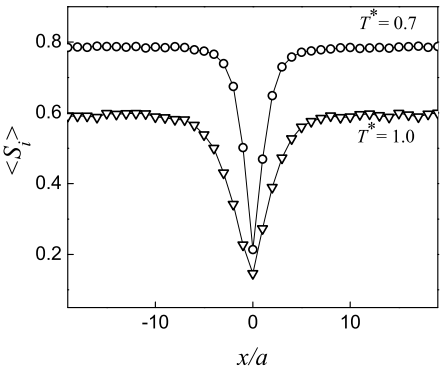

(c)

Figure 2.4: Results from canonical simulations of a Lebwohl-Lasher system. (a) Temperature dependence of various observables for a $100 \times 100 \times 100$ system. (b) Orientational correlations at different temperatures from a $31 \times 31 \times 31$ system. (c) Order parameter profile at different temperatures showing a depression in its value near an $m = -1/2$ disclination in a nematic medium.

by a molecular triad, $\{\mathbf{e}_i^x,\ \mathbf{e}_i^y,\ \mathbf{e}_i^z\}$. Apart from the primary director and its associated order parameter, the system can have two other preferred orientations of the remaining two (minor) axes lying in a plane perpendicular to the global director, with significant ordering along them. Different order parameters can be computed as follows: Corresponding to each vector of the orthonormal triad, three diagonalized ordering tensors $\mathbf{Q}^{xx}$, $\mathbf{Q}^{yy}$ and $\mathbf{Q}^{zz}$ are computed. These tensors are then sorted as $\mathbf{Q}^{max}$, $\mathbf{Q}^{mid}$ and $\mathbf{Q}^{min}$ such that the dominant eigen values of each one of them satisfy $w_1^{max} \geq w_1^{mid} \geq w_1^{min}$, whose eigen vectors are $\boldsymbol{v}_1^{max}$, $\boldsymbol{v}_1^{mid}$ and $\boldsymbol{v}_1^{min}$ respectively. Now $\boldsymbol{v}_1^{max}$ is the principal director and uniaxial order is obtained from the corresponding eigen value.

In order to define the other two axes of the system, from $\boldsymbol{v}_1^{max}$, $\boldsymbol{v}_1^{mid}$ and $\boldsymbol{v}_1^{min}$ a right handed orthonormal triad $\{\boldsymbol{u}^{max},\ \boldsymbol{u}^{mid},\ \boldsymbol{u}^{min}\}$ is constructed via Gram-Schmidt Orthonormalization procedure. This is done starting from $\boldsymbol{u}^{max}$ (which is the unit vector along $\boldsymbol{v}_1^{max}$), then constructing $\boldsymbol{u}^{mid}$ orthonormal to it, and finally $\boldsymbol{u}^{min}$ orthonormal to both of them. This defines the other two axes of the system, $\boldsymbol{u}^{mid}$ being the next relevant one. Computing various order parameters of the system follows. Primary order is given by,

$$R_{00}^2 = S = \frac{3}{2} w_1^{max} \equiv \frac{3}{2} \langle \boldsymbol{v}_1^{max} \mid \mathbf{Q}^{max} \mid \boldsymbol{v}_1^{max} \rangle \ . \tag{2.27}$$

Phase biaxiality is given by,

$$\begin{aligned} R_{20}^2 = \frac{P}{\sqrt{6}} &= \sqrt{\frac{3}{8}} \, (w_2^{max} - w_3^{max}) \\ &\equiv \sqrt{\frac{3}{8}} \Big[\langle \boldsymbol{v}_2^{max} \mid \mathbf{Q}^{max} \mid \boldsymbol{v}_2^{max} \rangle - \langle \boldsymbol{v}_3^{max} \mid \mathbf{Q}^{max} \mid \boldsymbol{v}_3^{max} \rangle \Big] . \end{aligned} \tag{2.28}$$

where w_2^{max} and w_3^{max} are the other two eigen values of $\mathbf{Q}^{max}$ with respective eigen vectors $\boldsymbol{v}_2^{max}$ and $\boldsymbol{v}_3^{max}$ such that $w_2^{max} \geq w_3^{max}$. Molecular biaxiality of the system is given by,

$$R_{02}^2 = \frac{D}{\sqrt{6}} = \sqrt{\frac{3}{8}} \, \Big| \, \big\langle \boldsymbol{u}^{min} \, \big| \, \mathbf{Q}^{min} \, \big| \, \boldsymbol{u}^{min} \big\rangle - \big\langle \boldsymbol{u}^{mid} \, \big| \, \mathbf{Q}^{mid} \, \big| \, \boldsymbol{u}^{mid} \big\rangle \, \Big| \, . \tag{2.29}$$

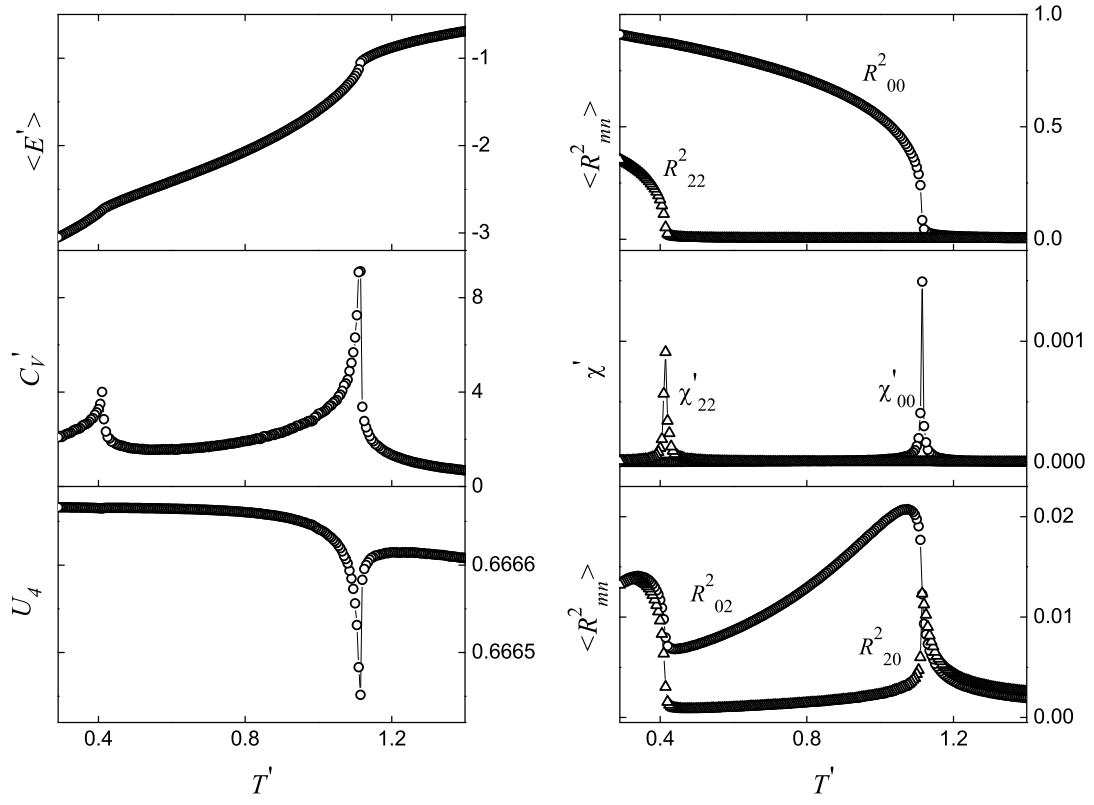

Figure 2.5: Temperature dependence of various observables from canonical simulations performed on a system with biaxial interactions between spins for a $40 \times 40 \times 40$ system.

Macroscopic biaxiality of the system is given by,

$$R^2_{22} = \frac{C}{2} = \frac{1}{4}\Big[\left\langle \boldsymbol{u}^{min} \,\middle|\, \mathbf{Q}^{min} \,\middle|\, \boldsymbol{u}^{min} \right\rangle + \left\langle \boldsymbol{u}^{mid} \,\middle|\, \mathbf{Q}^{mid} \,\middle|\, \boldsymbol{u}^{mid} \right\rangle - \left\langle \boldsymbol{u}^{min} \,\middle|\, \mathbf{Q}^{mid} \,\middle|\, \boldsymbol{u}^{min} \right\rangle - \left\langle \boldsymbol{u}^{mid} \,\middle|\, \mathbf{Q}^{min} \,\middle|\, \boldsymbol{u}^{mid} \right\rangle \Big]. \tag{2.30}$$

R^2_{22} is scaled to fall in the range [0, 0.5], a value of 0.5 denoting maximum biaxiality in the system. Order susceptibilities can be computed in a similar manner as that for the uniaxial case. Figure 2.5 shows some of the observables obtained from canonical simulations for a system with biaxially symmetric spins [35] at chosen biaxial Hamiltonian parameters. As the system is cooled from the isotropic phase, initially a transition to uniaxial nematic phase N_U and then to a biaxial phase N_B is seen.

Chapter 3

Nematic films and order parameter-based sampling

Nematic films are the most studied amongst confined liquid crystal systems [180] because of their simpler geometry for experiments and applicability in the display devices. They are suitable for studying anchoring effects of substrates and elasticity of the medium. Films with agreeable, hybrid or conflicting anchoring at both the substrates come into use for different applications. Experimental and numerical studies with appropriate models and simulation techniques have been employed widely to study planar nematic films [100, 181–194] and nematic medium confined to cylindrical [195–201], spherical [124, 125, 202–206] or porous [109, 207–209] surfaces. Amongst the Monte Carlo methods used for LC systems, widest employed is the Metropolis importance sampling [120]. For its simple use to construct canonical ensembles, the size of system is not a constraint, and the algorithm can be optimized catering to the size of the system and nature of the interaction, which typically is the case with systems having continuous degrees of freedom, such as Lebwohl-Lasher (LL) [93] model. Such continuous configuration variables of course place severe restrictions on the sizes of the systems that need to be studied when one has to carry out entropic sampling procedure. Confined systems in this respect are more amenable for detailed study based on these more informative simulations. In this chapter we report our studies on an interesting director structure observed in a simple planar nematic film anchored homeotropically at both the substrates. This is in addition to the stable homogeneous one expected, corresponding to the absolute free energy minimum. A detailed investigation of these structures using canonical sampling method is initially discussed, followed by an energy-based entropic sampling study. The nature of the unusual director structure necessitated the exploration of the configuration space of the system based on its order parameter, which resulted in the development of a new sampling method, facilitating a uniform random walk along the order parameter axis

– OP-sampling. The method is an algorithmic adaptation of the energy-based entropic sampling method, providing a representative distribution of microstates with respect to the order parameter within a thin energy sheet (a good approximation to a microcanonical ensemble). We report some interesting manifestations of this simple homeotropic film based on this sampling procedure.

3.1 Canonical sampling

The simulation box is simple cubic having l lattice units along either of the lateral directions (say, x- and y- directions) with periodic boundaries, and a thickness of d lattice units along the z-direction, resulting in $N_s = l \times l \times d$ number of interacting LC molecules represented by headless "spins". This is exclusive of the additional layers with fixed LC spins, each beyond $z = 0$ and $z = d$ of the film, representing substrates favouring strong homeotropic alignment. They are realized by fixed unit vectors at their sites oriented along the z-direction. In most of our simulations $l = 8$ and $d = 40$, unless specified otherwise. We have also varied l and d to study the system size dependence on the observed phenomena. Canonical simulations based on Metropolis sampling [120] is performed assuming the LL interaction. It may be noted that a 3-d LL model has a reported clearing temperature (in reduced units) at $T^*_{NI} \sim 1.1232$ [94] and lattice parameter $a \sim$ a few nm [98, 113]. Initially the spins are chosen to be randomly oriented. The temperature is then set to a very low value of $T^* = 0.01$ and the system is allowed to evolve towards an equilibrium state, guided by the Metropolis algorithm. We repeated this experiment with several random seeds for the choice of the initial random configuration, trying to examine if the system anneals to different topologically different structures. The most probable configuration corresponds to the absolute minimum of the free energy, resulting in a uniform homeotropic alignment of the LC spins. Contrary to this expectation, with a lesser probability the system indeed condenses into yet another configuration, qualitatively different from the more familiar one. We call the homeotropically aligned film with bulk value of a high uniaxial order (≈ 0.99 consistent with the low temperature) as film A. The second director structure inti

which we find this film to be condensing is associated with a low bulk value of the order (≈ 0.26), resulting from the tilted director structure of the film. The tilt occurs normal to the substrate into the xy-plane. We refer to this as film B. Snapshots of the microstates of these films, with 3d ellipsoids mimicking the LL spins are shown in Figure 3.1.

We carried out MC simulations starting with these two distinct structures (at $T^* = 0.01$), and obtained observable physical properties as averages over equilibrated ensembles, constructed through the Metropolis algorithm. The equilibration and production runs are carried out over 5×10^6 MC sweeps, and the temperature is varied in steps of 0.01.

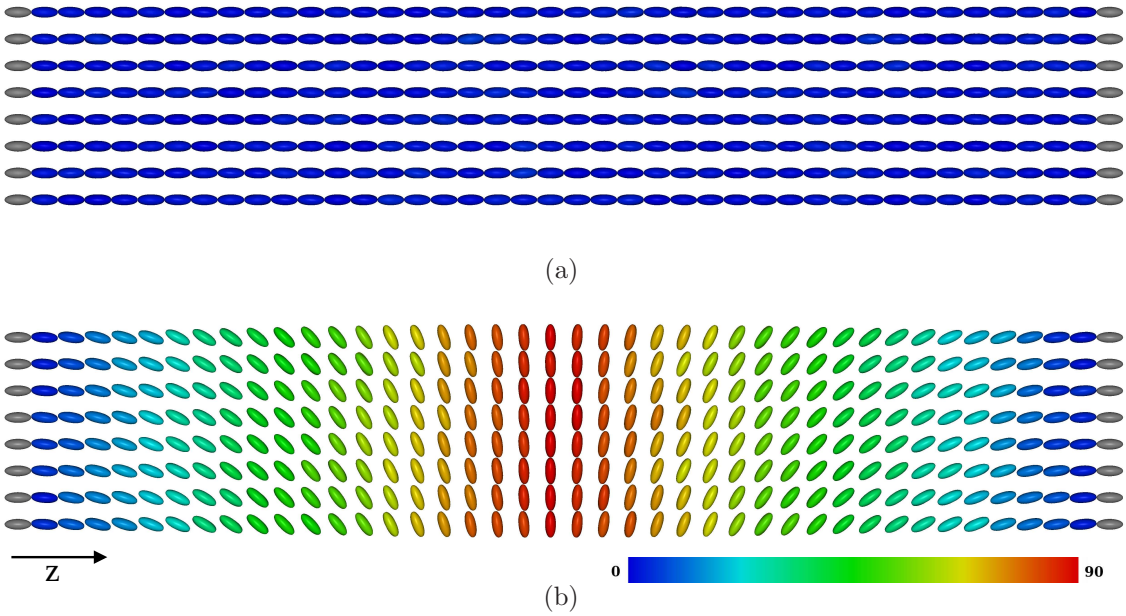

Figure 3.1: Snapshots of the system at $T^* = 0.01$ for film A with $S = 0.9974$ (a) and film B with $S = 0.2648$ (b). Right most and left most grey layers represent the substrates. Colour map is a guide to the relative orientation of the LC spins with respect to the z - axis (polar/zenithal angle). Due to the reduced fluctuations at this temperature, orientation of LC sites of other lateral layers are not visible in the figure, viewed along one of the edges of the simulation box.

Director structure similar to film B is experimentally observed in homeotropic

LC films [210] as a metastable state during the initial cell filling, the reason being the flow influenced rearrangement of aligning monolayers near the substrates, which later transforms to the more stable homeotropic one over the period of time. Such metastable structures are also predicted by continuum-based studies on flow phenomena in liquid crystals [211]. Theoretical calculations predict other forms of director deformations in very thin nematic cells when splay-bend elastic constant is strong [212, 213]. This indeed is not the case in this study as the interaction model used here has an isotropic elastic constant [96, 98]. Director distortions can arise also due to the collective behaviour of the nematic medium resulting in electric, magnetic [1, 214–218] or optical [219–221] Fréedericksz transition, wherein a corresponding external field of sufficient strength opposing the substrate anchoring is applied. This phenomenon is widely used for controlling the birefringence of the nematic films, providing the ON/OFF states required for the display devices. However such director distortions are topologically distinct from that in Figure 3.1(b) as will be discussed later in *Discussion* section. Field-induced transient [222, 223] or ground states [224] with periodic stripes are also seen in nematic systems. Simulations on confined systems using the LL interaction have shown the occurrence of different possible director configurations (which are predicted and allowed by continuum-based elastic theory) depending on the rate at which the system is cooled [225]. In all the above cases the distorted director structure arises from an external stimuli, whereas in our case the structure B forms apparently spontaneously. At the same time, we take cognizance of the dependence on the initial random configuration which could set in the nucleation of the director structure of film B.

On heating, a system evolving through the set of microstates compatible with the film B suddenly merges with that of film A at a temperature $T^*_m = 0.97 < T^*_{NI}$, where T^*_{NI} is the nematic-isotropic transition temperature. The film B appears to be stable through the production run until the merging happens. The temperature dependence of various observables of the film are shown in Figure 3.2. The average energy per LC spin ($\langle E^* \rangle$) and specific heat (C_V) of film B are seen to be slightly higher than that of A until they merge (as is discussed below), though it is not so much evident from Figure 3.2. A clearly distinct order parameter profile shows

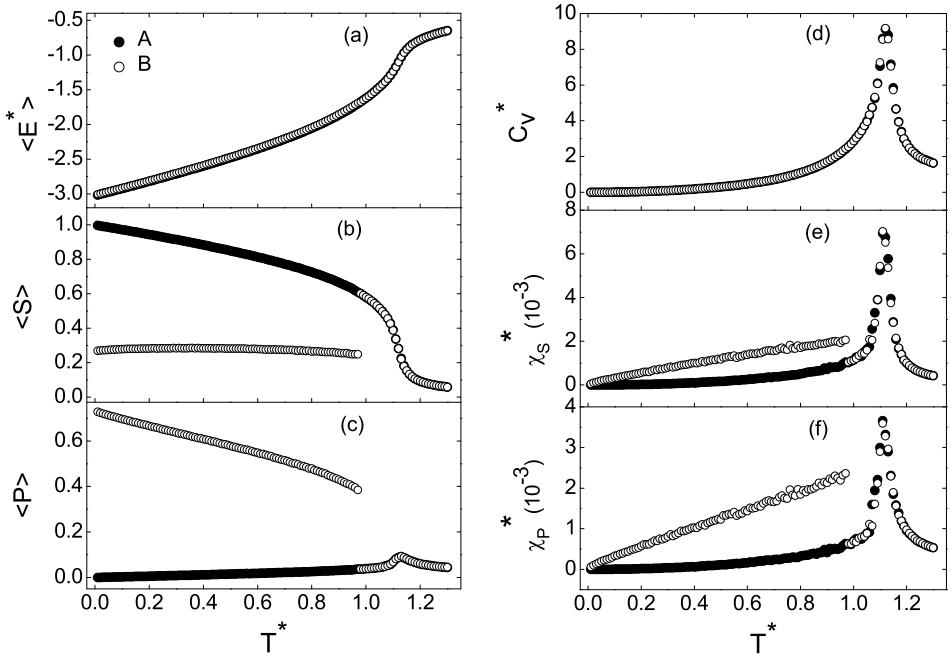

Figure 3.2: Temperature dependence of various macroscopic observables obtained from Boltzmann sampling. Filled circles represent the data for film A and the empty ones for film B.

that the film B has a lower value of S, which is a consequence of the tilt in its layers (geometrical average over the entire film). This is supported by the complementary behaviour of the phase biaxiality, P. A relatively higher susceptibility of order, χ_S for film B points to larger fluctuations in S indicating a larger range of S values accessed by these configurations, this is also deducible from the fluctuations in P. Unequal energies of the structures is more evident in Figure 3.3 where the difference in their total average energies, $\Delta E^*_{AB} = \langle E^*_B \rangle - \langle E^*_A \rangle$, is shown. (Please note that $\langle E^*_A \rangle$ or $\langle E^*_B \rangle$ represents the total mean energy from all the N_s LC spins.) This difference is $\sim$ 20 units (*i.e.*, $\sim$ 0.0078 per particle) at lower temperatures and increases as the merging temperature $T^*_m \sim 0.97$ is approached, and thereafter vanishes through T^*_{NI}. It can be seen that at lower temperatures the energy fluctuations ($\sigma_A/2$ or $\sigma_B/2$) are smaller than ΔE^*_{AB} thereby restricting a transition from one to the other. For $T^* > 0.81$ the fluctuations are relatively higher and one can expect a transition from film B to film A to occur (merging) above this temperature value. The inset of Figure 3.3 shows that $\sigma_B - \sigma_A$ (which is related to the specific heat by fluctuation dissipation theorem as, $\sigma^2 = C_V T^{*2}$)

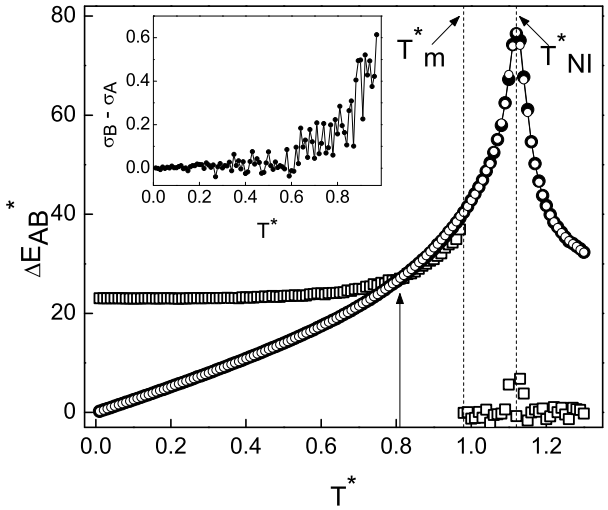

Figure 3.3: Temperature dependence of the difference in the total average energies of film B and A (squares). Filled and open circles represent $\sigma_A/2$ and $\sigma_B/2$ respectively which gives the half of the energy fluctuations of both the structures. Dashed lines are drawn at $T^*_m \sim 0.97$ (where film B merges with A), and at T^*_{NI} which is the NI transition temperature. $T^* = 0.81$ when Δ^*_{AB} crosses the fluctuations is also marked. Inset shows $\sigma_B - \sigma_A$ until both the structures merge at T^*_m.

increases as T^*_m is approached, but its value is seen to be relatively much small (less than 2% of $\sigma_A/2$ at T^*_m).

Figure 3.4(a) shows the average orientation of the nematic director within each of the layers, $\theta_l(z)$, with respect to the z-axis, at $T^* = 0.01$ and 0.9 for both the film structures. The corresponding fluctuations (σ_l) are shown in Figure 3.4(b). The tilting of the director through the layers is in accordance with the director structure shown in Figure 3.1. The average values at higher temperature are seen to deviate from that of the lower temperature one due to the increased fluctuations. For film A, σ_l is seen to increase towards the middle of the film due to the anchoring effect at the boundaries. On the other hand, σ_l for film B increases as we move away from the substrate, reaching a maximum and then decreasing towards the middle of the film. This indicates a relatively stable orientation of the middle layers with director parallel to the substrate. Figure 3.5(a) shows the average order within each layer, $S_l(z)$, at different values of T^*. The corresponding fluctuations (σ_{Sl}) are

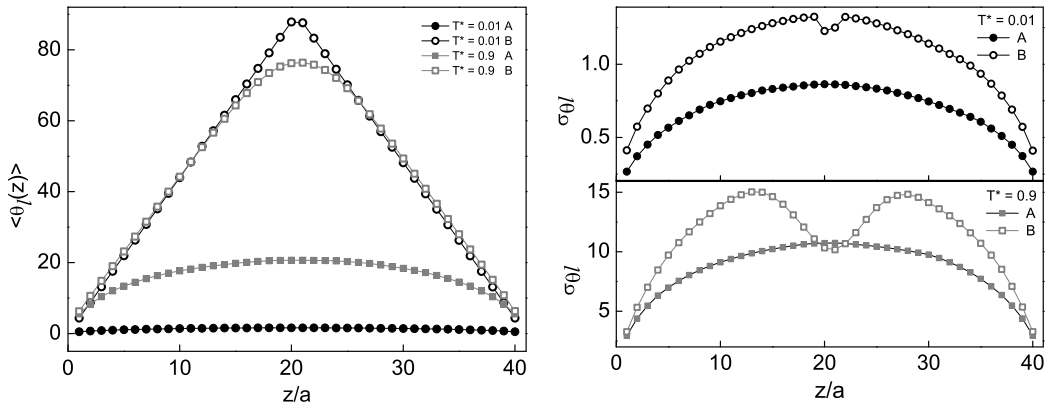

(a) (b)

Figure 3.4: Variation of layer-wise director angle θ_l in degrees (a) and its fluctuations $\sigma_{\theta l}$ (b) along the thickness of the sample for film A (filled symbols) and B (open symbols) at $T^* = 0.01$ and 0.9, computed as MC averages.

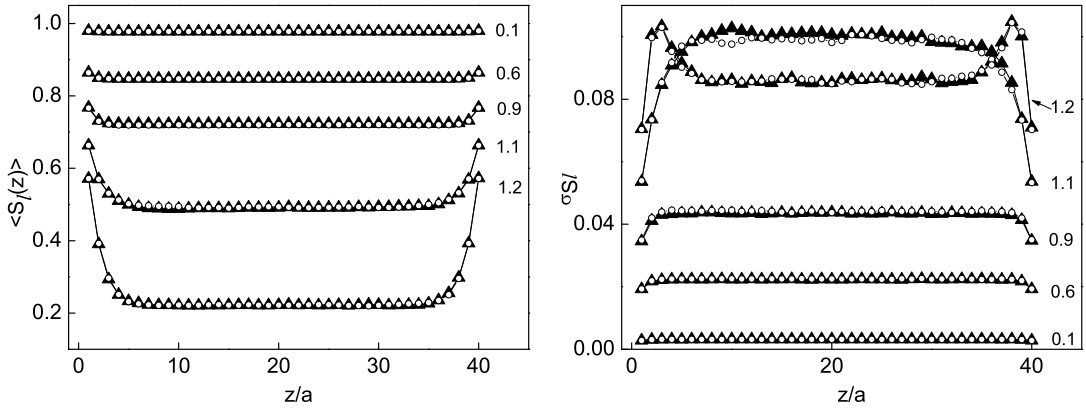

(a) (b)

Figure 3.5: Variation of order within each layer S_l (a) and its fluctuations σ_{Sl} (b) along the thickness of the sample for film A (filled triangles) and B (open circles) at different temperatures as labelled, computed as MC averages. It may be noted that at all the temperatures S_l for both the films are almost identical.

shown in Figure 3.5(b). It is seen that despite the notable difference in the value of S of the two structures, their individual layers are ordered almost identically.

The variation of average the order within each layer with reference to the z-direction, $S_{lz}(z)$ is shown in Figure 3.6(a) and 3.6(b) respectively for films A and B. The behaviour is as expected such that in both the films S_{lz} decreases towards the middle layers. For film B, its value reaches a minimum of ~ -0.5 at $T^* = 0.1$

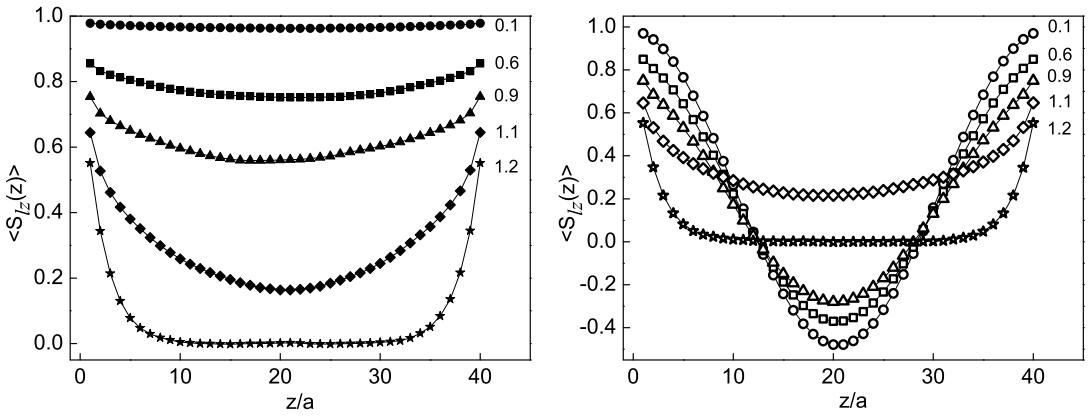

(a) (b)

Figure 3.6: Variation of order within each layer S_{lz} computed with reference to the z direction for film A (a) and B (b) at different temperatures as labelled.

l	N_A	N_B
8	5	5
10	4	6
16	5	5
24	7	3
32	8	2
36	9	1
40	10	0

Table 3.1: Number of occurrence of film A (N_A) and film B (N_B) as the lateral area of the film ($l \times l$) is varied, out of ten simulations with different random initial configurations.

due to the orientation of these layers orthogonal to the z-direction. At $T^* = 1.1$ and 1.2, S_{lz} varies in an identical manner in both the cases as the merging of the two sets of microstates has already taken place.

A rough estimate of the film's lateral size (l) dependence of the probability of spontaneous occurrence of film B is determined by performing 10 simulations with different initial random configurations, by varying l at $d = 40$. From an initially isotropic state the system is quenched to a low temperature. The site orientations and order parameter values are monitored to classify the director structure into

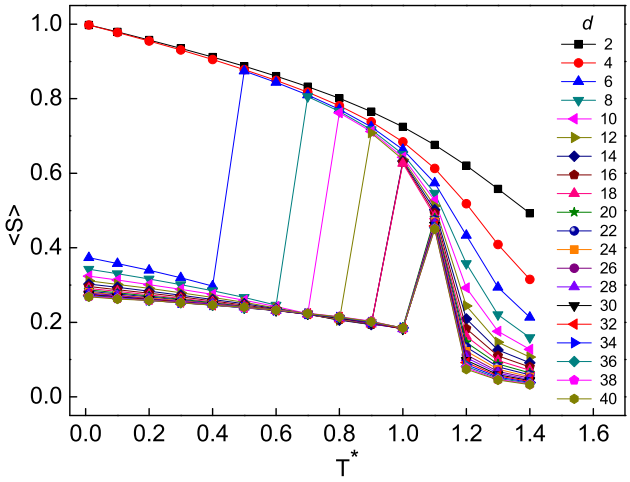

Figure 3.7: Thermal variation of average order S at different values of film thickness d at $l = 24$, as the system is heated from an initial configuration with director structure corresponding to film B. It may be seen that the film B is not feasible for $d < 6$, setting a critical value of thickness for the film [100, 185].

which the system condenses to. The findings are listed in Table 3.1. It is seen that the probability of spontaneous occurrence of director structure of film B reduces as the lateral area $(l \times l)$ of the film increases. Dependence on the film thickness d of the temperature range over which film B remains stable (before merging with the film A) is also studied. For this we considered a film with larger lateral area $(l = 24)$, and the initial director structure is chosen to correspond to that of film B. Temperature scans are performed (with a resolution of 0.1) for various values of d. Results are shown in Figure 3.7. It is seen that except for very thin films $(d < 6)$, film B is feasible, and the temperature range over which this structure remains stable increases with increasing film thickness. This is understandable as the anchoring field effects are dominant in thinner films $(d < 6)$ setting a critical value for the film thickness [100, 185].

A closer inspection of the merging of film B with film A is effected by monitoring S and keeping track of the microstates during the canonical evolution. As discussed earlier, a merging could occur at any temperature $T^* > 0.81$. Snapshots of microstates of the system at high enough temperatures, $(T^* = 0.99$ and $1.04)$ as the film B merges with film A, are presented in Figures 3.8 and 3.9. The interesting circumstance at these temperatures is that the fluctuation in the energies of the

two structures become comparable to the differences between their average energies (refer to Figure 3.3). Thermal fluctuations in this temperature region seem to be driving the film B towards the (global) free energy minimum corresponding to the homeotropic arrangement of film A. The snapshots depict these interesting changes as the system transits from the (bulk-wise) low ordered state to the more probable state with compatible orientational order. Concomitant qualitative changes in the topology of the structures (particularly is evident at $T^* = 1.04$) may also be noted.

3.2 Entropic sampling

An entropic sampling (random walk in the configurational space resulting in a distribution uniform with respect to its energy) is performed on the film, with an initial configuration corresponding to film B at a low temperature. The resulting energy-order (E^*-S) microstate space is shown in Figure 3.10. From the initial state corresponding to the leftmost region of the lower branch in the figure (marked by the arrow), the system accesses regions of the microstate space by swiftly moving towards the right. This is because an increase in energy is favoured by entropy. The microstates belonging to the lower narrow branch in the figure are compatible with the film B. As the system starts sampling higher energy regions (or equivalently higher temperature regions), it then traverses along the broader

Figure 3.8: (***following page***): (a) Canonical MC evolution of macroscopic order parameter S near the region of merging of film B with film A captured at $T^* = 0.99$. (b)-(h) Snapshots from the marked regions of (a) as the transition happens from $B \rightarrow A$. Microstate in (b) and (h) have director structures of films B and A respectively. It can be seen that the director profile remains similar on the left hand side whereas major orientational rearrangements happen on the other half of the film, as is more evident from (d), (e) and (f) cases. (Due to thermal fluctuations, the actual LC spin orientations at this temperature are found to give less visual information. Hence for the purpose of a clearer depiction of the director profile, each represented spin in the figure correspond to a local director (apolar) computed over the nearest neighbouring bulk LC sites.) Reference axis and colour map are same as that of Figure 3.1.

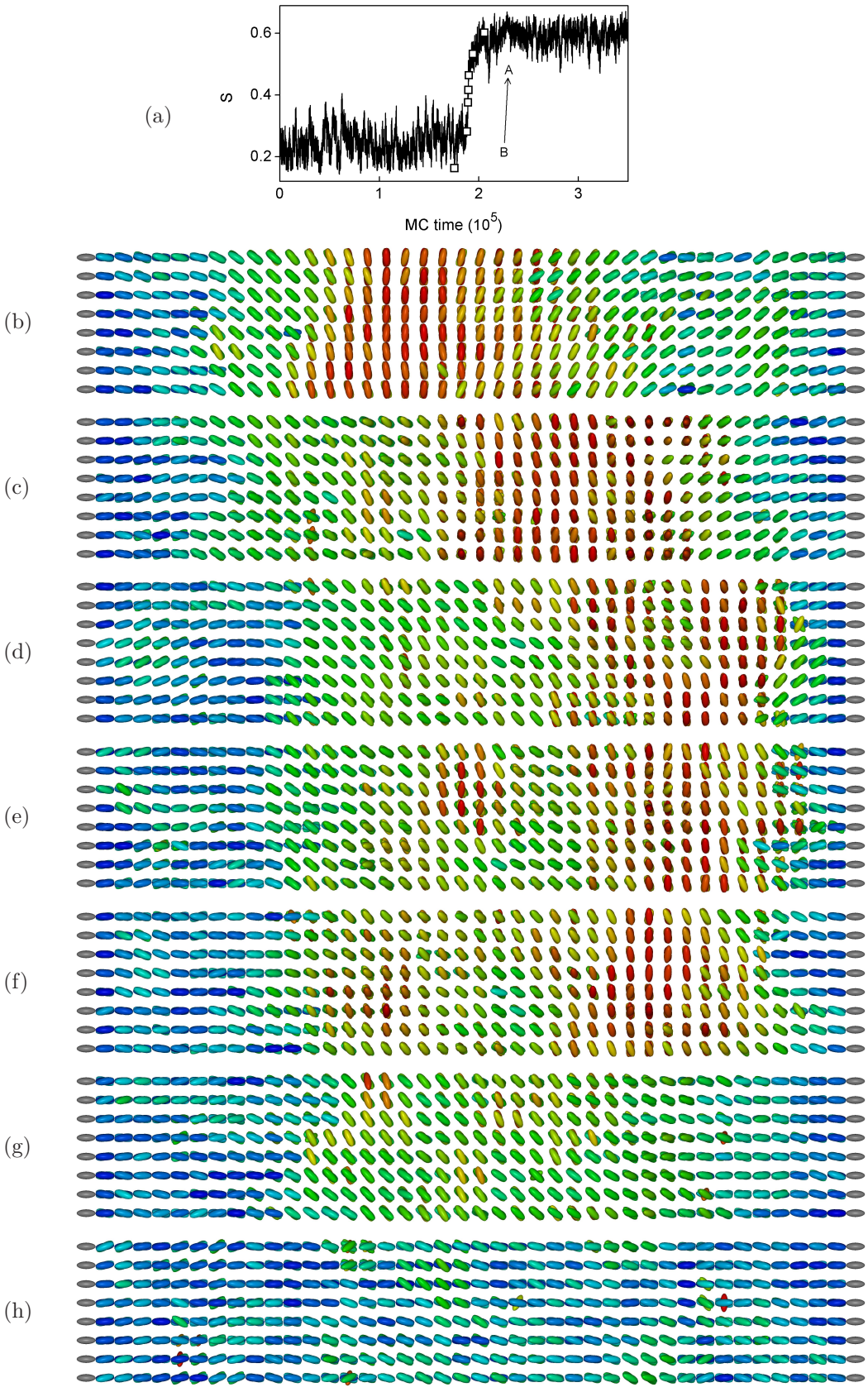

Please see the previous page for caption.

(a)

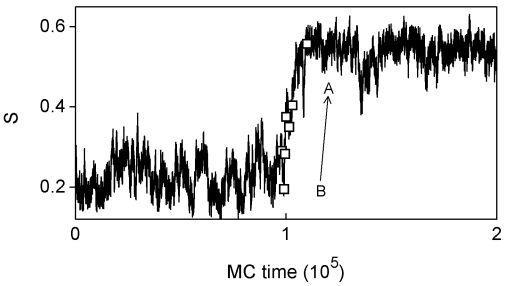

(b)

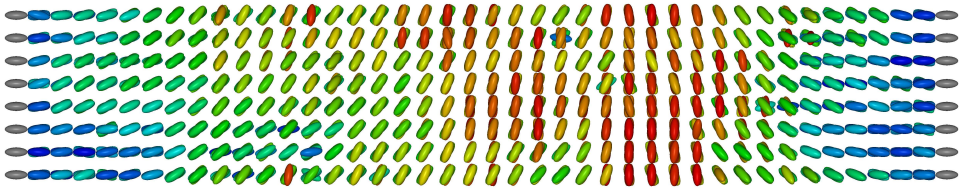

(c)

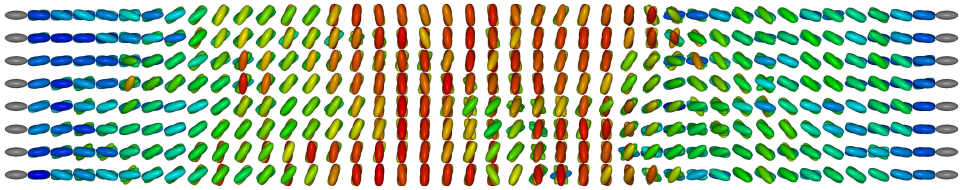

(d)

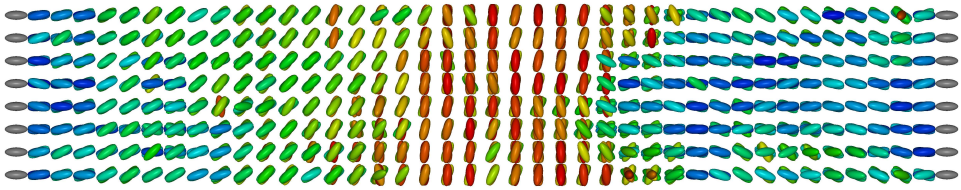

(e)

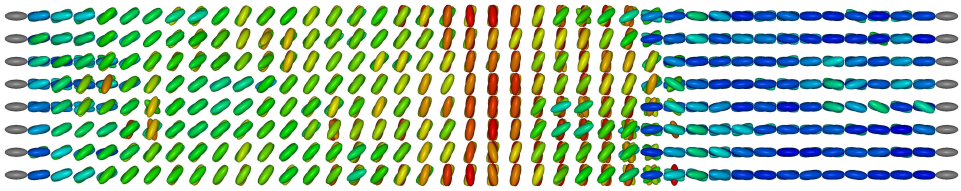

(f)

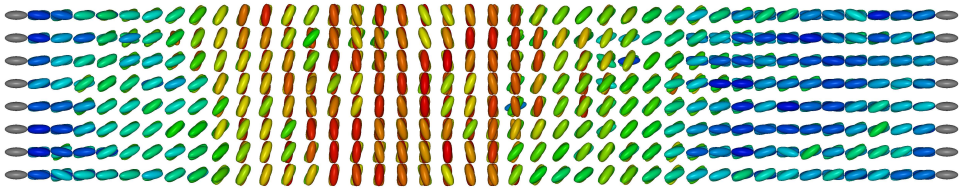

(g)

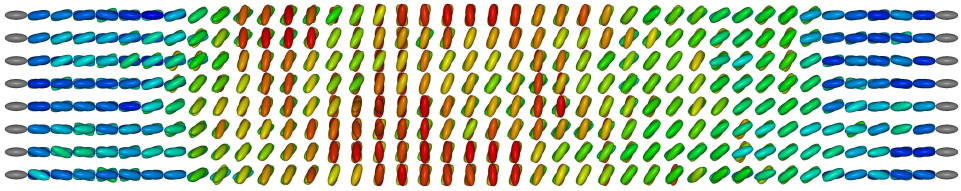

(h)

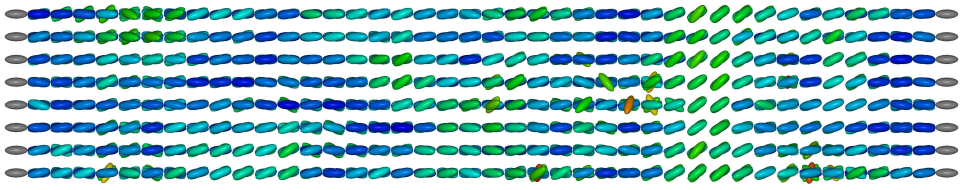

Figure 3.9: Same as Figure 3.8 but at $T^* = 1.04$.

region where the microstates are compatible with the film A, and once film B transits to this region, it does not visit the microstates of the lower branch again. This points to the relative abundance of states corresponding to that of film A and also to the inaccessibility of microstates connecting both the structures, alluding to the presence of potential entropic barriers.

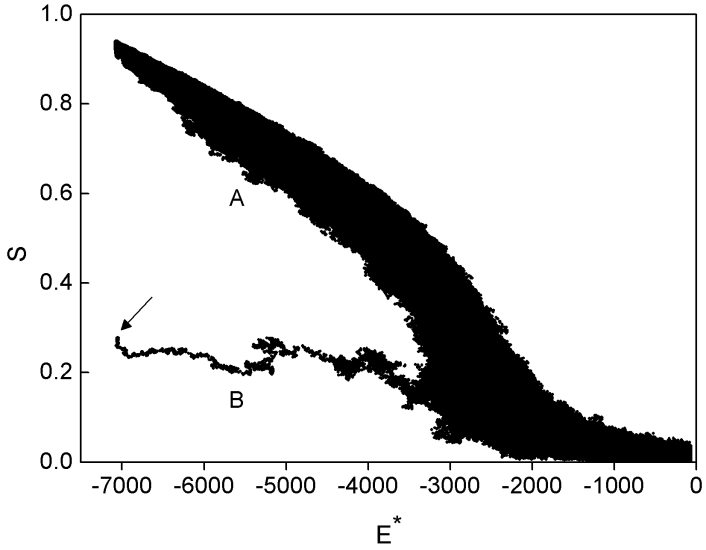

Figure 3.10: E^*-S microstate space obtained during the production run of the entropic sampling. The initial configuration is marked by an arrow in the lower narrow branch corresponding to film B. This is the result of putting the coordinate of the microstates collected during the respective random walks.

We studied the regions of the E^*-S space, where the microstates are sparse by concentrating on the lower energy region of the branch in Figure 3.10 corresponding to film B. The initial configuration is chosen to correspond to film B (indicated by the arrow in the figure) and the maximum value for the admissible energy of the system is set as E^*_{cut}. (Please note that E^*_{cut} represents total energy from all the N_s LC spins.) Strictly for the purposes of reference, we tag this energy with a corresponding temperature T^*_{cut} by making a correspondence of E^*_{cut} with the average energy of the system under Boltzmann sampling. Thus for $E^*_{cut} = -5700$, $T^*_{cut} \sim 0.69$. It is observed that the system quickly reaches, in the process of random walk, this highest permissible value of energy, and remains in the lower branch throughout the length of the simulation. When an external field, E_a of adequate strength, which tends to orient the LC sites along the z-direction (through

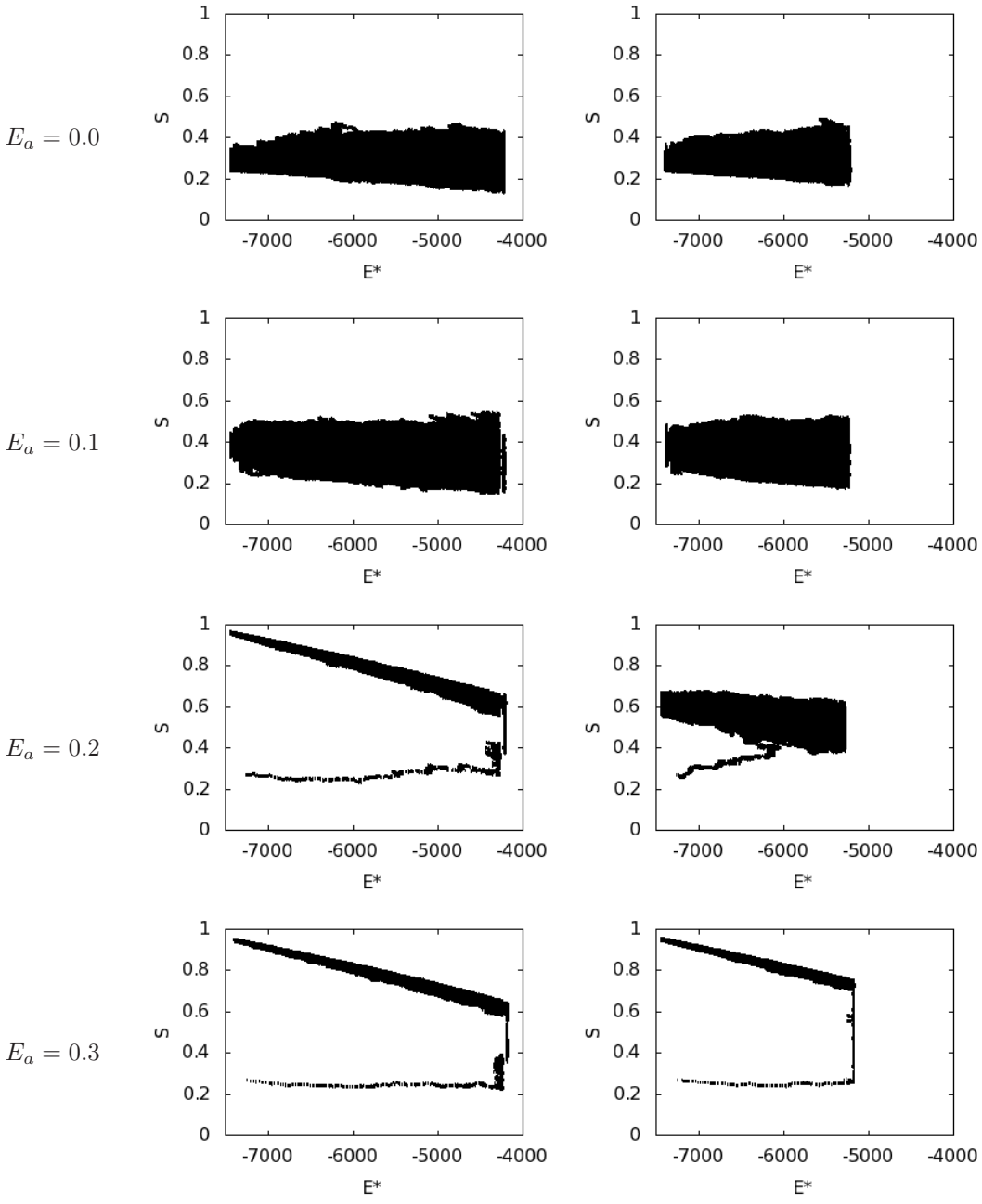

Figure 3.11: E^*-S microstate space spanned during entropic sampling at higher (right) and lower (left) values of set E^*_{cut} (corresponding to energies well below the merging temperature in Figure 3.3), for various strengths of external field, E_a. Merging from film $B \rightarrow A$ is aided by E_a, which occurs at lower values of E_a for higher E^*_{cut}. Initial configuration is same as that in Figure 3.10.

an additional interaction term of the form -$E_a^2 P_2(cos\theta_i)$, where θ_i is the angle between i^{th} LC spin and the z-axis), is applied, the system is assisted to traverse from the microstate space of film B to that of film A. Figure 3.11 shows the E^*-S space spanned by the system for various values of applied E_a. Strength of the field required to merge B with A increases as E^*_{cut} is lowered. In the spirit of aiding a reverse transformation, where an initial configuration belonging to structure A at low energy is subjected to an external field tending to orient the LC spins perpendicular to the z-direction (Fréedericksz transition), structures with different director profiles are expected. We refer to the set of such microstates topologically connected with film A as $\{A'\}$. However there are qualitative differences between the director structures of the microstates $\{A'\}$ and those of film B, as discussed later in *Discussion* section.

3.3 Order parameter-based sampling (OP-sampling)

So far it remains that both the structures appear disconnected in the lower energy region with the energy-based uniform (entropic) sampling procedure, unless aided by an external field. This suggests a novel possibility of guiding the random walk in the configuration space based on another reaction coordinate, say the order parameter, keeping the energy of the system confined to a very narrow range of a chosen fixed value (approximating to a microcanonical ensemble). This appears appropriate as the bulk order S is the distinguishing characteristic of the two apparently disconnected structures. In this perspective, we propose an order parameter-based entropic-like sampling (OP-sampling), analogous to its energy-based counterpart, in order to determine the distribution of states in a chosen film (at a fixed energy value) with respect to S, $g(S)$. Here the random walk is performed along the order parameter S axis which is guided by an acceptance probability for a move from state i with order S_i to j with S_j by,

$$acc(i \rightarrow j) = \begin{cases} \frac{g(S_i)}{g(S_j)} & \text{if } g(S_i) < g(S_j), \\ 1 & \text{otherwise.} \end{cases} \tag{3.1}$$

This procedure is further augmented by a corresponding frontier sampling protocol (along S-axis) to significantly improve its efficacy to sample extremely rare states, more readily. The simulation is restricted to a narrow energy range as the objective is to seek all the accessible director structures of microstates compatible with a given energy, of course without the (canonical) fluctuations. The energy region to be spanned is accordingly restricted by denying the system access the states of higher energy beyond the set E^*_{cut}. Due to the inherent tendency of the system to reach out the high energy states (higher entropy) the only deviations from this set energy mark to lower values are due to canonical fluctuations, and these excursions are found to be be less than 0.05% of the set value. The distribution of states with respect to energy visited during such runs are shown in Figure 3.12(a) for a typical value of E^*_{cut}. The initial configuration of the microstate for OP-sampling simulation is chosen to belong to film A with a very low chosen energy, and a correspondingly high order. Figure 3.12(b) shows the evolution of the order parameter of the system as the Monte Carlo time progresses, with markers placed at each frontier sampling stage (discussed in section 2.3.1).

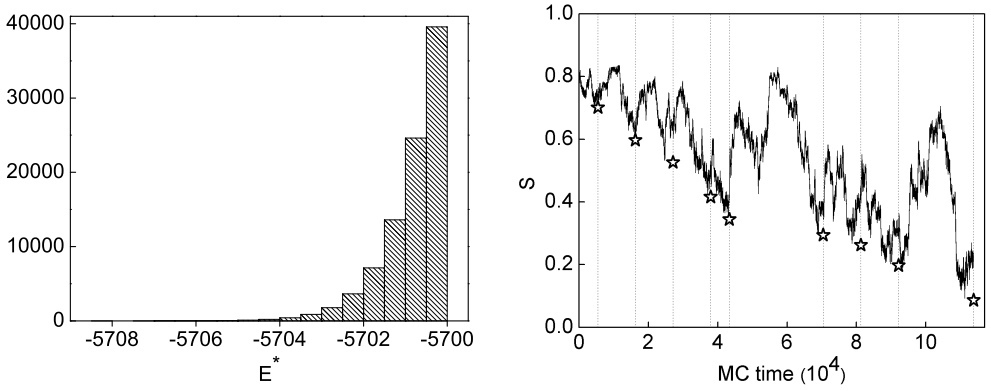

(a) (b)

Figure 3.12: (a) Distribution of energy states sampled during OP-sampling at $E^*_{cut} = -5700$. (b) Evolution of S with Monte Carlo time during frontier sampling stage at $E^*_{cut} = -5700$. Dashed lines mark the time at which a fresh frontier is introduced, and the minimum value of S corresponding to the following boost in the updation of $g(S)$ is marked by star symbols.

As the simulation begins, the energy of the system initially increases rapidly to E^*_{cut} value due to entropic reasons, and thereafter fluctuates within a narrow range.

But for the restriction not to cross E^*_{cut} to higher values, there are no other constraints on the system. Under these conditions, the recipe of OP-sampling results in visiting states compatible energetically, but encompassing a wide range of S. A successful sampling, satisfying certain flatness criterion (see section 2.3) leads to an estimation of $g(S)$ appropriate to the chosen energy E^*_{cut}. Figure 3.13(a) shows the normalized distribution of states with respect to S, obtained at $E^*_{cut} = -5700$ (~ -2.2265 energy per particle). It is seen that the distribution peaks near $S \sim 0.78$ which corresponds to the canonical average value of order of film A at $T^*_{cut} \sim 0.69$. This is evident also from a more peaked distribution obtained in the presence of an external field E_a applied along the z-direction. Plots depicting the variation of $g(S)$ at different values of E^*_{cut} for the field value $E_a = 0.3$ are shown in Figure 3.13(b). A similar experiment is performed with an initial microstate belonging to film B with a low energy ($E^* \sim -7700,\ S \sim 0.26$). Profiles of $g(S)$ thus obtained are shown in Figure 3.13(c) where the range of S values accessed is seen to increase as E^*_{cut} is decreased. It is seen that the peak position of these profiles obtained in this case occur progressively at lower values of S, in contrast to that seen in Figure 3.13(a). For comparison, the snapshots of microstates with comparable energy and macroscopic order parameter obtained from OP-sampling performed with films A and B, are shown in Figure 3.14. Here a low value of $E^*_{cut} = -7000$ (or ~ -2.7343 energy per particle) is chosen to depict the qualitative differences in the director structures with minimal orientational fluctuations obscuring them. It may be noted that these are not the equilibrium structures and hence are only representative microstates belonging to the corresponding ensembles. It is seen that the director structures obtained in both cases differ qualitatively. Tilt of the director from the substrate to the planar region towards the middle of the film occurs symmetrically along one of the lateral directions (downwards here) in the case of film B in Figure 3.14(b). On the other hand, the bend occurs along opposite directions in each half-plane of the film in Figure 3.14(a). As we discuss later, these differences are profound, and correspond to different topologies.

To investigate the relaxation paths of the rare states thus obtained from each of these films, canonical simulations are performed at $T^* = 0.69$, starting with

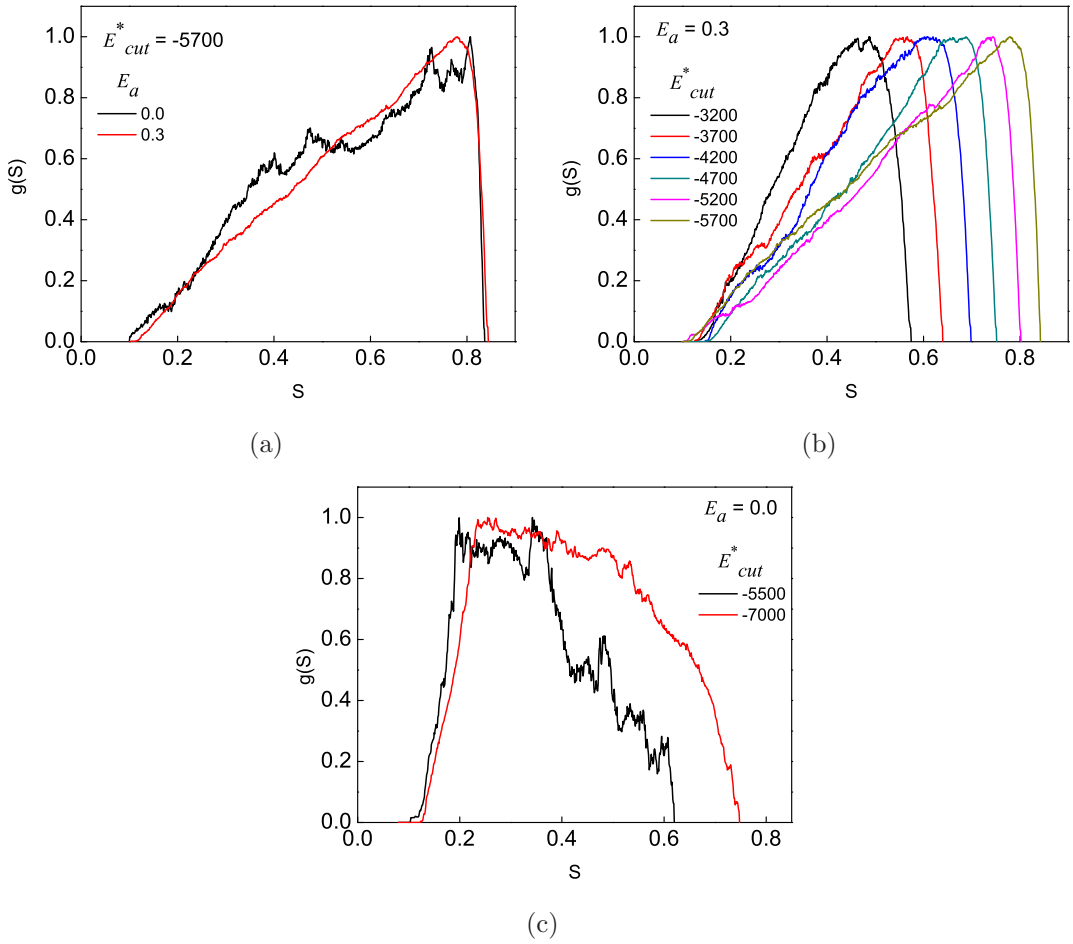

Figure 3.13: Normalized distribution of available microstates obtained from OP-sampling as a function of S (a) of film A for different values of E_a at $E^*_{cut} = -5700$ (~ -2.2265 energy per particle) and (b) of film A for different values of E^*_{cut} at $E_a = 0.3$. (c) of film B for different values of E^*_{cut} without a field.

different initial microstates chosen at different values of S, obtained through the OP-sampling of the film A at $E^*_{cut} = -5700$. At this temperature, the degree of fluctuations in the energy of the system is lower than the difference in their canonical average values for both the structures (see Figure 3.2). The Monte Carlo time evolutions of S for these cases are shown in Figure 3.15. It is seen that in all the cases, S values relax to the canonical equilibrium value of ~ 0.77 corresponding to film A. A similar simulation with the initial configuration belonging to film B at $T^* = 0.69$ with its S at the mean value of at ~ 0.27 is attempted. It has been found to be stable, and retains the structure of film B over a fairly long

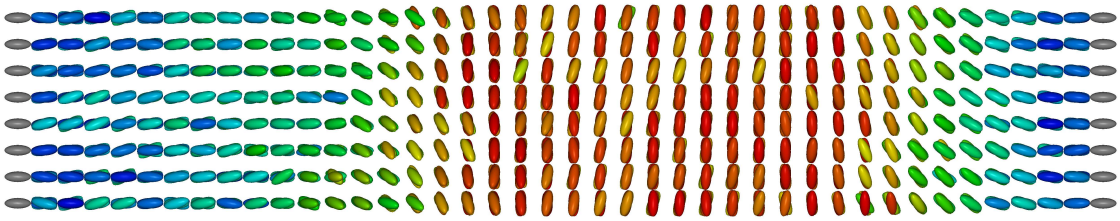

(a)

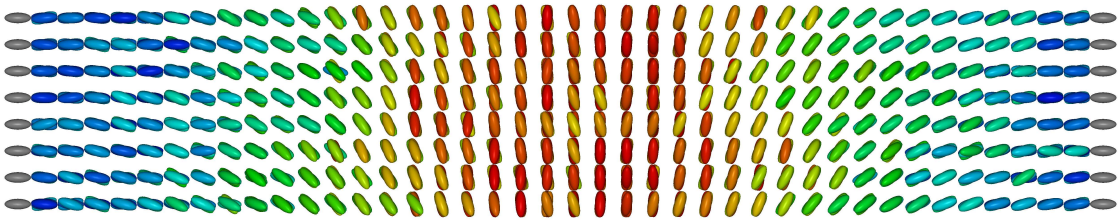

(b)

Figure 3.14: Snapshots of microstates obtained from OP-sampling at $E^*_{cut} = -7000$ with initial configurations chosen to belong to (a) film A and (b) film B. In both the cases $S \sim 0.2$. It may be noted that the tilt spin orientations on the right half is in opposite directions for (a) and (b). Reference axis and colour map are same as that of Figure 3.1.

evolution period. These observations indicate that the rare microstates obtained from the OP-sampling of film A are distinct, and do not "mix" with those of film B. The microstates of film A with diverse values of S are thus transient states spanning distinct regions of configuration space, not accessible to film B, and they are topologically distinct as is elaborated below. Hence though this sampling method explores microstates with agreeable E^* and S belonging to films A and B, the structures seem to be disconnected in the sense of Markov chain Monte Carlo (MCMC) dynamics, in a large region of the microstate space. Thus the general transition matrix of the MCMC dynamics in the total configuration space (in the low temperature region) is reducible.

Snapshots of the system during the OP-sampling of films A and B captured at various values of order parameters, for $E^*_{cut} = -7000$, are shown in Figure 3.16 and Figure 3.17 respectively. It is informative to examine the director structures of these transient states. Referring to Figure 3.2 it is seen that its equilibrium state

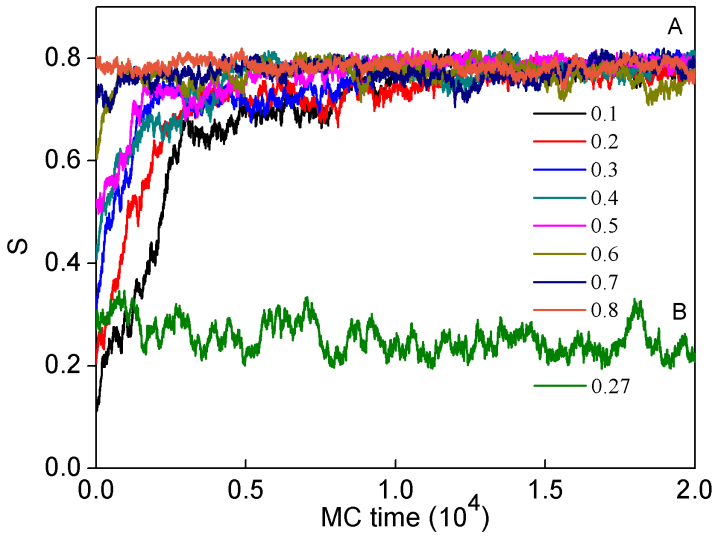

Figure 3.15: Evolution of microstates with MC time during a canonical sampling at $T^* = 0.69$ with initial microstates chosen from a S based entropic sampling at $E^*_{cut} = -5700$. Legend shows the approximate values initial order $S_{initial}$ of the microstates. For the case of lower green line below, the initial microstate belong to film B at the same temperature.

corresponds to $S \approx 0.92$ at $E^*_{cut} = -7000$ (film A) exhibiting a simple homeotropic arrangement corresponding to the (global) free energy minimum. Now as OP-sampling tries to see lower ordered states, extending upto $S = 0.2$, with the caveat that the energy of the system is essentially kept constant, the system exhibits fascinating transient structures. Since these are random snapshots taken during evolution, they are only representative. It may be seen that initially film A tries to accommodate the bulk-wise less ordered states by introducing compensating bent structures at either ends till $S \approx 0.6$. Further demand to seek microstates with lower values of S makes the film adopt a different strategy, viz, encompass a slab-like structure (parallel to the substrate), but with an interfacing bent segments to match the substrate boundary conditions. Thus till about $S \approx 0.6$ the eigen

Figure 3.16: (***following page***): Director structures of the film at different values of S obtained from OP-sampling for film A at $E^*_{cut} = -7000$. Here the viewing direction is along one of the lateral axes, and therefore show at each lattice site a superposition of the orientations of the spin along the line of sight. Reference axis and colour map are same as that of Figure 3.1.

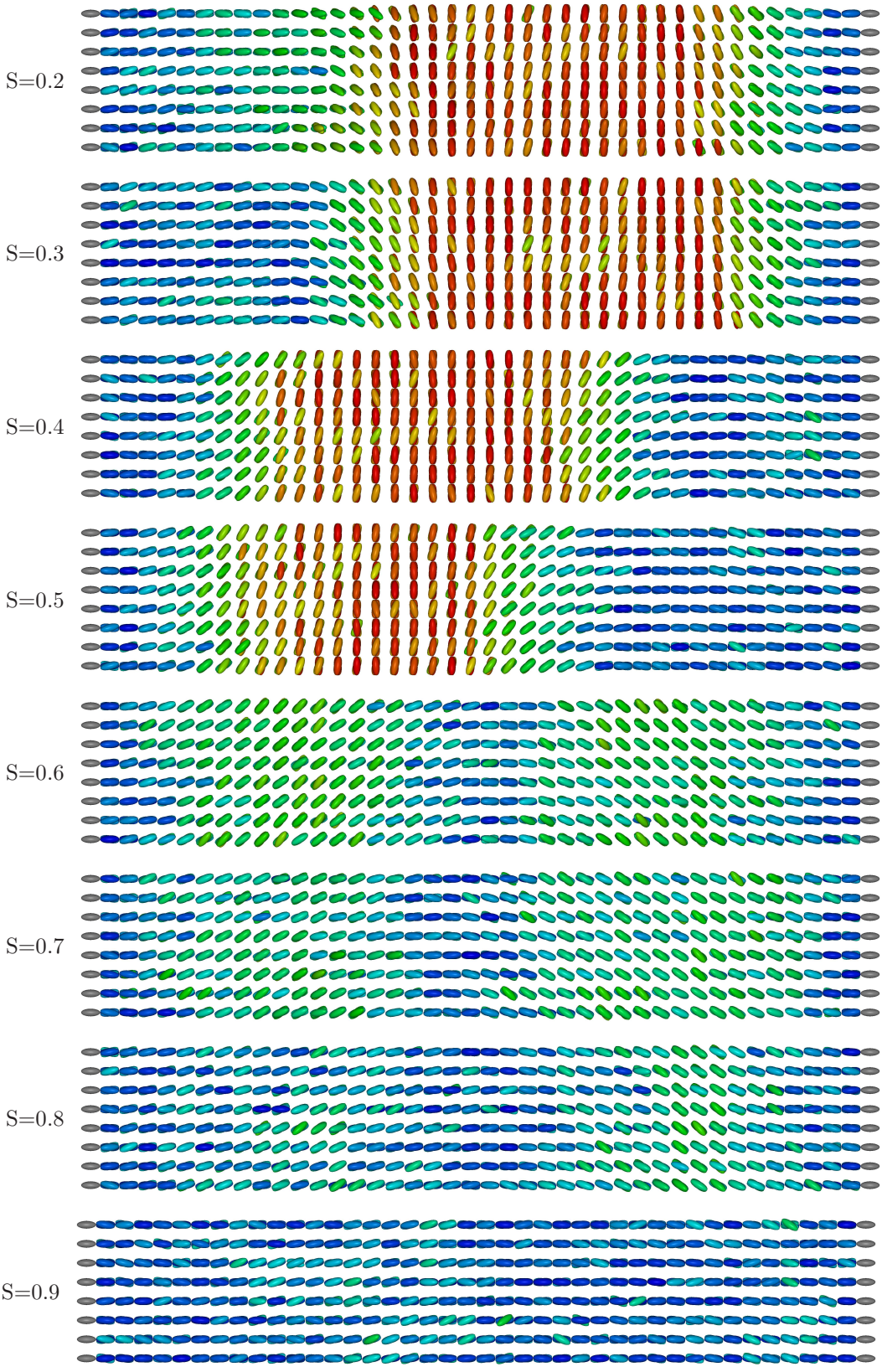

Please see the previous page for caption.

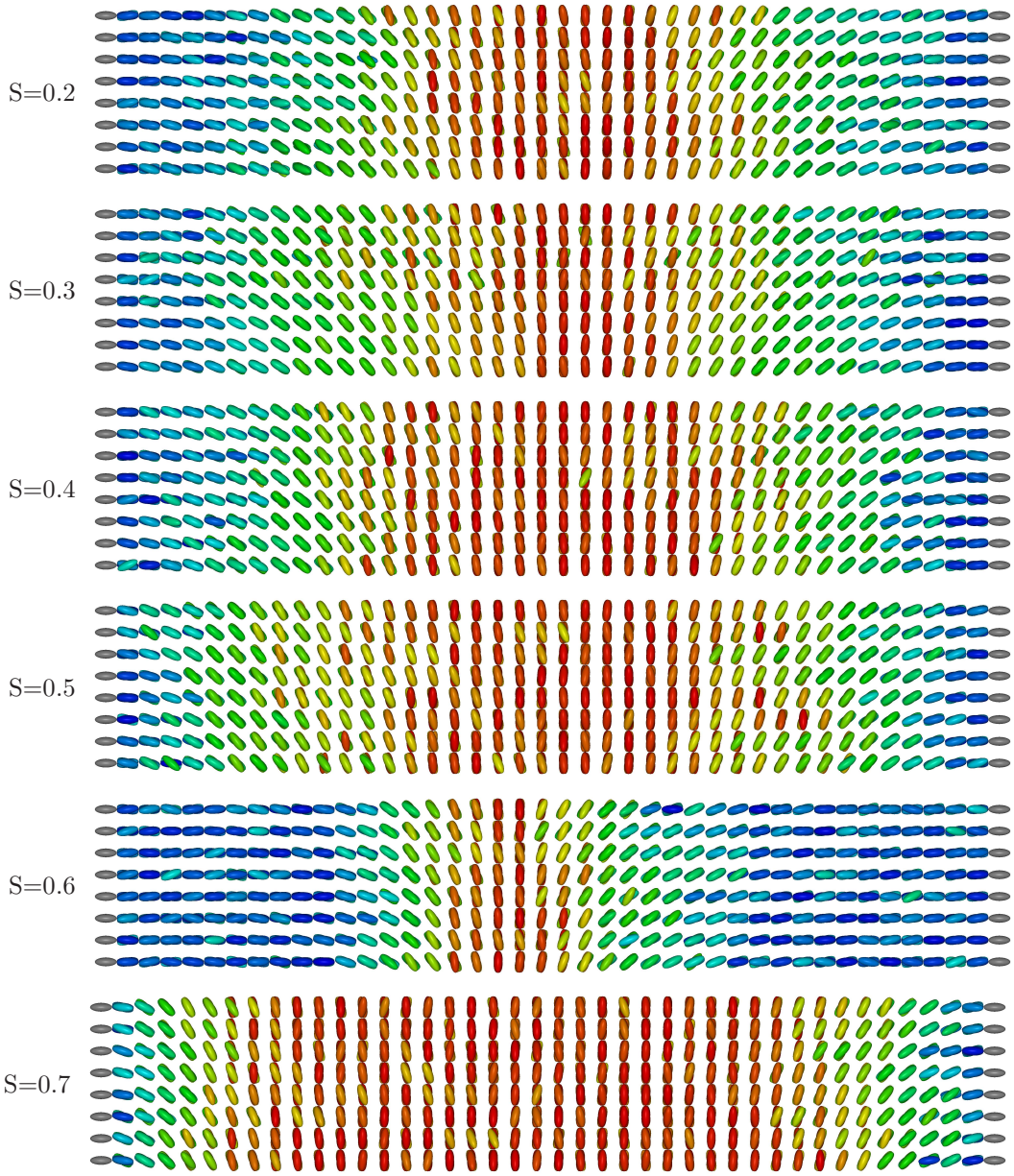

Figure 3.17: Same as Figure 3.16 for film B at $E^*_{cut} = -7000$.

vector corresponding to the maximum value of the ordering tensor of the molecular axes, remains essentially aligned more along the normal to the substrate. Much lower values of S require geometrical averaging be brought into play to meet simultaneous demand on S and constraint on (constant) E^*_{cut}. Thus the lower order ($S \approx 0.2$-0.3), compatible with the equilibrium value of film B, is achieved

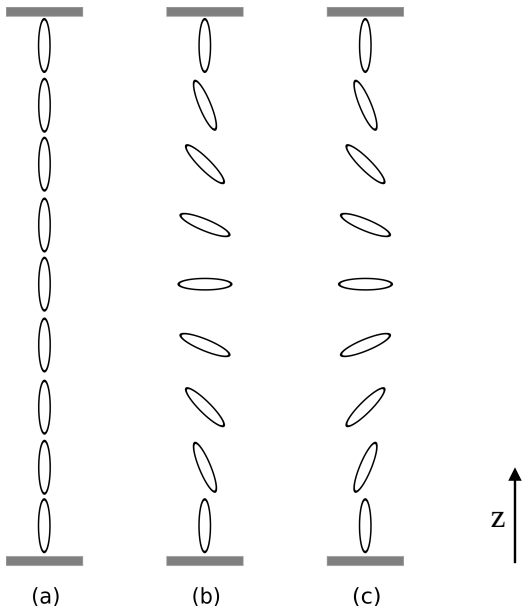

Figure 3.18: Schematic showing the various director profiles for the films (a) A, (b) its transient states A' and (c) film B within a film with homeotropic surface anchoring. Note the difference in orientations in the lower half plane of A' and B.

by progressively increasing the degree of geometrical averaging process. From this perspective, the rotation of the eigen vector of the long axis of Q by $\pi/2$, as we reach the middle of the film is common to both the films A and B (see the snapshots for $S = 0.3$ in Figures 3.16 and 3.17). However these two structures are topologically distinct: equilibrium states of film A could be reached by continuous (bulk) deformation of its transient structures $\{A'\}$., whereas none of the structures of film B can be mapped to those of film A. This is more evident from the transient structures of B shown in Figure 3.17. The system here, under algorithmic pressure to seek higher ordered states but at same energy, achieves this again by reducing the degree of geometrical averaging by including more coherently ordered layers in the middle, while paying its energy cost at the interface. The important difference to note is that in all its transient states film B retains the same protocol of the tilt of the director. In the light of these observations, the results of Figure 3.15 showing non-intersection of these microstates should not be surprising.

Discussion

Focussing on the low-ordered director structures that the film A could exhibit under OP-sampling (Figure 3.16 - microstates $\{A'\}$), we notice that these correspond to the distortions that a homeotropic film would undergo in a Fréedericksz transition, as the applied field (in the plane of the film) crosses a threshold value. Thus A and A' structures are topologically equivalent, and there is no energy barrier between them: withdrawal of the field results in the film relaxing towards zero-field equilibrium structure. Schematic representations of the director profiles for these various structures are shown in Figure 3.18. We thus observe that the OP-sampling seeks such topologically equivalent, but geometrically deviating, configurations in detecting low-ordered structures at a given energy. It may be noted that in general all such structures which differ in the rotation of the uniaxial director across the cell by a multiple of 2π are equivalent from this perspective [190]. Referring to the film A as monostable in this sense, film B is topologically distinct, and hence could be transformed to film-A structure only with the application of an external field. These two films thus form a pair of bistable states, differing in energy and hence a barrier preventing their inter-conversion. The rotation angle of the main eigen value of the layer-wise ordering tensor of the medium undergoes zero degree shift in the film A (or multiples of 2π in its rare (no field) but topologically connected A' structure), and π in film B. Such topologically distinct, but stable director structures are indeed of great interest for bistable display devices [190, 226, 227]. Once this is noted, the outcome of the present work can be summarized.

Attempts to look for a topologically differing film structures under homeotropic anchoring condition in a film of uniaxial liquid crystal medium have been successful. These are separated by an energy barrier and can be connected only through the application of an external field where film B transforms to film A. At high enough temperatures, when the energy fluctuations of these structures match the energy difference, the energy barrier is observed to disappear facilitating the merger of the structures of the two films. In the process of investigating these structures compatible with film A, at a given energy in the nematic phase, we developed an algorithm to carry out uniform random walk along the order parameter axis. Being guided by essentially Metropolis algorithm at the level of acceptance of the trial states, this walk encompasses only topologically equivalent

states. In the present case this walk results in structures which are reminiscent of microstates resulting after the Fréedericksz transition. Attempts to force film B to such higher order states under OP-sampling yields rare microstates which are topologically consistent. Finally, the development of the OP-sampling procedure seems to hold a promise to investigate the order-wise distribution of microstates (within a thin energy slice) in bulk systems as well. This forms the subject matter of the next chapter.

Chapter 4

Order parameter-based sampling: bulk nematic systems

In this chapter we apply the OP-sampling method to bulk liquid crystal systems, both uniaxial and biaxial. These studies demonstrate the efficacy of the method to reach out to very rare regions of the microstate space, starting from canonical equilibrium regions. The microstate space is visited giving importance to sampling all possible microstates resulting from a uniform walk along the OP axis, within a given energy slice. Different regions of this spanned microstate space corresponding to varying values of the OP are analyzed, a useful handle being the spatial dependence of the orientational pair correlations. While the implementation of the method itself proved to be demanding in terms of computational effort, our preliminary investigations allude to the prospects of adopting this method to study many interesting physical systems, like sampling the non-equilibrium fluctuations of the system, detection of transient states, possible enumeration of director structures after a deep quench from a higher temperature phases *etc.* Another scenario is the possibility of determining joint density of states, $g(E,\ S)$ which stands challenging as of today for a continuous system like liquid crystals. The OP-sampling method combined with the energy based entropic sampling can in this context be a plausible computing technique to estimate $g(E,\ S)$, following an efficient stitching together of $g(S)$ and $g(E)$, both estimated to a good accuracy. Such studies attempting to compute $g(E,\ S)$ are so far concerned with Heisenberg magnetic spin system [173], and LC systems in one dimension [228, 229].

4.1 Uniaxial system

We consider here a (cubic) lattice model ($15\times15\times15$) of uniaxial LC medium, with nearest neighbours interacting *via* Lebwohl-Lasher potential [93]. Simulations are

performed at chosen values of energy, E^*_{cut} (the upper limit of energy permitted for the system), and the initial configuration is chosen from the canonical ensemble at the corresponding temperature, T^*_{cut} (at this temperature the average energy of the system obtained from a canonical Boltzmann distribution is equal to E^*_{cut}, and the initial microstate is chosen from the corresponding canonical ensemble with its microstate's energy closest to E^*_{cut}). The sampling procedure (as discussed in section 3.3) enables the sampling of the microstate space spanning over a wide range of order parameters while maintaining the energy of the system to within a narrow window close to the set E^*_{cut}.

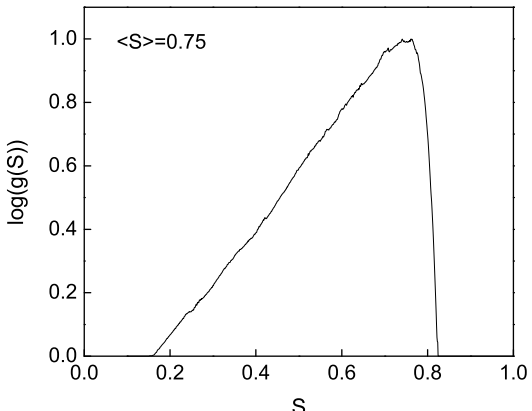

Figure 4.1: Normalized distribution (log scale) of states with respect to the uniaxial order S, obtained from OP-sampling at $T^*_{cut} = 0.8$. The corresponding canonical average value of S at this temperature is 0.75.

Figure 4.1 shows the distribution of states, $g(S)$ in a normalized scale, obtained from OP-sampling at T^*_{cut}=0.8. The distribution is seen to peak near the canonical average value of order ($\langle S \rangle$) at this temperature. While $g(S)$ extends to some degree towards higher values of S, it encompasses significantly towards the lower ordered regions. Obviously the microstates corresponding to their extensions in $g(S)$ are very rare transient fluctuations, essentially of the canonical ensemble. It is to be noted that all these states have essentially the same energy, but for fluctuations restricted to within 0.2%. Excursion of the order parameter to higher values (than $\langle S \rangle$) would require necessarily lowering of energy (corresponding to more order), which is inhibited consequent lowering of its entropy. Its variations

induced by OP-sampling to lower ordered states are more extensive, till about $S \approx 0.2$. These microstates corresponds to internal director structures which produce the required (low) value by geometrical averaging of the ordering tensor, while preserving the total energy by the formation of locally ordered domains. Thus, in a sense, the OP-sampling is facilitating a systematic collection of all transient states (of essentially same energy) but very different bulk-wise order.

It is observed that the estimation of $g(S)$ requires increasing computational effort as E^*_{cut} is decreased. This is due to the increased rarity of such bulk-wise low ordered states consistent with very low energies, or equivalently for systems equilibrated at lower temperatures. The system size also contributes to this by restricting the possible number of locally aligned domains, but randomly distributed with respect to their orientations, within the sample.

We attempted quantifying the characteristics of these microstates by collecting, during the evolution of $g(S)$, 2×10^5 microstates, each belonging to one or the other of the windows of order parameter centered at differing values, S_w with a width of 0.02. From the ensemble of microstates within each S_w-window, the average second rank orientational pair correlation, $G_2(r)$ (equation 2.26) is determined up to a cut-off distance of $r/a = 7$ (where a is the lattice spacing), by constructing spherical shells of varying radii centered at the LC site. A further averaging is effected by choosing 130 such random LC sites. Figure 4.2 (a) shows $G_2(r)$ determined at $T^*_{cut} = 0.55$ for different values of S_w. At this temperature the canonical average value of orientational order is $\langle S\rangle = \langle S_{cut}\rangle = 0.85$. For a homogeneous nematic phase, the orientational correlations begin from one at $r = 0$, decay as r increases and eventually saturate to a value $\sim \langle S\rangle^2$. Such decays are satisfactorily fitted to Ornstein-Zernike form $(\frac{A}{r}\exp(-k_c r))$ [94]. This behaviour is seen for $G_2(r)$ obtained from the canonical Boltzmann distribution shown in black open circles. A similar behaviour is seen for the case where $S_w > \langle S_{cut}\rangle$ at the set T^*_{cut}. On the other hand, $G_2(r)$ for the microstates belonging to $S_w < \langle S_{cut}\rangle$ continue to decay with distance and do not saturate even at higher values of r. This is a clear evidence of the formation of domains within the sample, which are locally ordered by aligning the LC spins along a local director, while the

domains themselves are misaligned with respect to each other. At lower S_w, $G_2(r)$ is seen to develop undulations with r. These indicate a periodic development of similarly ordered regions distributed within the sample. A quantitative estimation of the components of wavenumbers, k_w associated with these director structures is made using discrete Fourier transform, and the corresponding magnitude spectrum obtained as a function of k_w is shown in Figure 4.2 (b). The black open circles represent the homogeneous nematic states from a Boltzmann distribution is seen to peak at $k_w = 0$ and tail off at higher values of r. It is also seen that for the cases of lower S_w, apart from the prominent mode at zero wavenumber, the curve shows a noticeable spike at $k_w = 7$ and smaller spikes near $k_w = 10$ and 13. These correspond to wavelengths of 1, 0.7, and 0.53 respectively in units of lattice spacing a, indicating the presence of short wavelength undulations within the sample. Snapshots of the system at $T^*_{cut} = 0.55$ for different S_w are shown in Figure 4.2 (c)-(k). (Please refer to figure caption for more details). The undulations in $G_2(r)$ are observed to decrease as T^*_{cut} is increased, and consequently the contributions from secondary spikes are also found to decrease, as is evident from Figures 4.3-4.8.

Figure 4.9 shows the collection of curves corresponding to $S_w = 0.1$ obtained at different values of E^*_{cut} and hence T^*_{cut}. These provide a more comprehensive view of the effect of temperature on $G_2(r)$ (Figure 4.9 (a)) while the system is forced to seek very low bulk value for its order, and its discrete Fourier transform in

Figure 4.2: (***following page***): (a) Spatial dependence of orientational pair correlations for the LL system of lattice size $15 \times 15 \times 15$, obtained from microstates sampled at various order parameter windows, S_w (as indicated by the legend), for $T^*_{cut} = 0.55$. For comparison, $G_2(r)$ obtained from a canonical simulation performed at the same temperature (*i.e.*, equilibrium structures) is shown in black circles, and the corresponding canonical average value of S is also indicated. (b) The discrete Fourier transform of the data in (a) as a function of k_w, the wave number in scaled inverse lattice units. In (a) and (b) lines are guide to eye. (c)-(k) show representative snapshots of the system belonging to different values of S_w as indicated in the sub-caption. The color coding is dark blue for the LC spins oriented along the director, and red for the ones in the plane perpendicular to it. Please note the increasing number of blue sites as S_w increases. In each case the viewing axis is chosen to be either x, y or z for convenience of visualization.

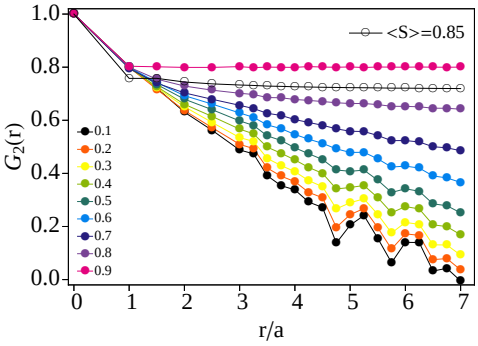

(a)

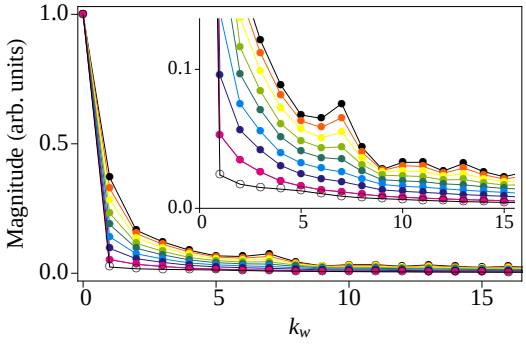

(b)

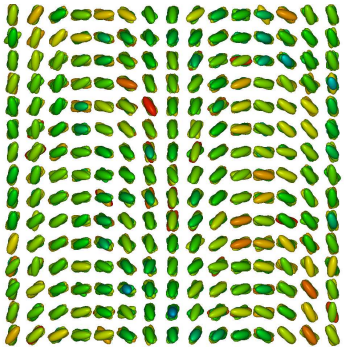

(c) 0.1

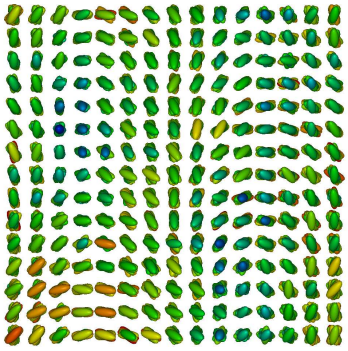

(d) 0.2

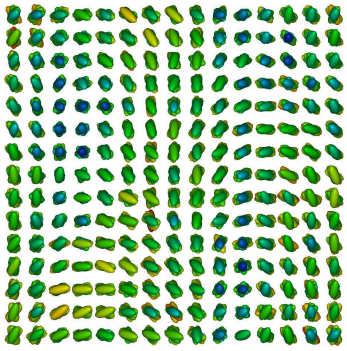

(e) 0.3

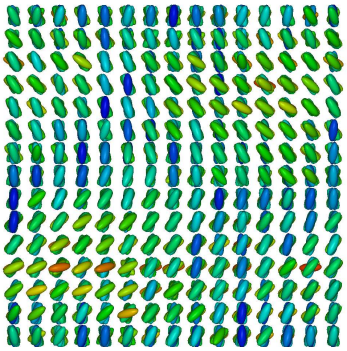

(f) 0.4

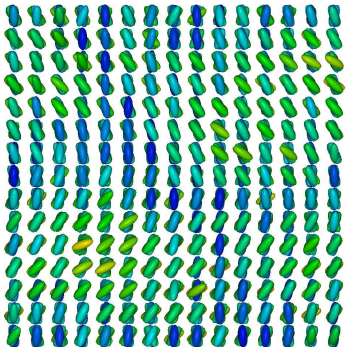

(g) 0.5

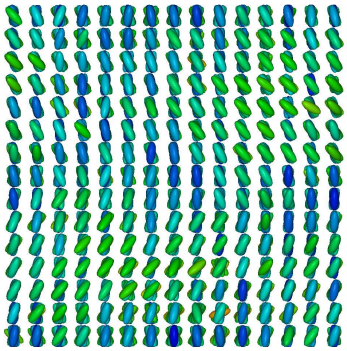

(h) 0.6

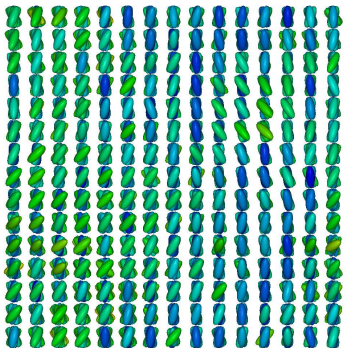

(i) 0.7

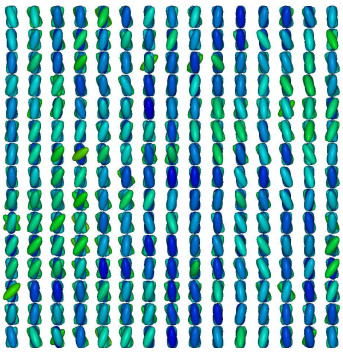

(j) 0.8

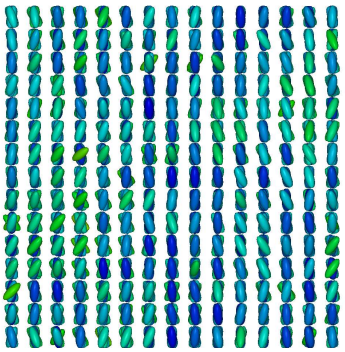

(k) 0.9

Please see the previous page for caption.

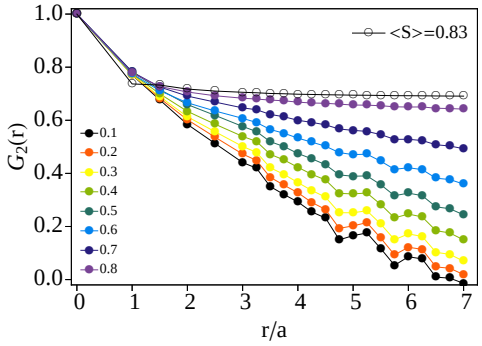

(l)

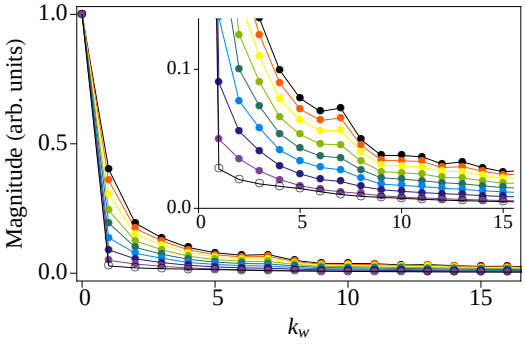

(m)

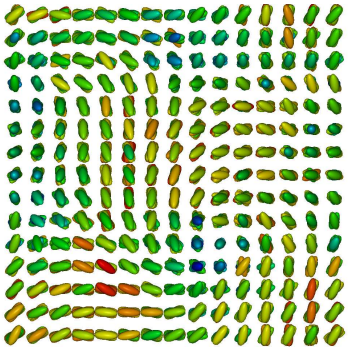

(n) 0.1

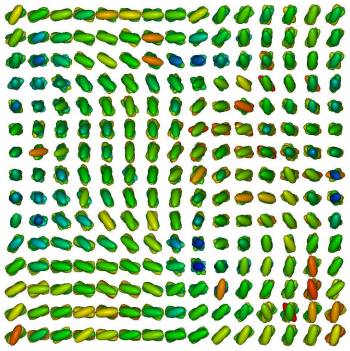

(o) 0.2

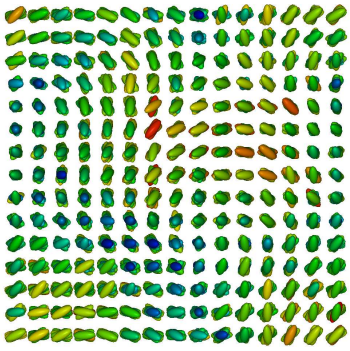

(p) 0.3

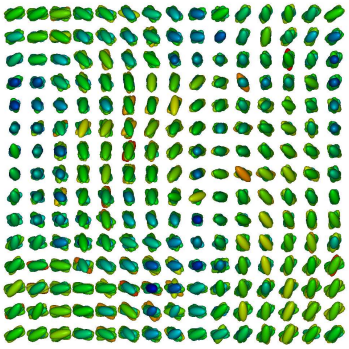

(q) 0.4

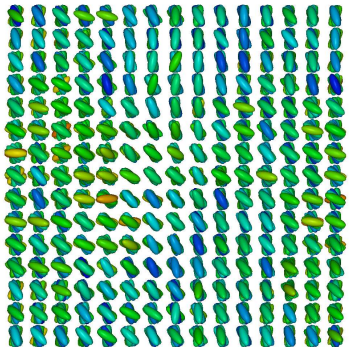

(r) 0.5

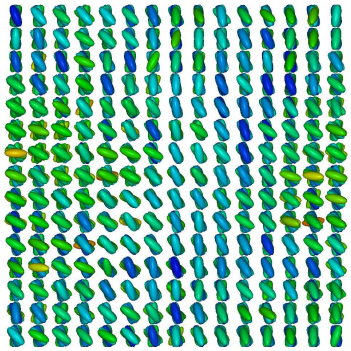

(s) 0.6

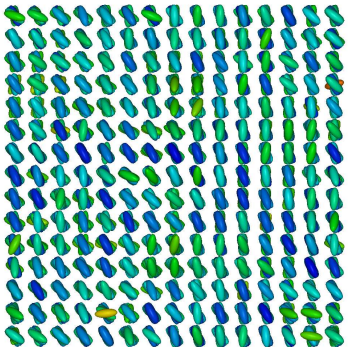

(t) 0.7

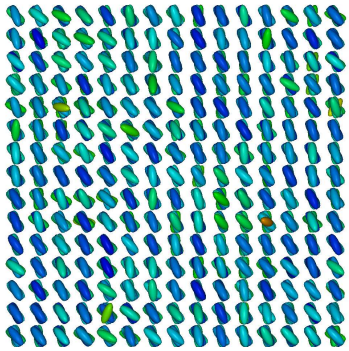

(u) 0.8

Figure 4.3: Same as Figure 4.2 at $T^*_{cut} = 0.60$.

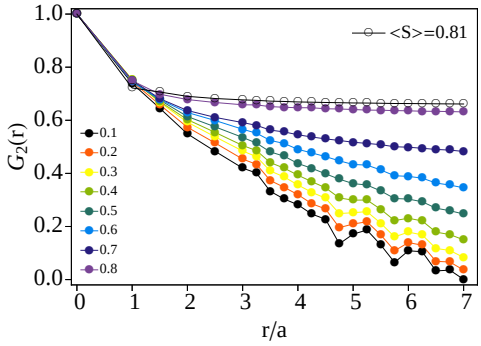

(a)

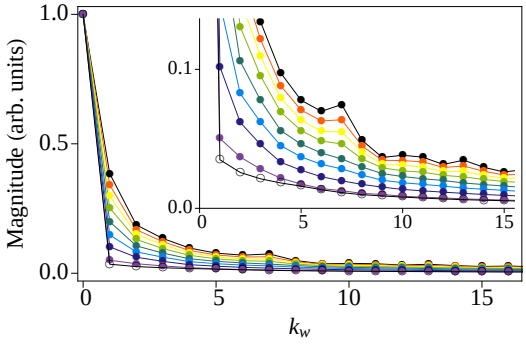

(b)

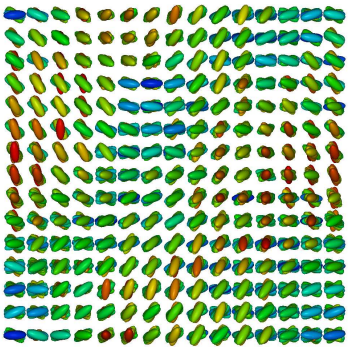

(c) 0.1

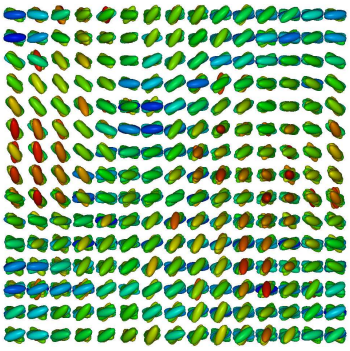

(d) 0.2

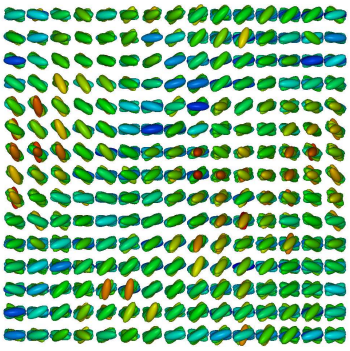

(e) 0.3

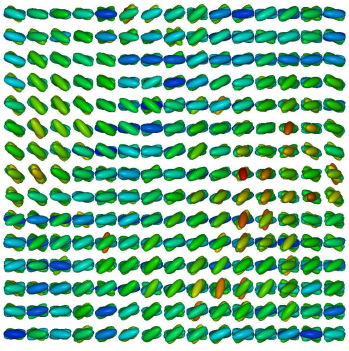

(f) 0.4

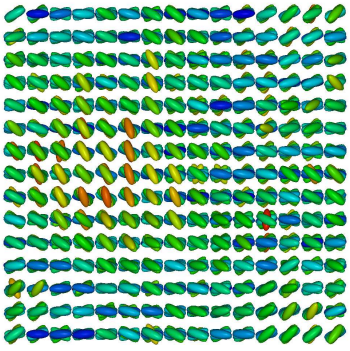

(g) 0.5

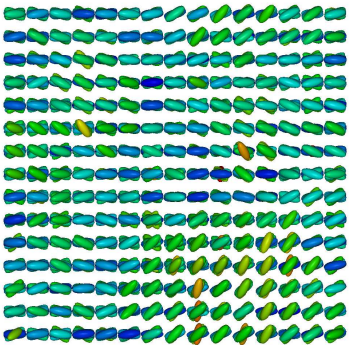

(h) 0.6

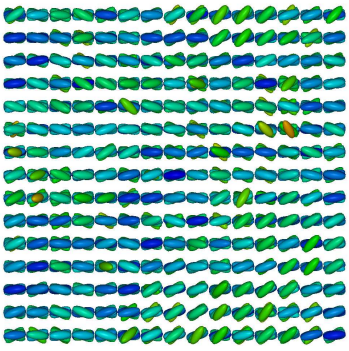

(i) 0.7

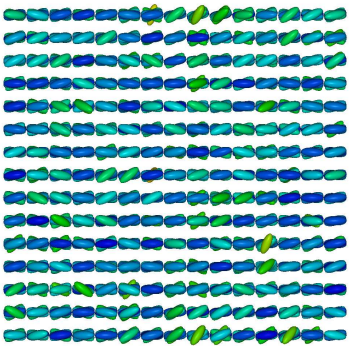

(j) 0.8

Figure 4.4: Same as Figure 4.2 at $T^*_{cut} = 0.65$.

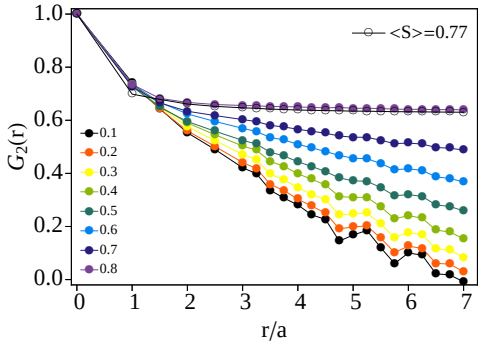

(a)

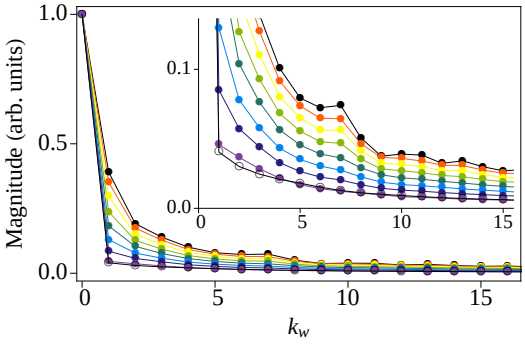

(b)

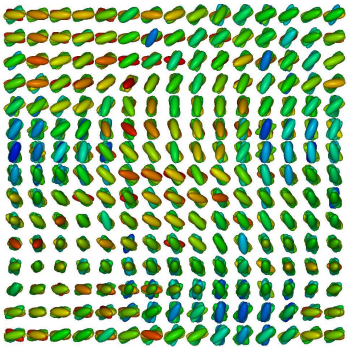

(c) 0.1

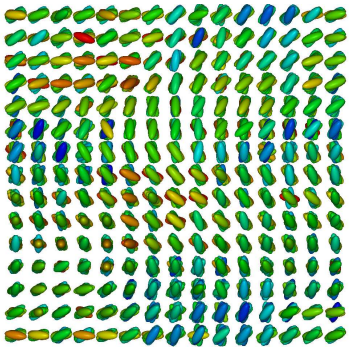

(d) 0.2

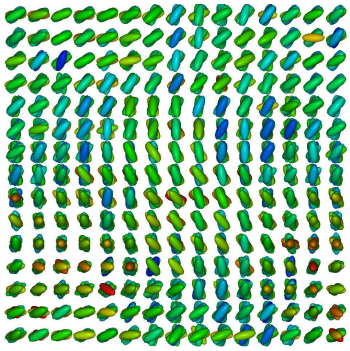

(e) 0.3

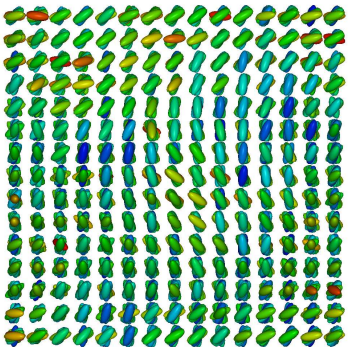

(f) 0.4

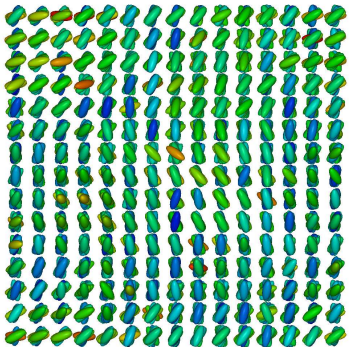

(g) 0.5

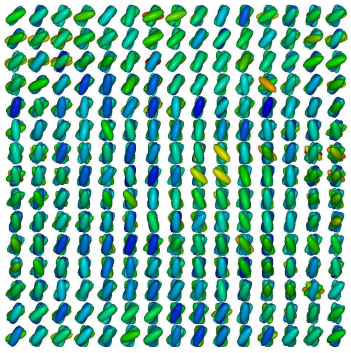

(h) 0.6

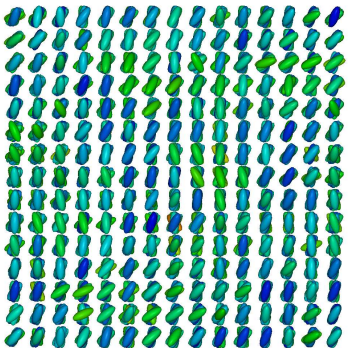

(i) 0.7

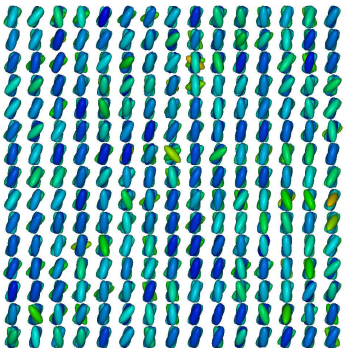

(j) 0.8

Figure 4.5: Same as Figure 4.2 at $T^*_{cut} = 0.70$.

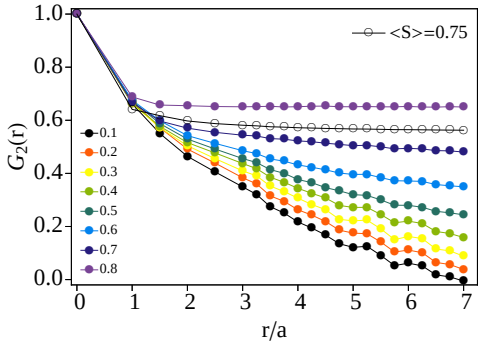

(a)

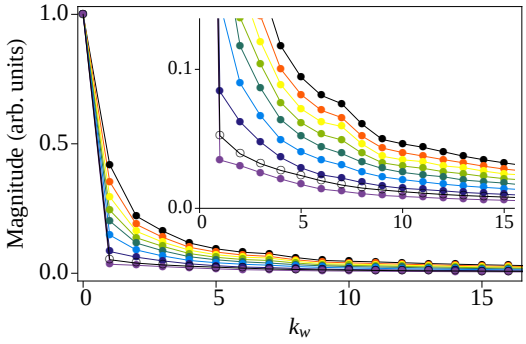

(b)

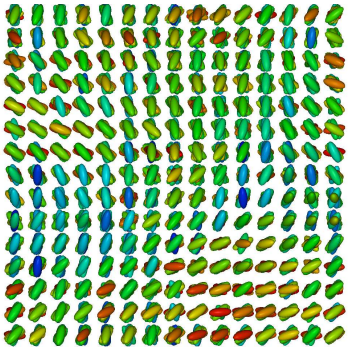

(c) 0.1

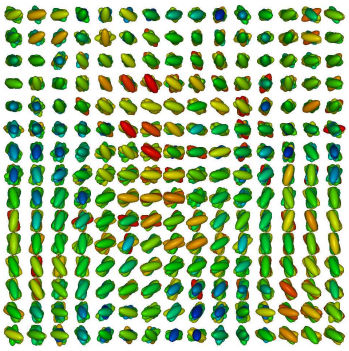

(d) 0.2

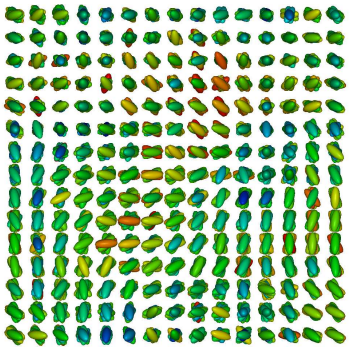

(e) 0.3

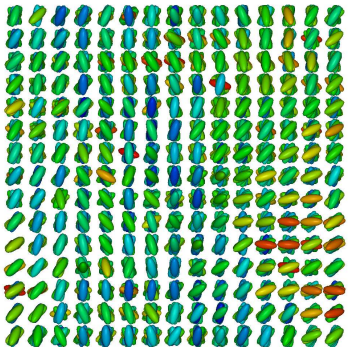

(f) 0.4

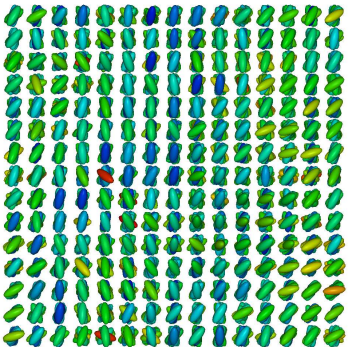

(g) 0.5

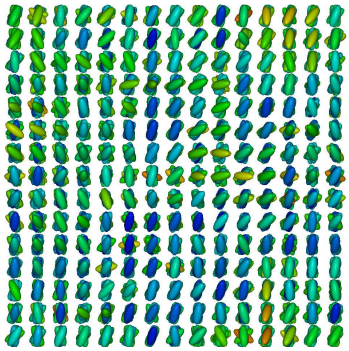

(h) 0.6

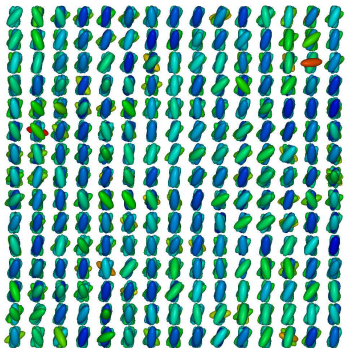

(i) 0.7

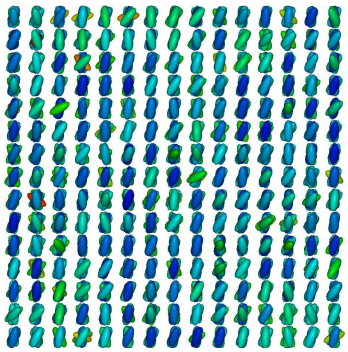

(j) 0.8

Figure 4.6: Same as Figure 4.2 at $T^*_{cut} = 0.80$.

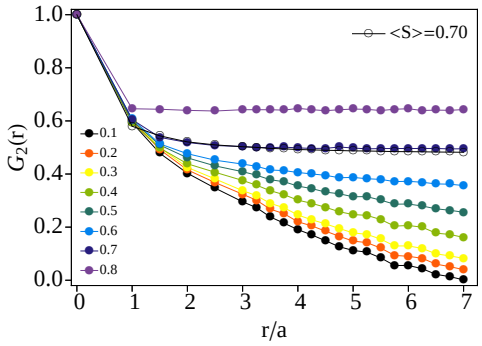

(a)

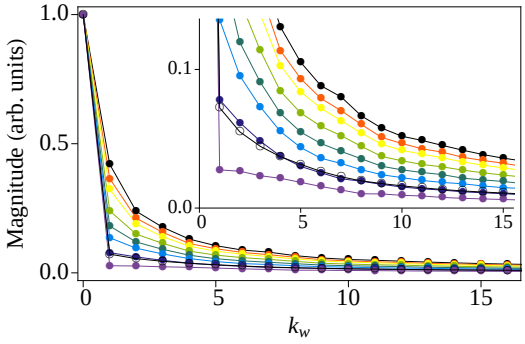

(b)

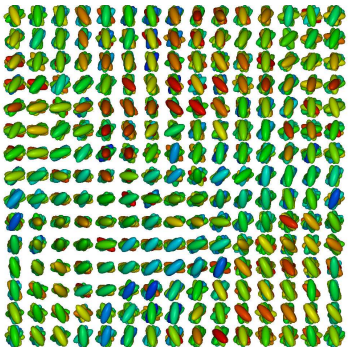

(c) 0.1

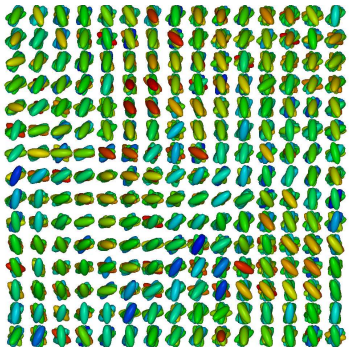

(d) 0.2

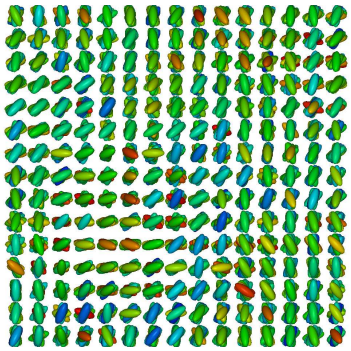

(e) 0.3

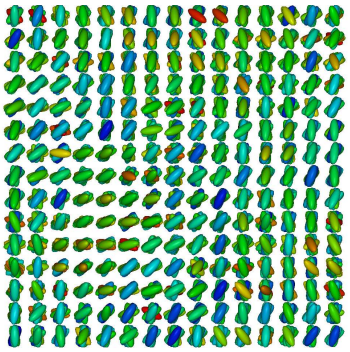

(f) 0.4

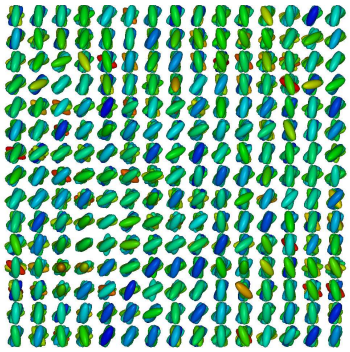

(g) 0.5

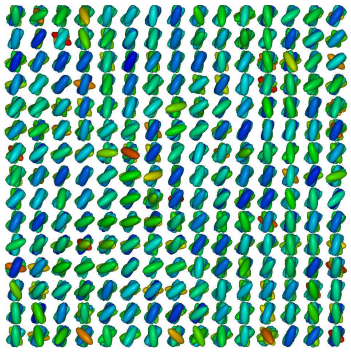

(h) 0.6

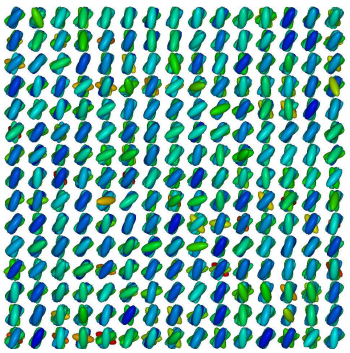

(i) 0.7

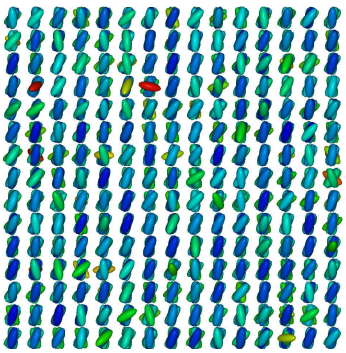

(j) 0.8

Figure 4.7: Same as Figure 4.2 at $T^*_{cut} = 0.90$.

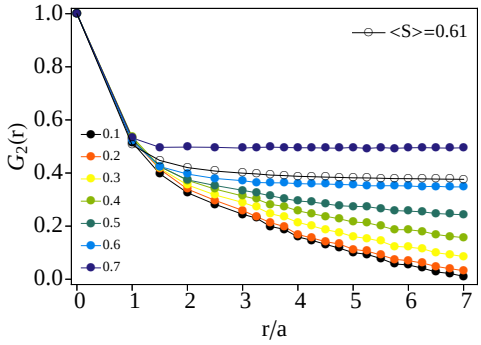

(a)

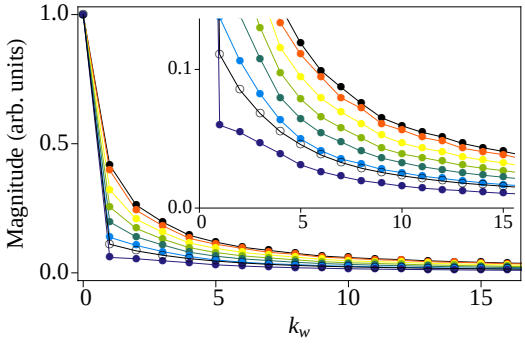

(b)

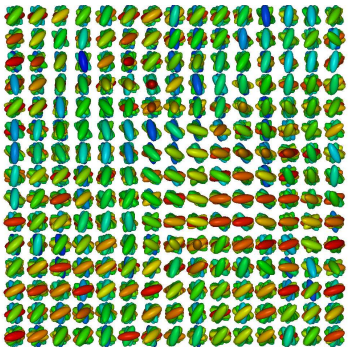

(c) 0.1

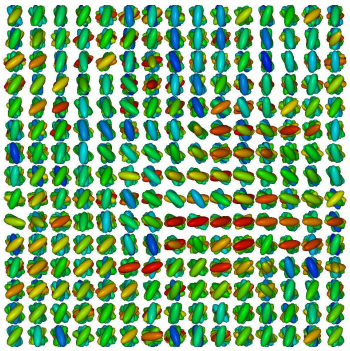

(d) 0.2

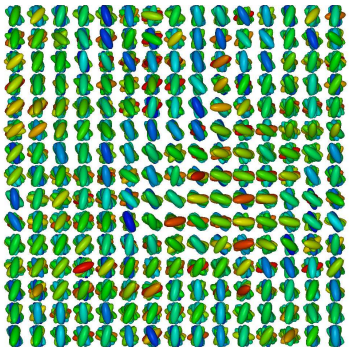

(e) 0.3

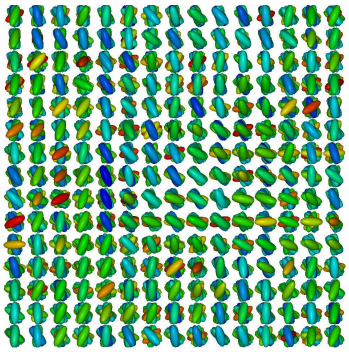

(f) 0.4

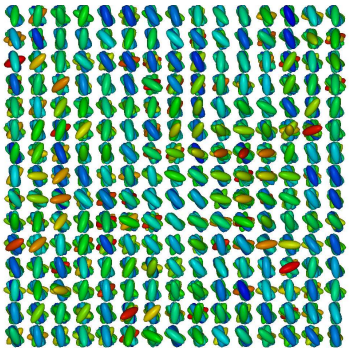

(g) 0.5

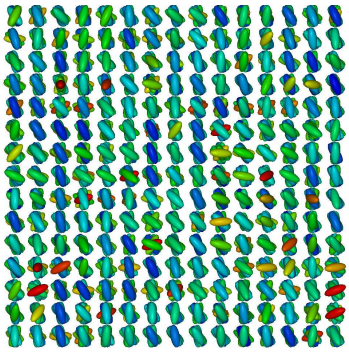

(h) 0.6

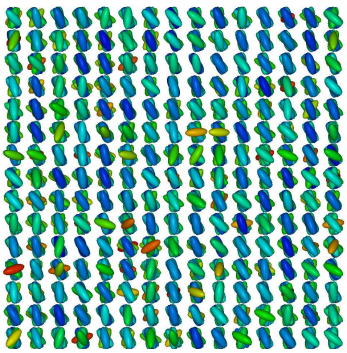

(i) 0.7

Figure 4.8: Same as Figure 4.2 at $T^*_{cut} = 1.00$.

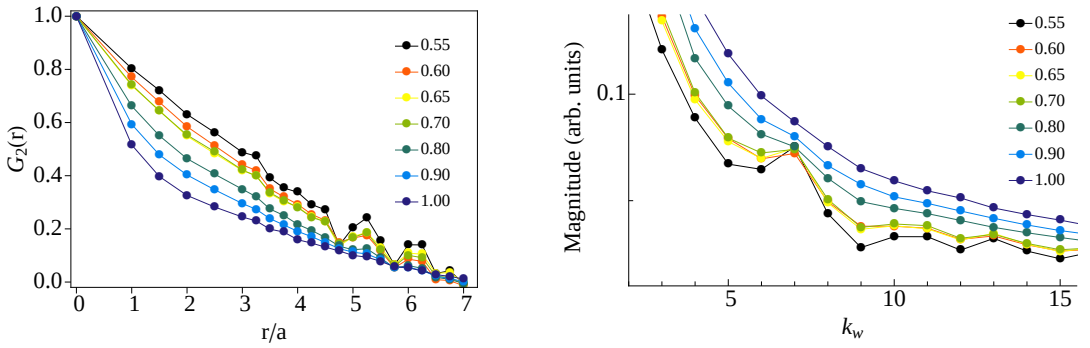

(a) (b)

Figure 4.9: (a) $G_2(r)$ as a function of r and (b) the magnitude of discrete Fourier transform of $G_2(r)$ in the wavevector space, k_w for the case of S_w=0.1, at different values of T^*_{cut}.

the k_w space (Figure 4.9 (b)). An estimation of the size of orientationally aligned domains within the sample has the potential to give qualitative information on the temperature dependence on such rare microstates [230].

Discussion

In this section, we demonstrated that one could obtain a representative distribution of microstates, $g(E)$, with respect to the order parameter of the uniaxial LC system, at any chosen energy (of course, within a narrow range). We find that the system, while respecting the energy constraint, seeks very curious director structures which yield progressively lower order as the uniform random walk along the OP-axis pushes it away from the equilibrium value.

While repeating OP-sampling at various temperatures, our interest was to examine possible differences in the director structures, on the allowed energy (and hence the equilibrium value of its order) is progressively changed. We captured systematically representative microstates at different bin values of the order, in each case, and analyzed them in terms of spatial dependence of orientational pair correlation functions, and their Fourier representations. The common feature is the progressive loss of long-range correlations as the random walk encompasses lower order parameter values. While this observation in itself is not very surprising, even though perhaps for the first time quantitatively analyzed, the change

in these correlation functions as the system is constrained at much higher orders (and hence lower energies) are very curious and illustrative. It is seen that at low enough energies (low temperatures and highly ordered equilibrium states), the OP-sampling captures rather fascinating structures which at once geometrically average the bulk value to the desired low value, while being consistent with the essentially constrained low energy. The sample develops periodic director structures in order to satisfy the competing conditions, resulting in periodic undulations on the spatial correlation functions. We estimate its k-space spectrum by performing a Fourier analysis. The amplitude spectra obtained are indicative of these coherent structures.

There has been considerable interest in the microscopic states that are obtained from deep temperature quenching in several condensed matter systems including liquid crystals [231, 232]. One of the interesting aspects is the growth of the quenched state into expectedly ordered medium consistent with the equilibrium conditions that the system is subjected. In this context, we conjecture that the realization of such (rare) microscopic structures (systematically with a well-defined algorithm) corresponding to different low energies (within the nematic medium), and at different OP value at a given energy, could be useful in exploring the kinetics of the growth of the order. These microstates, chosen for a specific objective for such investigations, could be used as initial configurations to carry out appropriate Monte Carlo simulations. One such modest attempt in the case of film with structure A (Figure 3.14) indicated qualitative difference in time scales to regain equilibrium. We now try to extend this procedure to a 2-d order parameter space, and for this purpose we study a biaxial nematic model, reported in the following section.

4.2 Biaxial system

Another system of interest is one with biaxial constituents interacting via a quadratic Hamiltonian (equations 1.39, 1.54) where the phases can be described using two order parameters, uniaxial ($R^2_{00} = S$) and biaxial ($R^2_{22} = C/2$). We wish to choose

a convenient set of model parameters (γ, λ), and carry out the OP-sampling procedure along R^2_{00} (uniaxial order along the calamitic axis). As this random walk proceeds trying to capture all microstates representing a wide range of R^2_{00} values, we monitor its R^2_{22} values. We wish to analyze the director structures of these representative microstates. The interest in doing this study is two fold: one is to extend the OP-sampling to two dimensions, and the second is to look for supportive evidences, if any, for the curious extra biaxial phase that we recently reported from this group [54].

The system studied has a size of $10 \times 10 \times 10$ lattice units with periodic boundaries on all the sides. Here we demonstrate a case simulated at a biaxial parameter value of $\lambda^* = 0.58$ which is equivalent to (γ, λ) $\sim$ (0.21, 0.12) (section 1.2.2) at the reduced temperature $T'_{cut} = 0.65$, which corresponds to a phase with considerable amount of order (both R^2_{00} and R^2_{22}) developed (please note the usage of primed symbols in the case of biaxial systems). Figure 4.10 (a) and (b) show respectively the region studied in the biaxial parameter space (γ, λ) and the temperature dependence of the order parameters in that region. With these set parameters, OP-sampling along R^2_{00} is initiated from a microstate belonging to the canonical equilibrium ensemble belonging to the region indicated in (Figure 4.11 (a)). The algorithm is then seen to sample diverse regions in the R^2_{00}-R^2_{22} parameter space, as is observed from the subsequent evolutions in Figure 4.11. Deviations in energy from E'_{cut}, corresponding to the set value of T'_{cut} is seen to be less than 0.55%. As was observed in the case of uniaxial systems described in the previous section, here too the excursions of R^2_{00} from its equilibrium value, occur slightly towards higher regions of order and to a considerable extent towards lower ordered regions, as set by the lower limit in the program. It is to be noted that in these biaxial systems, the total energy is distributed among three terms: the first term tending to align the long axes of LC constituents (uniaxial-uniaxial tensor interaction), the second term tending to align the long axis of a constituent perpendicular to the one of its neighbour (uniaxial-biaxial tensor interaction), and the third term tending to align their short axes (biaxial-biaxial interaction). Hence an increase in the value of R^2_{00} can only be allowed at the cost of a reduced R^2_{22}, explaining the pathway for R^2_{00} excursions above its equilibrium value. The decrease in the value of both

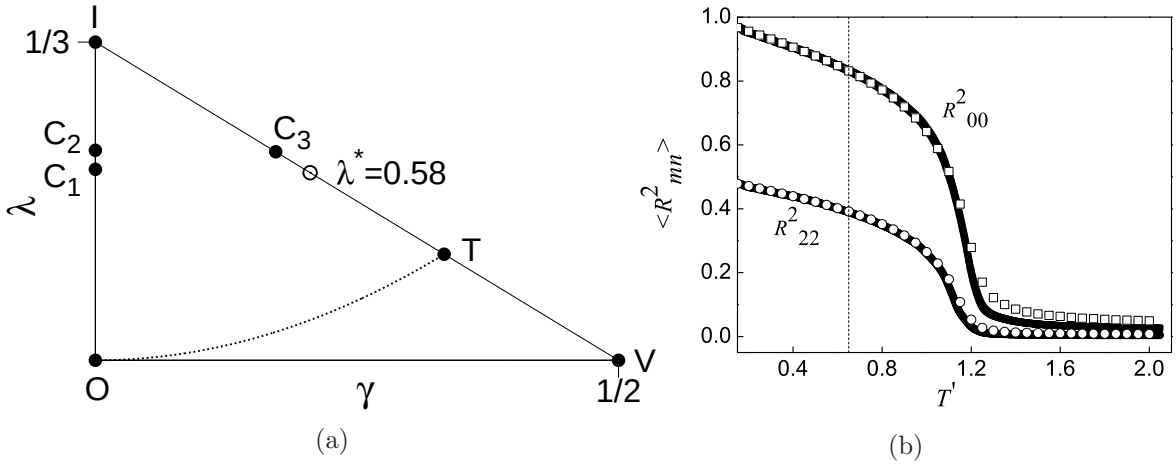

Figure 4.10: (a) The black open circle corresponds to the region of essential triangle in the biaxial parameter space (γ, λ) at $\lambda^* = 0.58$, subjected to OP-sampling (please refer to section 1.2.2 for details on essential triangle). (b) The temperature dependence of the uniaxial (R^2_{00}) and biaxial (R^2_{22}) order parameters for the point marked in (a), with a dashed vertical line drawn at reduced temperature, $T' = 0.65$. Filled and open symbols represent data obtained from energy-based entropic sampling and Boltzmann sampling, respectively.

the orders are possible by the formation of local domains. Thus the system is seen to loop around a region of the microstate space. It is worthwhile to note here that the sampling method was successful in spanning the R^2_{00}-R^2_{22} space in a reasonably exhaustive manner, though it is adequate to guide the system along the R^2_{00} space alone. A movie showing the evolution of these microstates as the OP-sampling along R^2_{00} axis proceeds is included (file: Chapter4_OP_Evolution_058.wmv) in the soft copy for further elucidation of this point.

In order to investigate the R^2_{00}-R^2_{22} microstate space sampled, nine distinct regions were chosen from Figure 4.11 (d), from which microstates are collected and $G_2(r)$ is determined along the directions of each of the three molecular axes $\{\boldsymbol{e}, \boldsymbol{e}_\perp, \boldsymbol{m}\}$. Here $\boldsymbol{m}$ represents the major axis (calamitic) and the other two are the minor axes. The averaging of $G_2(r)$ was done over ten microstates in each region and over ten random centers for each microstate. The results are depicted in Figure 4.12 which shows that the system can exist in qualitatively different forms within a very narrow band of chosen energy. Region 1 represents the canonical equilibrium configuration of the system where all the molecular axes are ordered with respect

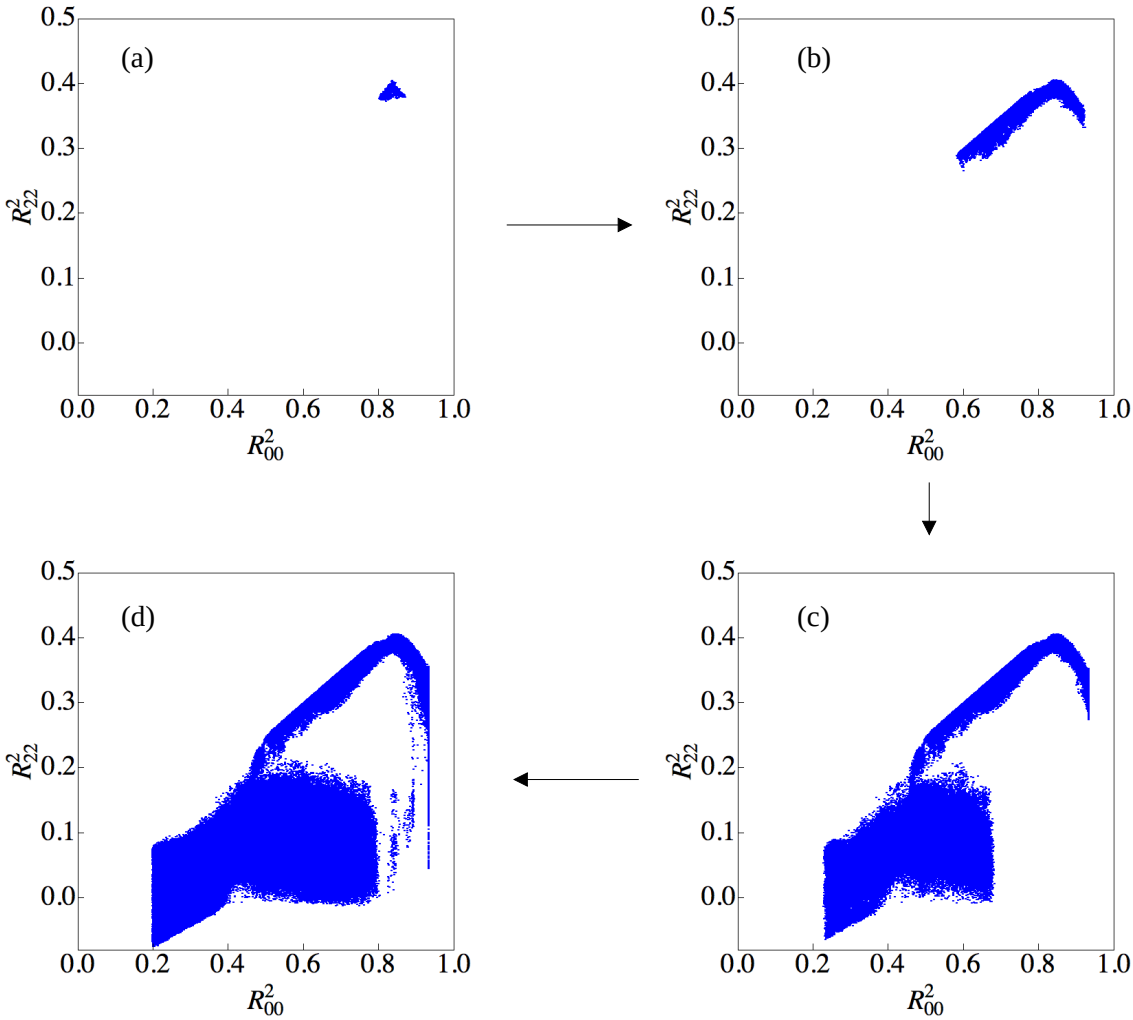

Figure 4.11: Evolution of the R^2_{00}-R^2_{22} microstate space of the biaxial system at $\lambda^* = 0.58$ and $T'_{cut} = 0.65$ during OP-sampling. (a) the initial region sampled by the algorithm which belongs to the canonical equilibrium ensemble at the set temperature. (b)-(d) show the subsequent evolution. (Here only 10% of the total data points collected is displayed.)

to each other, the calamitic axis $\boldsymbol{m}$ being the most ordered one implying a prolate biaxial state. As we move along the subsequent regions 2-5, the correlations are seen to continuously decay with distance along all the molecular axes, indicating the presence of local domains within the sample. In the regions 6-8 correlations resume to develop along one of the minor axes, $\boldsymbol{e}_\perp$, while they continue to decay along the other axes, indicating alignment of $\boldsymbol{e}_\perp$ axes alongside the existence of randomly oriented domains with respect to the other axes. Region 9 indicates all

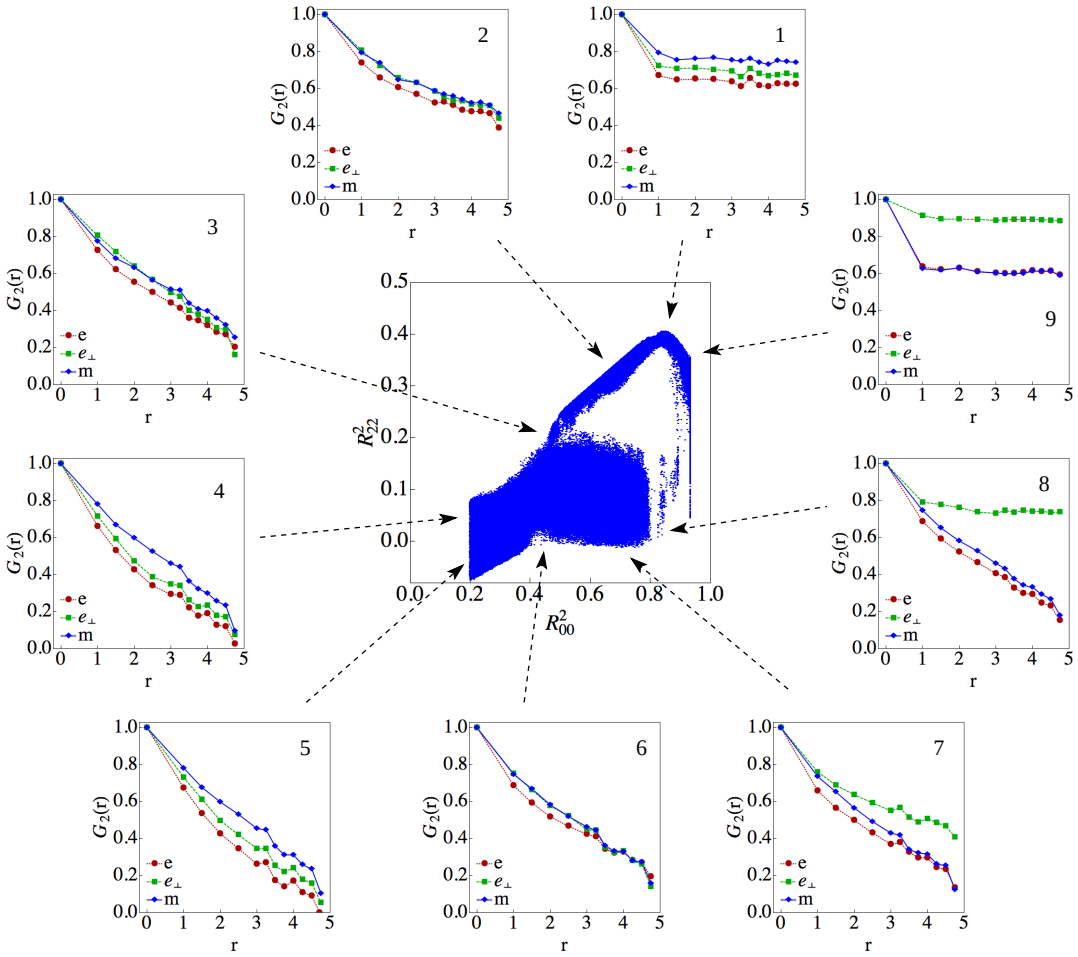

Figure 4.12: Spatial dependence of orientational pair correlations along the three molecular axes $\{\boldsymbol{e}, \boldsymbol{e}_\perp, \boldsymbol{m}\}$ for the microstates belonging to different regions of the R^2_{00}-R^2_{22} microstate space at $\lambda^* = 0.58$ and $T'_{cut} = 0.65$. Region 1 belongs to the canonical equilibrium at the set temperature.

the molecular axes ordered with respect to each other, with $\boldsymbol{e}_\perp$ having a higher degree of order thereby implying an oblate biaxial state.

The effect of the Hamiltonian parameter γ is examined by considering two more cases (apart from case A described above), case B and case C where the value of γ is reduced to half of that of case A and to zero, respectively. This trajectory corresponds to progressive decrease of uniaxial-biaxial coupling between neighbouring molecules, while leaving the other ordering terms undisturbed. The R^2_{00}-R^2_{22} microstate space sampled by the three cases are shown in Figure 4.13. It is observed that for $\gamma \neq 0$, the system revisits the initial microstates through a region of higher

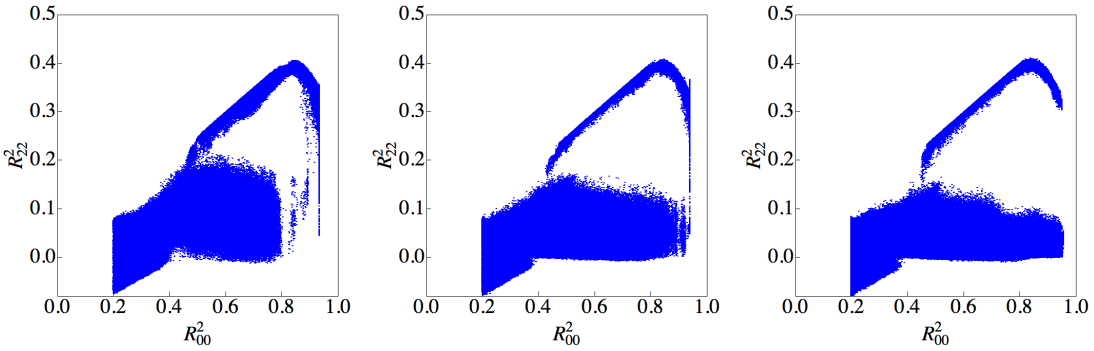

(a) (b) (c)

Figure 4.13: R^2_{00}-R^2_{22} microstate space spanned by the OP-sampling algorithm for the cases A (a), B (b) and C (c) at (γ, λ) $\sim$ (0.21, 0.12), (0.10, 0.12) and (0, 0.12) respectively at $T'_{cut=0.65}$.

R^2_{00}, while at $\gamma = 0$ (no cross-coupling term) under the same sampling conditions we could not observe a connecting return path to its equilibrium structure. For a system of even smaller size, regions of lower values of both the order parameters are seen to be rarely visited, pointing to the difficulty in the formation of randomly oriented domains due to the size restriction. Attempts to carry out similar simulation on a system of larger size proves to be prohibitive from computational point of view, and could not be successfully completed.

Discussion

While discussing the implication of the interesting collection of microstates spanned by OP-sampling in the R^2_{00}-R^2_{22} parameter space of the system confined to a very narrow region of energy, one enters two caveats. The first is that the correlation function graphs plotted in Figure 4.12 are from a representative set of limited number of microstates captured transiently as the system evolves under OP-sampling. The second is that the size of the system ($10 \times 10 \times 10$) is not satisfactory from the point of understanding these, even representative results: there could be finite-size effects inducing spurious k-space components. The collection of this data on the present system size proved to be computationally expensive, taking about six months on a contemporary processor.

Starting from location 1 in Figure 4.12, which corresponds to the equilibrium location of the system at the chosen low temperature (and hence low energy), we

find that the three axes show long-range correlations, as evidenced by the three plateau regions. It may be noted that the model parameters (γ, λ) of this system reside on the diagonal at $\lambda^* = 0.58$. The pair-wise interaction on the diagonal exhibits D_{4h} symmetry about the molecular $\boldsymbol{e}$ [54], and the large values of R^2_{00} and R^2_{22} corresponding to the region (~ 0.85 and 0.40, respectively) indicate a well-ordered biaxial phase, consistent with this data.

As the OP-sampling is initiated starting from a microstate corresponding to this equilibrium point, the system somewhat readily visits regions in the R-space corresponding to lower R^2_{00} values (Figure 4.11 (b)). From Figure 4.12, correlation function graphs of region 9, we see that these results are qualitatively different from the microstates of region 1. In this higher value region of R^2_{00}, we see rather dramatically, that the molecular $\boldsymbol{e}_\perp$ axis has emerged as a clear calamitic axis, while the correlation of the other to axes are looking identical. The fact that the OP-sampling procedure is needed to push the system to this state indicates that this is not the equilibrium director structure, even though somewhat more readily accessible. Keeping in view the permutation symmetry of the Hamiltonian with respect to the indices of the molecular axis [39], and the hypothesis that all such choices of (γ, λ) can always be mapped suitably with the interior of the essential triangle, we conjecture that this could correspond to a plausible equilibrium state of another coordinate point within the region of biaxial stability. We suggest that this could be a point on the diagonal of the image of the triangle in the 2^{nd} quadrant ($1 + 2\gamma - 3\lambda = 0$). On this diagonal the Hamiltonian exhibits a pair-wise D_{4h} symmetry along the molecular $\boldsymbol{e}_\perp$ axis.

The progression of microstates towards the lower regions of R^2_{00} and R^2_{22} are accompanied by the loss of long-range order of all the molecular axes (Figure 4.12, regions 2–6). We conjecture that the irreversible transition from region 3 into the low R^2_{22} regions, corresponds to the system accessing states which are predominantly uniaxial. The progression of OP-sampling indicates a build up of long range order of molecular $\boldsymbol{e}_\perp$ axis, relative to the other two, alluding to the development of a uniaxial phase with ordering director being associated with $\boldsymbol{e}_\perp$ axis. The progression of the system from region 7 to 9 *via* isolated region like 8, appears

to be corresponding to a transition triggering the onset of biaxial ordering of the system with the major eigen vector of the ordering tensor associated with the $\boldsymbol{e}_{\perp}$ axis defining the calamitic director.

The above plausible mapping of different regions of R^2_{00}-R^2_{22} microstates space to different types of macroscopic symmetries of the director structure is very interesting, and indicates the variety of in-principle accessible states to the system, commensurate with the set energy. In Figure 4.13, we show similar microstate maps for two more points in the Hamiltonian parameter space, as the value of γ (strength of the cross-coupling term in the model) is reduced to zero in two equal steps. Figure 4.13 (b) shows a very similar progression of microstates takes place as in Figure 4.13 (a), but for the difference that the development of the initial order (lower branch of the map) proceeds to a higher value, before the system is driven (under OP-sampling) to assume biaxially symmetric states. Figure 4.13 (c) does not exhibit a similar return path (through isolated islands), but it could as well be due to the maximum limit on R^2_{00} that has been set during the OP-sampling.

In view of the efficiency of this sampling procedure to look at closely the distribution of the microstates in the R^2_{00}-R^2_{22} plane in a biaxial nematic system (at chosen energy), we envisage its applicability in throwing perhaps some useful light in resolving issues connected with director distribution in systems with partly repulsive Hamiltonian [39, 54, 233].

Chapter 5

Effect of external field in bulk nematic systems

This chapter investigates the effect of an external field on the phase transition temperatures in uniaxial and biaxial nematic systems. Our studies on uniaxial nematics are motivated by earlier experiments which indicated an initial linear regime followed by a quadratic dependence of the NI transition on an external field, (assuming for example, positive dielectric anisotropy). The phenomenological explanation offered appeals to the quenching of director modes by the applied field, initially in a linear way. The resultant loss of entropic contribution leading to the corresponding increase in the free energy is argued to be the reason for the experimental observations. In this context, it is thought to be a worthwhile task to generate the experimental data through MC simulations, and examine if the computer-based experiments based on a simple and well accepted model (like the LL interaction) could support real experiments. This is particularly interesting that simulations, which are based on microscopic interactions with only nearest neighbours, are expected to mimic mesoscopic manifestations (alluded to in the phenomenological arguments) to account for the actual observations. Such an exercise of course would require very high precision in temperature to be able to detect very subtle changes in the NI transition temperatures on the application of very small fields ($\sim$ one part in 10^4). We employed entropic sampling method to achieve this resolution, and this chapter reports on findings in the uniaxial system.

Such studies on biaxial nematics, with intrinsic molecular level biaxiality, are rare; and there are two transitions (I-N_U and N_U-N_B) to be examined. Further consideration of biaxial molecules requires additional Hamiltonian parameter space, accommodating the resulting extra terms in the model. It will be worthwhile to investigate the dependence of the transition temperatures from the uniaxial to the biaxial phase in systems with differing couplings between the two molecular

tensor components. These are to be clearly distinguished from the biaxial symmetries induced in the uniaxial systems with negative dielectric anisotropy, under the influence of external fields. We report in this chapter such simulational studies, with different choices of interaction parameters in the general quadrupolar biaxial Hamiltonian.

5.1 Uniaxial system

Coupling of an electric field to the anisotropic LC medium leads to controllable molecular orientation. Its manifestation is two fold as far as the NI transition is concerned. Firstly the isotropic phase acquires a small orientational order in the presence of the field, and we refer to it as paranematic phase to distinguish it from the isotropic phase. Secondly, the transition from this higher temperature phase to the nematic phase is affected. At low enough fields, the transition temperature is enhanced proportional with field. And, beyond a threshold value a critical point is reached where the first order transition disappears. The consequent changes in the (dis)order show up as observable variation in different physical properties, indicating new phases, and other field induced critical effects [234]. The effect of the applied electric field on the paranematic-nematic transition temperature (T_{PN}) was investigated experimentally in LCs with both positive and negative dielectric anisotropies [74–77, 217, 234–239]. The nature of the transition is affected differently owing to the qualitative difference between the ordering directions induced by intermolecular interactions on one hand and the coupling of the molecules with the field on the other [15]. However, in both the cases it was experimentally observed that T_{PN} increases linearly for small applied fields contrary to the expectation based on the Landau-de Gennes energy considerations, which in fact predicts a quadratic dependence, *i.e.*, $T_{PN}(E_f) - T_{NI}(0) \propto E_f^2$, where $\mathbf{E}_f$ is the applied field (please refer to section 1.4.2). Such a quadratic dependence is predicted also by the thermodynamic relations near a first order transition through Clausius-Clapeyron-type dependence [74]. The origin for this unexpected result (at low fields) is attributed to the quenching of director fluctuation modes by the

applied field, leading to additional initial dependence on the field which turns out to be linear. Of course experimental detection of this subtle effect needs application of very low fields and hence require experimental facilities to measure rather very small shifts (typically one part in 10^4) [5]. The enhancement in the free energy, ΔF due to the loss of entropy resulting from the quenching of long wavelength director modes was calculated phenomenologically by introducing two length scales: the electric coherence length $\xi(E_f) \propto 1/|E_f|$ (section 1.4.2) and the cut-off wave vector $q_c \propto 1/l$ (l is of the order of the molecular dimension). The enumeration of the modes in the presence of these two bounding cut-off wave vector amplitudes, needed to compute the decrease in the entropy at an applied field E_f, leads to an increase in the free energy [5]

$$\Delta F = \alpha|E_f| + \delta E_f^2 \,. \tag{5.1}$$

Here $\delta << \alpha$, leading to prominent linear dependence on E_f in the low field regime. The experimentally observed linear shift in T_{PN}, in the field range up to 10^7 V/m, is within 0.6 K for medium with positive dielectric anisotropy and within 0.2 for that with negative dielectric anisotropy.

In this context, the present work reports Monte Carlo simulation results on the variation of the paranematic-nematic transition temperature with applied field [169]. The motivation is to see if the experimental observations bearing the signatures of hydrodynamic length scales, could be simulated based on microscopic interactions taking place on molecular length scales. A possible success in this attempt would signal an important, and qualitatively significant step forward in the applicability of such models. We used the well studied lattice-model (Lebwohl-Lasher) potential to simulate the results, augmented with a dielectric energy density contribution with the usual quadratic dependence on the field. The interest is to investigate if a linear dependence emerges from such a model at low enough fields. The challenge of achieving a high precision in the temperature variation during simulation was met by employing the entropic sampling method [155, 156] (see Chapter 2), thereby achieving temperature resolution of the simulated results comparable to the experiments.

Since the nematic-isotropic transition is primarily connected with the orientational degrees of freedom, and in view of the wide acceptance of the simple lattice model based on the Lebwohl-Lasher interaction [93] to capture the essential features of the NI transition, we adopt this model here. Accordingly we consider a cubic lattice of size $20 \times 20 \times 20$ imposing periodic boundary conditions to minimize the finite size effects, and the interactions among the lattice sites are restricted to only the nearest neighbours as usual. We use this model for the present work, supplemented by the interaction term (assuming a positive dielectric anisotropy of the medium) with the applied electric field (please refer equation 1.53). Due to the assumed positive dielectric anisotropy of the system, the applied field favours parallel alignment of the long axes with the field. After obtaining the density of states (DoS) with respect to E at a given field value as described above, several independent energy-uniform random walks were performed to collect a number of entropic ensembles, each consisting of 3×10^7 microstates. This extensive collection of microstates comprising of entropic ensemble was found necessary to improve the statistical confidence interval of the data to meet the experimental conditions. Computation of the different physical quantities, averaged over several canonical ensembles constructed under identical conditions yielded accuracies in the location of the C_V peaks determining the transition temperature, compatible with the experimental errors in the temperature measurement. Canonical ensembles so extracted have at least 7×10^5 microstates near the transition. Transition temperatures are determined from the peak position of specific heat C_V plotted as a function of temperature at each field value. T^*_{PN} values obtained from several such canonical simulations (at a given T^* and E_a) are further averaged so as to yield an error not exceeding 3×10^{-4}.

The shift in the temperature on the application of the field, $\Delta T^*_{PN} = T^*_{PN}(E_a) - T^*_{PN}(0)$, determined from the positions of the C_V peak, is shown as a function of E_a in Figure 5.1. As may be observed, there are two distinct regions of variation of this shift with the field. For low values of the field (≤ 0.04 in simulation units), the temperature shift is linear, tending to become quadratically dependent at higher values. As is shown in the inset of the figure, a linear fit seems to be appropriate

in the low field region. The high-field regime fits very well to a polynomial in E_a of order 2, in line with confirming the expected variation from the dielectric energy.

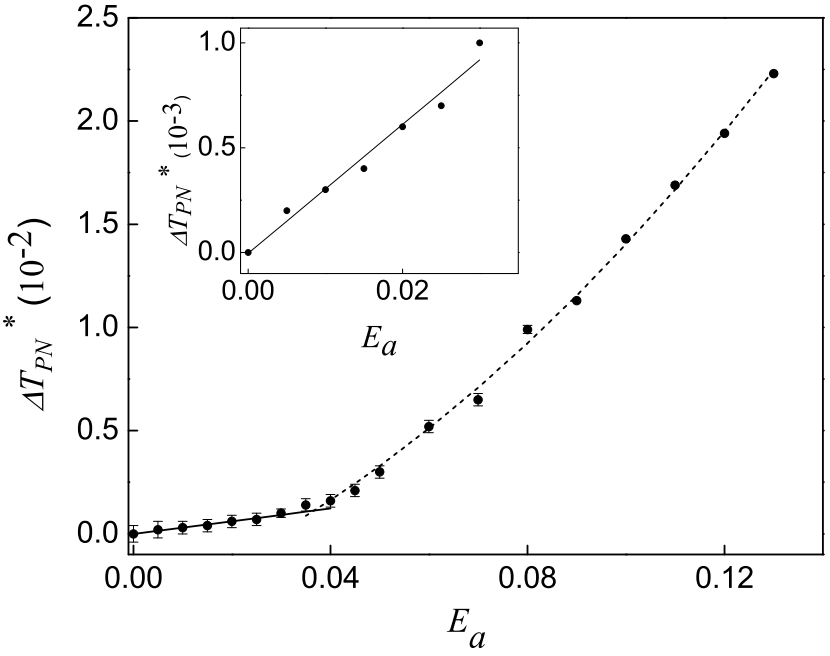

Figure 5.1: Variation of ΔT^*_{PN} with field (solid line is a linear fit and dashed line is a quadratic fit to the data in the low and high field regimes respectively). The inset focuses on the variation in the low field regime.

The variation of C_V with temperature at various fields is shown in Figure 5.2(a). It is observed that near and above $E_a \sim 0.15$, the C_V peak flattens considerably indicating softening of the transition in the presence of high enough fields. Of course this also makes the determination of the T_{PN} (at those high values) relatively more prone to errors. In fact in a positive dielectric liquid crystal medium, the trajectory of the transition with field is expected to end in a critical point. Our results are in agreement with reports on a system of 1000 particles with similar interactions wherein the critical value of E_a^2 was reported to be well below 0.2 [238]. The experimentally observed critical electric field for 5CB is 1.41×10^7 V/m [75] which gives an estimate of the corresponding value in simulation units to be at $E_a \sim 0.23$. The detection of transition temperatures from the simulation data at this high value of field remains difficult due to the above mentioned reason.

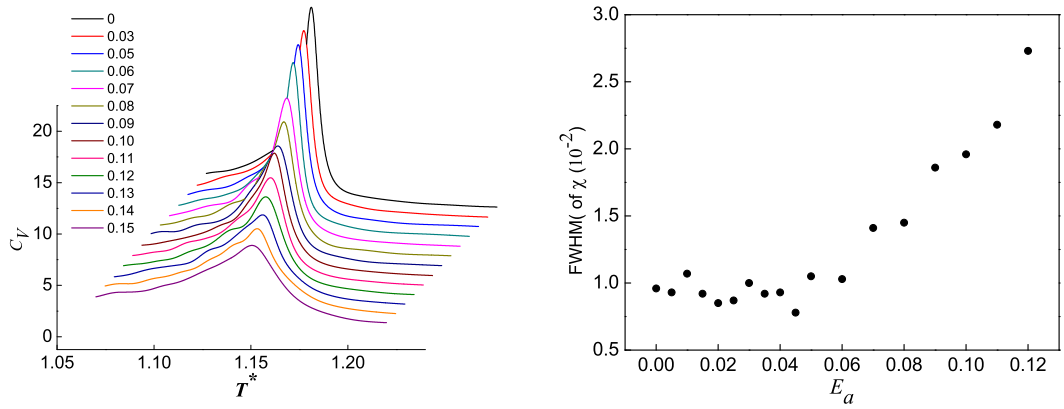

Figure 5.2: (a) Temperature variation of specific heat at various fields. (b) Variation of the widths of nematic susceptibility (FWHM) with applied field.

The softening of the transition with the increase of the applied field is also seen from the variation of the width *i.e.*, full width at half maximum (FWHM) of the nematic susceptibility (χ) (computed from reweighting results of a single entropic ensemble) and is shown in Figure 5.2(b). This width remains almost constant in the lower field regime (consistent with linear temperature shift) and increases at the higher field values. This seems to indicate that the thermally driven fluctuations in the order near the PN transition are effectively quenched at the lower values of E_a.

The field dependence of energy at a temperature just below the PN transition is shown in Figure 5.3 (solid circles). The corresponding values of entropy computed from the DoS data *i.e.*, $\log(g(E))$ is also shown in this figure (open triangles). It may be noted that the values of the entropy shown are representative being accurate to within an additive constant, and are obtained by appropriate normalization of the DoS over the chosen energy range. It is remarkable that despite the quadratic dependence of the energy on the applied field introduced through the Hamiltonian, the macroscopic energy and consequently the associated entropy, show striking linear behaviour at low fields conforming both the experimental observations, as well as lending support to the phenomenological view point of partial quenching of director modes over a length scale determined by the interplay of the applied field strength and the elastic constant.

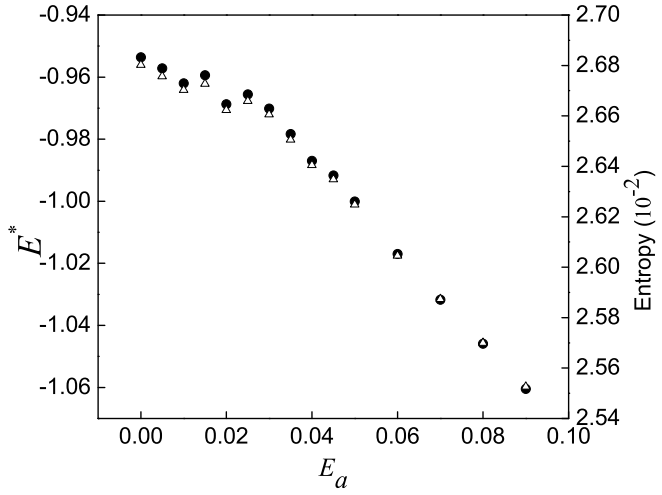

Figure 5.3: Energy per lattice site (solid circles) and the corresponding representative entropy (open triangles) versus applied field at $T^* = 1.1239$ (just below T^*_{PN} corresponding to $E_a = 0$).

5.2 Biaxial system

Effect of an external field on the phase transitions in biaxial systems has been subject of earlier studies based on Landau-de Gennes expansion of the free energy, with terms upto sixth order in order parameter [17]. Typical phase sequence in such systems on cooling is: I-N_U-N_B. The prediction from this analysis is that, for materials with positive dielectric anisotropy, the high temperature transition (IN≡IN_U) is enhanced on the application of the external field, coupling to the major long molecular axes. The case of the second transition between is curious: depending on the choice of the parameters in the Landau expansion, the transition temperatures with the application of the field, could be enhanced, or suppressed, or may be even independent of the field. These predictions were also verified by carrying out lattice-based MC simulations on a quadrupolar Hamiltonian [17] within the dispersion approximation [8]. Under this simplification, only a simple model parameter (λ_d) is needed to specify the Hamiltonian. MC simulation at $\lambda = 0.3$ have been carried out earlier [17], and the results are in partial confirmity with the free energy based predictions. With this choice of λ_d, the system

exhibits an enhancement of the temperature, T'_{PN} with the increase of the applied field. The T'_{UB} (uniaxial to biaxial transition temperature) however is very weakly field-dependent, and in fact is suppressed slightly with increase in the field strength. From these studies it is clear that the $N_U N_B$ transition, characterized by the appearance of a biaxial symmetry of the medium (even without field), is affected by the field qualitatively differently, and the prediction that its variation could go either way depending on the Landau free energy parameters is curious. They also observed that molecular mean field approach and lattice-based computer simulations using a dispersion Hamiltonian [8], where a single relative biaxiality parameter (λ_d) determines the intermolecular interaction, shows an agreeing behaviour of shift in T'_{PN} whereas (T'_{UB}) decreases with E_a (for $\lambda_d = 0.3$) as against its non-universal shift predicted by phenomenological approach. To *et al.* [19] studied the effect of external magnetic field on T'_{PN} and on the degree of order induced in the paranematic phase (Cotton-Mouton effect) using the dispersion Hamiltonian over a range of λ_d values, and also by using a Landau-de Gennes-type free energy expansion based on a single composite order parameter. In their study, a comparison was made with one of the first observations of substantial magnetic field effects on the isotropic to nematic phase transition temperature [79]. The reason for this achievement is being stated to be the ability to use high magnetic fields of upto 31 Tesla, and the properties of the bent core material used (indicating an implied biaxiality due to the bent-structure and the observed decrease in the difference between T_{NI} and the supercooling temperature) which had a better coupling with the field unlike the conventional rod-shaped LC molecules. Goshal *et al.* [240] have also studied the shift in T'_{PN} under the external field using the dispersion Hamiltonian via lattice-based Monte Carlo simulations. Molecular dynamics studies based on biaxial Gay-Berne particles were done on bulk systems to find the effect of switching in bulk systems under an external field applied transverse to the calamitic axes of molecules [6].

In this context, we take up a study of the biaxial system in its generality (employing two model parameters) (see equation 1.54), and examine the dependence of the biaxial transition temperature with field on the coupling parameter γ, which

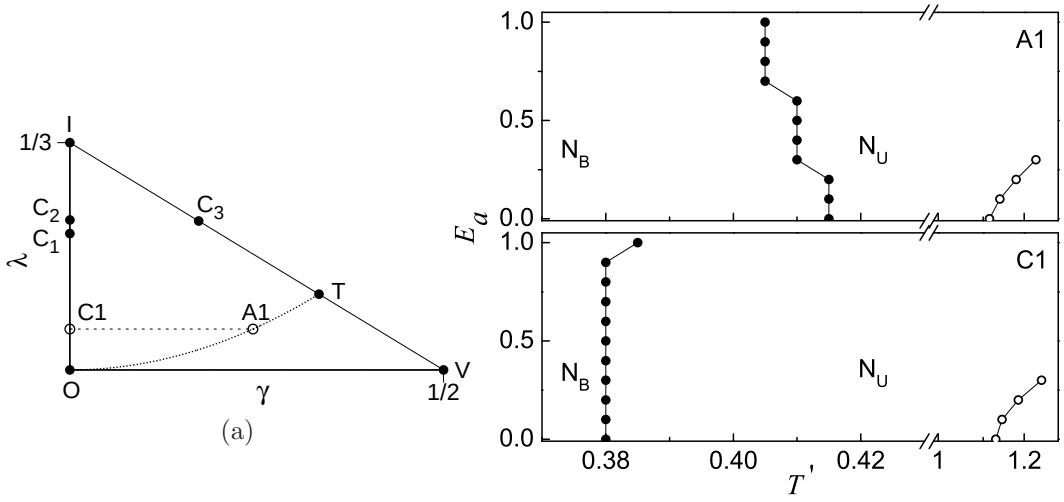

Figure 5.4: (a) Open circles mark the region under study in the biaxial parameter space (γ, λ). $A1 \approx (0.245, 0.06)$ corresponding to $\lambda_d = 0.3$ on the dispersion parabola; $C1 \approx (0, 0.06)$. (b) shows the field dependence on the transition temperatures T'_{PN} (open circles) and T'_{UB} (filled circles) for the cases A1 (top) and C1 (bottom) respectively. Discretization of the data points is due to the low resolution of temperature. Please note the break on the temperature axis.

determines the extend of coupling of uniaxial and biaxial components of the neighbouring molecules. Before proceeding with this objective we carried out MC simulation on the dispersion model itself at $\lambda_d = 0.3$ and reproduced the result of the earlier work [17] with a much bigger lattice size.

The simulation box studied has a size of $40 \times 40 \times 40$ with periodic boundary conditions on all the sides. It is seen that for all the chosen Hamiltonian parameters T'_{PN} increases with external field until a critical point is reached where the transition vanishes. The point chosen on the parabola (A1 in Figure 5.4(a)), represents the Hamiltonian with (γ, λ) = (0.245, 0.06), and corresponds to $\lambda_d = 0.3$ [8]. From Boltzmann sampling studies it is seen that the effect of the application of the field is to shift T'_{UB} to lower values, as shown in Figure 5.4(b) (top), in agreement with earlier studies [17]. This means that the field introduces more disorder into the system and requires a further cooling of the system to set in the biaxial order. While such a behaviour appears to be unusual in an ordering transition, here one

needs to consider the fact that the Hamiltonian hosts a term with parameter γ (equation 1.54), which provides a cross coupling between the uniaxial and biaxial tensor components. To clarify this matter further, we now choose another point C1, which is a projection of this point (on the parabola) on to the λ axis. Thus we retain the same biaxial-biaxial coupling, but eliminate the cross-coupling term. It is seen that for this case C1, the effect of the field is relatively weak, and if at all it shifts T'_{UB} to higher values, as is shown in Figure 5.4(b) (bottom). This shows tellingly the effect of the parameter γ in influencing the slope of the shift in T'_{UB} with applied field. The variation of T'_{PN} for both the cases is shown in the inset. It can be observed that a considerably large field is required to induce notable shifts in T'_{UB} as compared to that of T'_{PN}.

The second study focuses on two points in the (γ, λ) space: A2= (0.26, 0.16), and C2= (0.0, 0.16) as shown in Figure 5.5. A2 is a point on the diagonal of the essential triangle, and envisages two close transitions: I-N_U-N_B. It also is on the line of uniaxial torque about the molecular minor axis, $\boldsymbol{e}$ [41]. As such, the pair-wise interaction in a lattice model, at this point of the Hamiltonian, exhibits a D_{4h} symmetry [41]. It may be interesting, under the circumstances to couple the field to the molecular long axes, $\boldsymbol{m}$, thereby breaking this D_{4h} symmetry. The point C2 is on the λ axis corresponding to the projection of A2. We now discuss the results of our simulations on systems corresponding to these points, with two perspectives. The first is the examination of the effect of coupling of the field on the ordering tensors of the three molecular axes, as a function of temperature. The second is the effect of the field on the phase transition temperature, in particular of $N_U N_B$ transition.

We monitor the maximum eigen values in each of the ordering tensors of the three molecular axes (say δ_e, $\delta_{e_\perp}$, δ_m), averaged over the MC runs after equilibration, as a function of temperature at different values of the applied field in the range (0, 1.0) in steps of 0.1 (in the simulational units). We assign the ordering of one of these molecular axes as defining the primary director, depending on the maximum of the set (δ_e, $\delta_{e_\perp}$, δ_m) at each temperature, and the corresponding ordering direction is designated as 1, 2 or 3 (k-index), corresponding to $\boldsymbol{e}$, $\boldsymbol{e}_\perp$ or

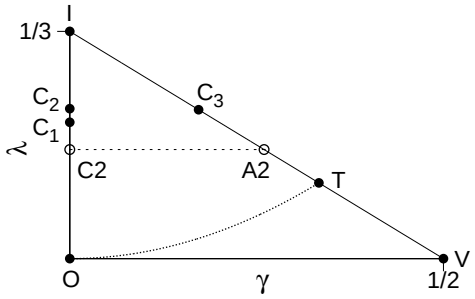

Figure 5.5: Open circles mark the region under study in the biaxial parameter space (γ, λ). $A2 \approx (0.26, 0.16)$ corresponding to $\lambda^* = 0.65$ on the diagonal of essential triangle; $C2 \equiv (0, 0.16)$.

$\boldsymbol{m}$, respectively. We also compute the order parameters R^2_{00} and R^2_{22}. We depict these in a series of plots shown in Figure 5.6. For example, Figure 5.6(a) shows these results for the point A2, with no external field. The eigen value plots clearly show the equivalence of molecular $\boldsymbol{e}_\perp$ and $\boldsymbol{m}$ axes in terms of their maximum values: they are coincident, and higher than the maximum eigen value associated with the $\boldsymbol{e}$ axes. The R^2_{00} and R^2_{22} values track the order parameters as determined by the degree of ordering of the three tensors (section 2.4.1). The last plot in this figure shows the variation of k-index with temperature, which essentially indicates which ordering among the three axes, is providing the highest eigen value among all three tensors. Here the data plotted ($\times$ symbols) are the instantaneous values of k-index obtained at 200 instances, during the production run. It may be observed that for the case of zero field, with the equivalence of $\boldsymbol{e}_\perp$ and $\boldsymbol{m}$ axes (in terms of their maximum eigen values) in evidence, it is not surprising that there is really no well defined primary director in the sense of maximum eigen value direction. The k-index randomly fluctuates between 2 and 3 (discretely) depending on the two instantaneous maximum value between the two eigen values. This represents a dynamic equilibrium, reflecting the D_{4h} symmetry, at this point A2.

The subsequent plots in the Figure 5.6 depict progressively, variation in these properties with field. It may be seen that with the application of the field, (Figure 5.6(b) for $E_a = 0.1$), the $\boldsymbol{e}_\perp$ and $\boldsymbol{m}$ axes are no more equivalent in terms of their ordering, and k-index is tagged to $\boldsymbol{m}$ axes, at a lower temperature. As the field increases to 0.2 and beyond, the $\boldsymbol{m}$ axes are coupled to the field string

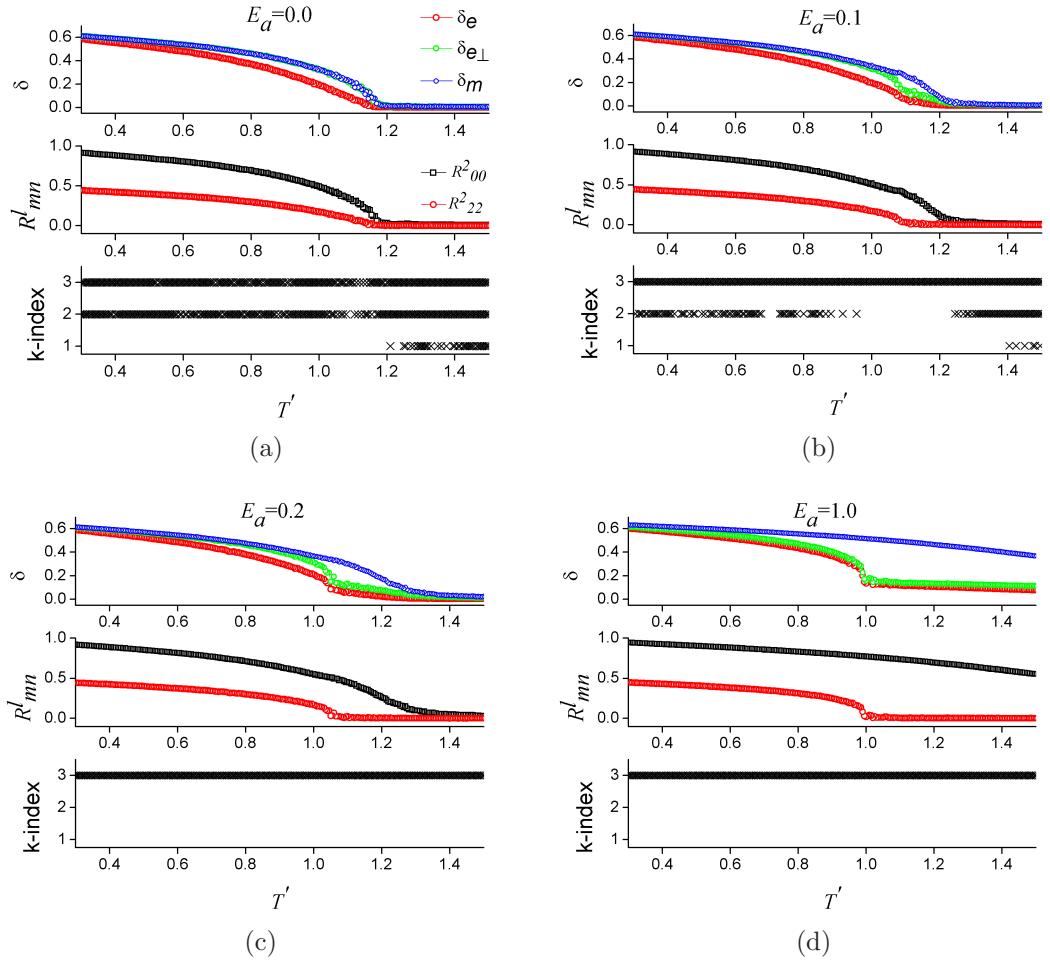

Figure 5.6: Temperature dependence of maximum eigen values of the ordering tensors ($\delta' s$), uniaxial and biaxial orders, and k-index (see text for more description), for the case A2, at various values of applied field.

enough, that k-index remains tagged to value 3 in the N_B phase. In contrast, the point C2 on the λ-axis corresponds to $\gamma = 0$, and is the uniaxial torque direction along the molecular $\boldsymbol{m}$ axes. Application of the external field coupling to the $\boldsymbol{m}$ axes themselves, thus do not lift this symmetry between $\boldsymbol{e}$ and $\boldsymbol{e}_\perp$ axes. This may be noted from the field dependent graph shown in Figure 5.7. Equally complementary is the observation of the variation of the k-index values. On the onset of transition to N_B phase, it gets tagged to the $\boldsymbol{m}$ axes, as the application of a field under above conditions, strengthens the order along that direction further. It is useful to note that the external field affects the molecular ordering qualitatively

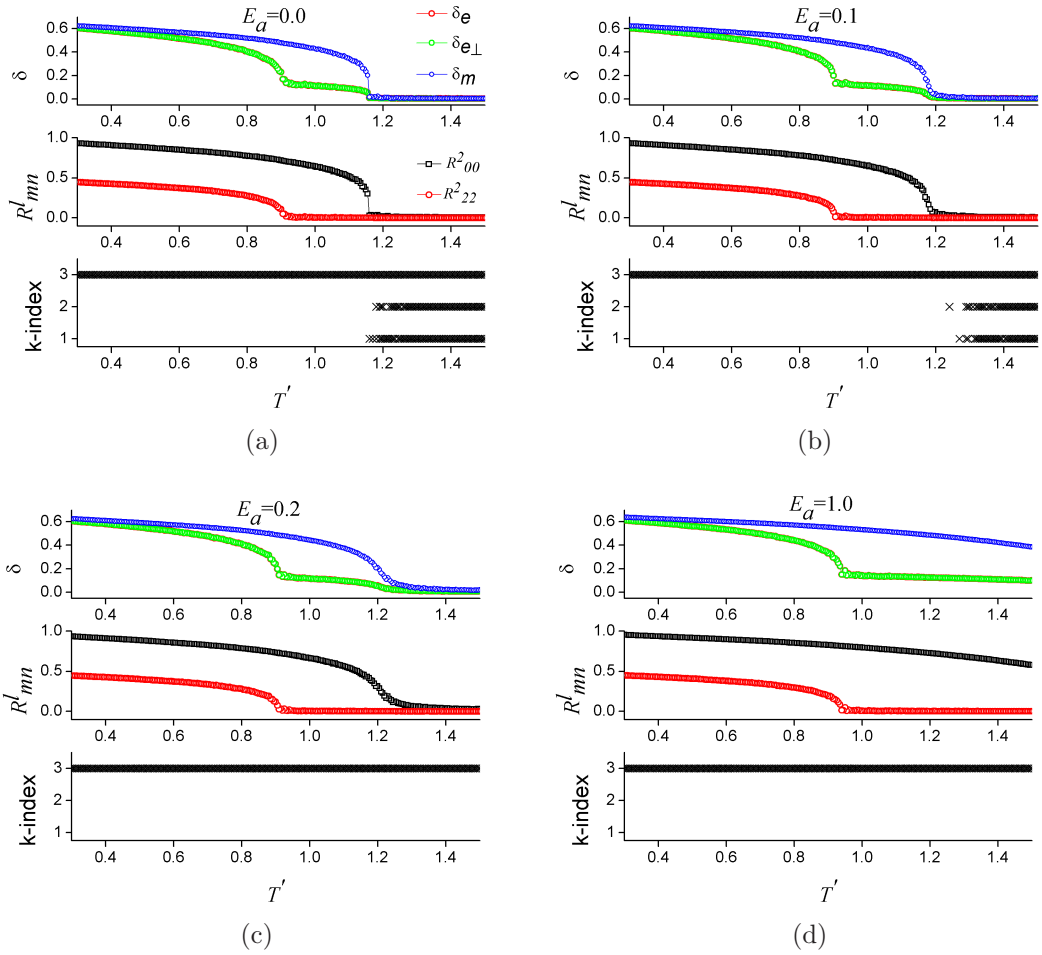

Figure 5.7: Temperature dependence of maximum eigen values of the ordering tensors (δs), uniaxial and biaxial orders, and k-index (see text for more description), for the case C2, at various values of applied field.

differently in these two cases.

We now focus on the dependence of transition temperatures of N_B transitions in C2 and A2 systems, in the back drop of the information we have on the evolution of the ordering tensors of the molecular axes (Figures 5.6 and 5.7). System C2, with $\gamma = 0$, is hosted on the λ-axis, and hence experiences uniaxial torque about the molecular $\boldsymbol{m}$ axis [41]. The pair-wise interaction between such D_{2h} molecules exhibit D_{4h} symmetry. (see δ_e and $\delta_{e_\perp}$ values in Figure 5.7, at different field values). The field coupling to this axis of symmetry (molecular $\boldsymbol{m}$ axes), and the transition is from the uniaxial to biaxial phase. The quenching of fluctuations associated

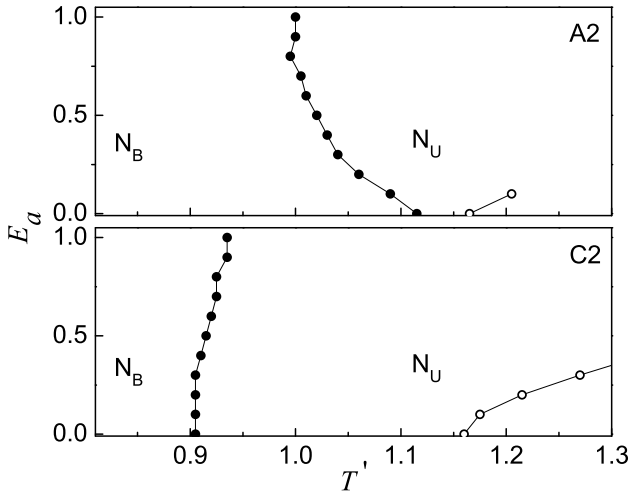

Figure 5.8: Field dependence on the transition temperatures T'_{PN} (open circles) and T'_{UB} (filled circles) for the cases A2 (top) and C2 (bottom) respectively.

with the primary director $\boldsymbol{n}_3 \equiv \boldsymbol{n}$ (of the ordering $\boldsymbol{m}$ axes) is already in effect before the onset of biaxial transition, in the uniaxial phase itself. The dependence of T'_{UB} with field is thus expected to arise primarily from the quenching of the secondary directors $\boldsymbol{n}_1$ and $\boldsymbol{n}_2$, associated with the ordering of the molecular $\boldsymbol{e}$ and $\boldsymbol{e}_\perp$ axes, and could be evident at the onset of the biaxial phase. It may also be noted that under the coupling of the field with the long axes $\boldsymbol{m}$ of the molecules, the quenching of the fluctuation of the two secondary directors could only be partial: only components of such fluctuations within the plane of the field and the respective director could be affected. Thus we could expect a somewhat subdued, but qualitatively similar, effect of the field on T'_{UB}. The observation presented in Figure 5.8 (bottom) indicate that the T'_{UB} of C2 system is in principle enhanced with field, relatively slowly initially,– in keeping with the similar behaviour as in the case of the primary director.

The symmetry of the system A2 is distinctly different, leading to a qualitative difference in the response to the applied field. It lies on a uniaxial torque axis [41], and has D_{4h} symmetry of the pair-wise interaction among D_{2h} molecules about that director. Therefore in the absence of a field, molecular $\boldsymbol{e}_\perp$ and $\boldsymbol{m}$ directors ($\boldsymbol{n}_2$ and $\boldsymbol{n}_3$) are equivalent in the ordering characteristics, as is evident from Figure 5.6. ($\delta_{e_\perp}$ and δ_m variation at $E_a = 0$). Application of the field however

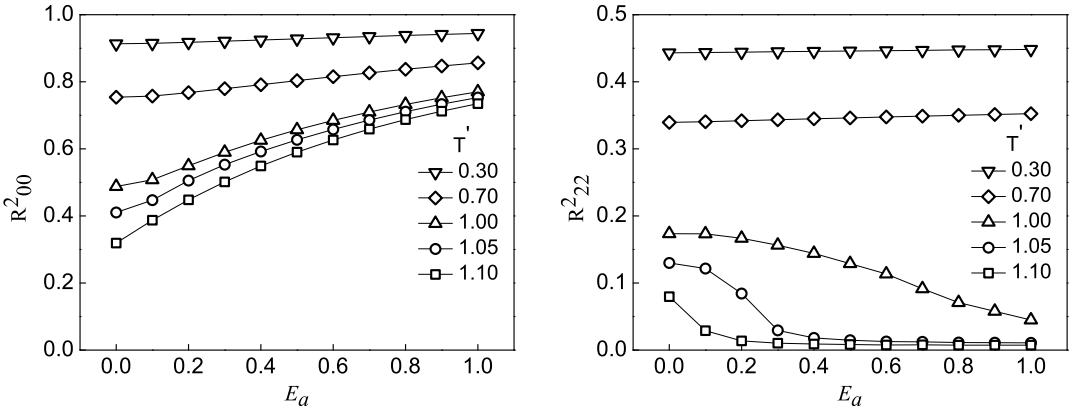

(a) (b)

Figure 5.9: Field dependence of (a) R^2_{00} and (b) R^2_{22} at various values of temperatures.

breaks this symmetry: the applied field promotes nematic order of the molecular $\boldsymbol{m}$ axes (long axes), and the equivalence of the two ordering tensors (of $\delta_{e_\perp}$ and $\boldsymbol{m}$ axes) no more exists. The progressive changes in the (maximum) eigen value associated with the ordering of the $\delta_{e_\perp}$ axes with field in Figure 5.6 are indicative of this. The uniaxial phase is thus progressively stabilized with increasing field, suppressing the onset of the biaxial phase, as is seen in Figure 5.8 (top). This seems to continue until, at some high enough field, the ordering tensors of the molecular minor axes ($\boldsymbol{e}$ and $\boldsymbol{e}_\perp$) are eventually equivalent. This corresponds to approximately $E_a \approx 0.8$. Beyond this field value, we conjecture that the effect of the field on the $\mathrm{N}_U\mathrm{N}_B$ transition mimics essentially the manifestations discussed for case C2. Essentially application of strong enough fields appears to have transferred the D_{4h} symmetry axes from $\boldsymbol{e}$ to $\boldsymbol{m}$ (A2 to C2), and the consequent temperature dependence of this transition is due to the partial quenching of the fluctuations of the secondary director due to the field.

In Figure 5.9, we show variation of the bulk order parameters R^2_{00} and R^2_{22} with the application of field at certain chosen temperatures, which were initially (at $E_a = 0$) in the biaxial phase. The effect of this field on R^2_{00} at all temperatures is a monotonic enhancement, as is to be expected with the field coupling with

the corresponding molecular axes. The variation of R^2_{22} with field at these temperatures is different. In the high temperature region, adjacent to the zero field $N_U N_B$ transition ($T' = 1.1$ to 1.0) the effect of the field is to suppress the biaxial order, thereby satisfying uniaxial symmetry against temperature decrements. The two temperatures, showing marginal increase of R^2_{22} with field ($T' = 0.3$ and 0.7) correspond to regimes of the field where the system is now like C2, and the partial suppression of the fluctuations of the secondary directors due to quenching could only lead to the enhancement of the corresponding (biaxial) order.

It may be pointed that the analysis based on Landau free energy of these systems alludes to the possibility that the slope of this transition temperature variation with field could vary all the way from positive to negative, depending on the choice of Landau coefficients. In this study we find, based on a microscopic model, that such qualitative changes in the slope are feasible, and are explained in terms of the symmetry of the system *vis-à-vis* the axis to which the applied field couples to. While this scenario is illustrative of the role of the choice of parameters of the Hamiltonian model, and perhaps throws some useful light on the mechanism, we envisage promising future work, covering the other representative model parameters which might mimic real systems, as well as biaxial systems with negative dielectric anisotropy. It is known that [17] even with simple uniaxial nematics, such an anisotropy leads to very curious possibilities.

Chapter 6

Colloidal nanoparticle trapped by nematic defect line

This chapter deals with the study of the interaction of a colloidal nanoparticle with a topological disclination line in a nematic medium. Curvature elasticity-mediated interactions in confined nematic liquid crystals (LCs) have turned out to be a powerful tool for colloidal particle assembly both in two- and three-dimensional systems [87, 241–243]. This mechanism is typically externally assisted by the use of laser tweezers allowing for a direct manipulation of colloidal particles in a refractive index-mismatched nematic medium [244, 245]. The resulting colloidal crystals show promise for use in various photonic applications [246]. A most relevant aspect in colloidal crystal assembly is the interaction of colloidal particles with nematic topological defect lines (disclinations): colloidal particles are known to be attracted towards disclinations if they are well within the influence of the corresponding distortion field [247–249]. Another important feature is the response of disclination-trapped particles to the application of an external force as provided in an experiment, e.g., through a laser tweezer in a disclination line tension measurement [244, 250]. Moreover, when a colloidal particle is moved, this affects the surrounding nematic medium, including the disclination lines [243, 251].

Here we present a simple microscopic lattice Monte Carlo (MC) simulation study of a small spherical colloidal nanoparticle trapped by a nematic disclination line, with a typical particle size around, or even below, 100 nm [252–254]. While there have been a number of experimental investigations in such systems, microscopic simulation studies are still rare. We focus on the particle force-displacement behaviour when an external (e.g., laser tweezer) force is applied in an attempt to move the particle. To provide a controlled disclination line environment, a nematic liquid crystal sample confined to a prismatic nanochannel is considered. Nanochannel-confined colloidal particles have been studied in the past using phenomenological simulations [255], while our approach here is microscopic and based

on simple pairwise interactions. Recently, off-lattice molecular simulations have also been used to study small nanoparticles in LCs, focusing on particle diffusivity and interaction, gel formation, and particle positioning inside LC droplets [256–258]. We perform lattice-based Monte Carlo simulations to study a confined liquid crystal system with a topological disclination line entangling a nanoparticle [259]. In our microscopic study the disclination line is stretched by moving the colloid, as in the laser tweezing experiments, which results in a restoring force attempting to minimize the disclination length. From constant-force simulations we extract the corresponding disclination line tension, estimated as ~ 50 pN, and observe its decrease with increasing temperature.

6.1 Model, geometry, and method

Our approach is based on the Lebwohl-Lasher (LL) lattice model [93, 94], where elongated liquid crystal molecules are represented by a system of freely rotating unit vectors (spins) $\boldsymbol{u}_i$ arranged into a simple cubic lattice of spacing a. The colloidal particle, as well as the confining nanochannel walls, are carved from the cubic lattice, with the corresponding interfacial spin orientations fixed according to the desired boundary conditions (anchoring). The total interaction energy is given by $E = -\epsilon \sum_{<ij>} \left[3(\boldsymbol{u}_i \cdot \boldsymbol{u}_j)^2 - 1\right]/2$, where the sum is taken over the nearest-neighbour lattice sites i and j, while $\epsilon > 0$ is the orientational interaction strength promoting parallel spin alignment. The nematic-nematic, nematic-colloidal particle and nematic-wall interaction strengths are assumed equal, which implies strong surface anchoring with an extrapolation length [1] approaching $\sim a$. Temperature T is represented in reduced units as $T^* = k_B T/\epsilon$, with bulk nematic-isotropic (NI) transition occurring at $T^*_{NI} \sim 1.1232$ [94].

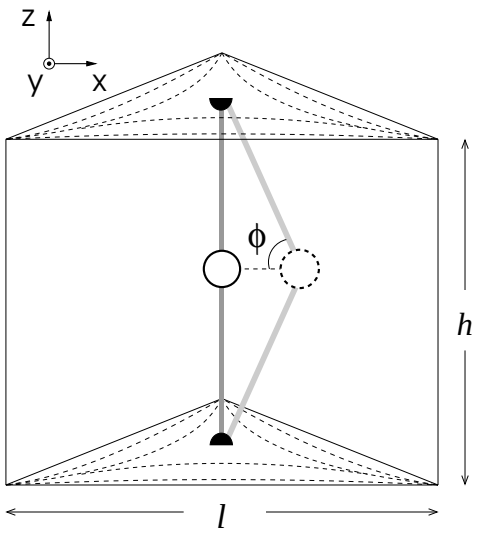

Figure 6.1: Schematic of the simulated nanochannel: dashed lines at the top and bottom surfaces represent the director field. The colloidal particle under study (white) is at the center and the smaller pinning particle (black) is at the channel top and bottom (note the periodic boundary conditions). The disclination (dark grey line) runs along the channel axis. The particle in a shifted position along with the stretched disclination is also shown in lighter shades. The defect structure around the particles is not explicitly shown.

The simulation box is simple cubic and periodic along the z-direction, accommodating a prismatic nanochannel. The channel is directed along z and has a length $h = 100a$; its lateral (xy) cross section is an equilateral triangle of side length $l = 200a$. This leaves more than 1.73×10^6 lattice sites inside the channel, actively taking part in the simulation and constituting the bulk of our nematic medium (see Figure 6.1). Bounding sites along the nanochannel surface are anchored planarly within the xy-plane so as to create a stable disclination line of strength $m = -1/2$, running along the channel symmetry axis, z. Through such boundary conditions we have explicitly avoided less stable integer-strength disclinations characterized by a higher free-energy cost per unit length, $F_d \propto m^2$, that, in addition, are also prone to escape along z [1, 260].

A spherical colloidal particle with strong homeotropic (normal) surface anchoring and $5a$ radius is fixed at the channel symmetry axis, serving to pin the edges

of the disclination. Another similar colloidal particle with $10a$ radius is initially placed at the mid-point of the nanochannel axis, *i.e.*, $h/2 = 50a$ away from the pinning particle (Figure 6.1). In our study, we focus on the interplay between the disclination line and this second colloidal particle (which is either kept fixed in position or could be mobile), taking its initial position (channel center) as the origin of our reference frame, $\boldsymbol{r}_c = (0, 0, 0)$, and denoting its instantaneous position (with respect to the MC "time") with $\boldsymbol{r}_c = a(x_c, y_c, z_c)$. Inclusion of the movable particle makes an otherwise straight disclination line loop around it, entangling it in the process. In this way a particle inclusion and a disclination are mutually affined, and hence the disclination can be stretched by pulling the particle away from the channel center. Excess pulling can cause the disclination to detach from the particle, and relax by retracing to its initial unstretched configuration. Figure 6.2(a) shows the cross section of the triangular nanochannel with a few layers in the xy plane near $z_c = 0$, obtained from a snapshot of the system at equilibrium at $T^* = 0.1$, with the colloidal particle fixed at $\boldsymbol{r}_c = (0, 0, 0)$. A magnified view near the colloidal particle is also shown in Figure 6.2(b) where the defect regions near the colloid are marked.

We explore the behaviour of our model system using Markov chain MC simulations. The underlying phase space consists of nematic spin orientations $\boldsymbol{u}_i$ and positions, as well as of the moving particle coordinates $\boldsymbol{r}_c$. In simulations where the particle is fixed, the MC evolution affects exclusively the nematic spin orientations and follows the standard Metropolis procedure [94, 120, 261]. Here single-spin reorientational trial moves are generated using the Barker-Watts technique [121] and are accepted with a probability $\min[1, \exp(-\Delta U/k_B T)]$, where ΔU is the corresponding interaction energy change. The acceptance ratio is kept close to 0.5 by dynamically adjusting the spin reorientation amplitude. A standard MC sweep is defined as an attempted reorientation of all nematic spins in the sample.

In simulations where the particle is mobile, on the other hand, composite particle moves are performed in addition: first, the particle is shifted randomly by a lattice unit and the nematic spins annihilated in this way are recreated in the newly established void on the other side of the particle. The recreated spins are given

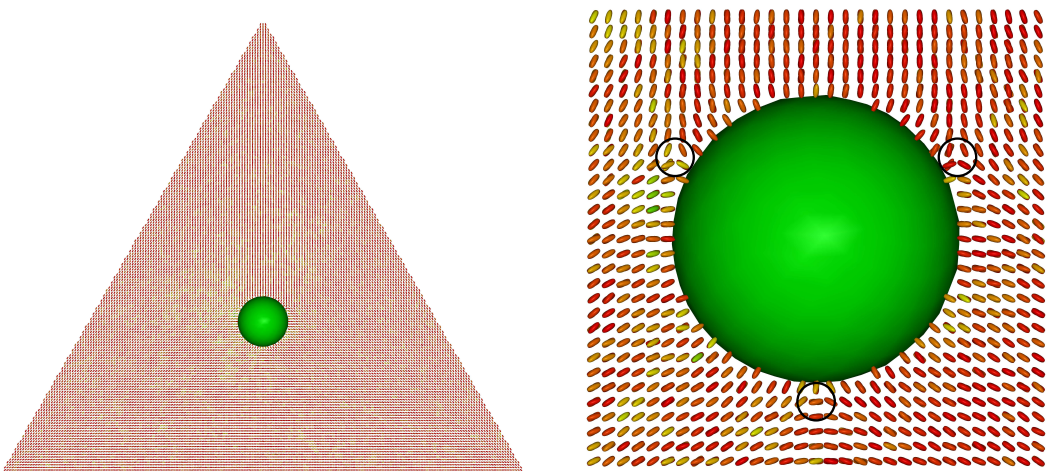

Figure 6.2: (a) Snapshot of the system from an equilibrium microstate at $T^* = 0.1$ showing the cross section of the triangular nanochannel with a few layers in the xy plane near $z_c = 0$. The colloidal particle with radius $10a$ shown in green is fixed at $\boldsymbol{r}_c = 0$. The LC spins are coloured blue to green to red as their orientations changes from a direction parallel to perpendicular with respect to the z direction. The predominant red colour of the bulk LC sites indicates their orientation being almost parallel to the xy plane. (b) A magnified view of the sites near the colloidal particle with the defect regions marked in black circles.

orientations compliant with the particle-imposed boundary conditions, which are refined by 1000 relaxation sweeps (see below) involving additional LC spins in the particle vicinity. The acceptance or otherwise of this composite particle move is, as above, guided by the Metropolis criterion, ΔU here denoting the total interaction energy difference between states before and after the attempted composite move. The relaxation sweeps performed prior to this acceptance/rejection are essential to facilitate the insertion of the displaced particle well equilibrated with respect to the existing nematic director field. They are carried out according to the Metropolis scheme used in fixed-particle runs, but involve, for the optimization of computational time and realize trial move acceptance ratios, only spins within a thin shell of $3a$ thickness surrounding the particle. (The immediate reorienting influence of the moving particle is expected to be stronger only in its vicinity.) After every such attempted composite move, additional 1000 standard MC sweeps are performed without moving the particle, to relax the entire director field, and this

sets a unit for the MC simulation "time" t_c. This algorithm is intended to reflect, and account for, the difference between the slower translational time scale associated with the larger and massive particle, compared to the faster reorientations of the LC spins constituting the surrounding nematic medium.

Note that, once the system has reached equilibrium and detailed balance is obeyed, the above Metropolis acceptance criterion generates the desired (canonical) distribution in phase space only if a given trial move and its reverse are attempted with equal probabilities [261]. While this is certainly the case for individual spin reorientations [121], it is much less obvious for our composite moves where the probability of attempting a particle displacement (together with a specific orientational configuration of the surrounding nematic spins) may, at least in principle, depend on the particle position. This arises due to the instinctual inadequacy of the procedure to sample the available phase space (for the geometry considered here) in a perfectly unbiased way. In the cases considered in this work, *i.e.*, for small particle displacements along the x-axis far enough from the confining walls, we expect this dependence to be negligible; therefore, forward and reverse move attempts should eventually be equally probable, and result in the canonical asymptotic distribution.

In analogy with the tweezing experiments wherein an adequately intense laser is used to pull the particle, in our simulations an external constant force $\boldsymbol{F}$ is applied. In such a case the Metropolis criterion for the acceptance probability of the particle move is modified to $\min\{1, \exp\left[-\Delta(U - \boldsymbol{F}\cdot\boldsymbol{r}_c)/k_BT\right]\}$ [261, 262]. In the following, external force is given in dimensionless units $F^* = |\boldsymbol{F}|a/\epsilon$. Taking $\epsilon \sim 0.023$ eV, which yields a bulk nematic-isotropic (NI) transition at room temperature [94], and $a \sim 1$ nm, which roughly assumes one spin to represent a single LC molecule [93, 98], a unit of F^* corresponds to ~ 3.7 pN.

To identify and visualize topological defects, Westin metrics [263] are calculated for each lattice site i from the eigenvalues $\lambda_1^i \geq \lambda_2^i \geq \lambda_3^i$ of the the averaged local ordering matrix $\langle \boldsymbol{u}_i \otimes \boldsymbol{u}_i \rangle$: $c_l^i = \lambda_1^i - \lambda_2^i$, $c_p^i = 2(\lambda_2^i - \lambda_3^i)$, and $c_s^i = 3\lambda_3^i$, with $0 \leq c_l^i, c_p^i, c_s^i \leq 1$. c_l^i, c_p^i, and c_s^i approaching ~ 1 correspond to prominent uniaxial, planar, and isotropic ordering, respectively. Since the defect core is characterized

by a depressed uniaxial order, compared to the rest of the medium, its structure can be visualized by constructing isosurfaces of c_l^i obtained from the $\boldsymbol{u}_i$ field, at an appropriately chosen (temperature-dependent) threshold. The averaging of the local ordering matrix is performed over the six nearest neighbour lattice sites, apart from the test site, from an instantaneous configuration or, alternatively, over a large number of MC sweeps. A so-called "instantaneous defect structure" (IDS) is obtained in the first case, and a "mean defect structure" (MDS) in the second. In our figures, IDS and MDS are typically shown for lower and higher values of T^*, respectively.

Along the length of simulation nanochannel, the nematic director field surrounding the disclination line is nearly identical except near the particle, and hence translations of the particle along the z-axis are energetically largely inconsequential. In our simulations we set $z_c = 0$, and translation moves of the particle are restricted along the x-axis, without loss of generality. This is to scale down the computational time to manageable limits, given the size of the three-dimensional sample space within the channel. The broad objective is to capture the essential qualitative behaviour of the system with multiple scales.

6.2 Equilibrium defect structures with fixed particle positions

Initially we look at the equilibrium defect structures in the system as a function of colloidal particle position, along the x-axis. The particle, initially positioned at the origin $x_c = 0$, is shifted off-center step-by-step to the adjacent sites, after equilibrating the medium with 2×10^5 MC sweeps during each step. Figure 6.3(a) shows the defect structure obtained by averaging the local ordering matrix over the latter 10^5 MC sweeps (production run) with particle at $x_c = 0$ and $T^* = 1.0$. Figures 6.3(b)-(f) show the IDS structure sequence obtained after each translational step at $T^* = 0.1$. It may be noted that during the equilibration sweeps in each of these steps, the particle position remains fixed. As the particle is shifted away

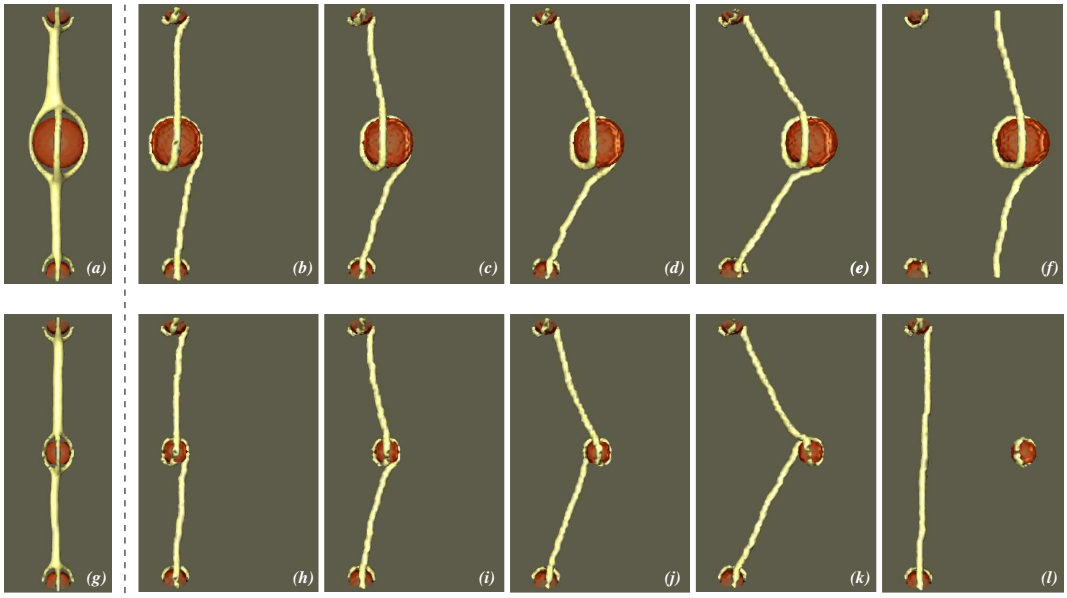

Figure 6.3: Top row shows defect structures (yellow) entangling a colloidal particle (red) of radius $10a$, obtained with (a) the particle positioned at the origin with $T^* = 1.0$, averaged over MC sweeps (MDS) and, (b)-(f) with $x_c = 0$, 10, 20, 30, and 40 with $T^* = 0.1$ from an equilibrated instantaneous configuration (IDS). Bottom row displays similar structures for a smaller particle of radius $5a$. Disclinations are visualized as c_l^i isosurfaces for threshold values of 0.85 and 0.28 at the lower and higher temperatures, respectively. (The corresponding bulk values are approximately 0.98 and 0.6.) Note the apparent variation in the looping of the disclination line around the colloid, and in the thickness of the line away from the particle, at both the temperatures. See the text for more details. The small particles seen at the top/bottom in each plate serve to pin the disclination line.

from center, the disclination line stretches itself, still entangling the particle, up to a threshold distance above which a detachment occurs. This threshold is observed at $x_c \sim 35$ for $T^* = 0.1$, and occurs at a smaller value of x_c at higher temperatures. For comparison, similar data for a smaller particle of radius $5a$ are shown in the bottom row of Figure 6.3. Figure 6.4 shows the mean defect structures obtained at $T^* = 1.0$ at different values of x_c. Here a second isosurface at a higher threshold of c_l^i is also superposed (please refer to the movies named Chapter6-instantaneous-low-temp.wmv and Chapter6-average-high-temp.wmv included in the soft copy, for further elucidation of this point).

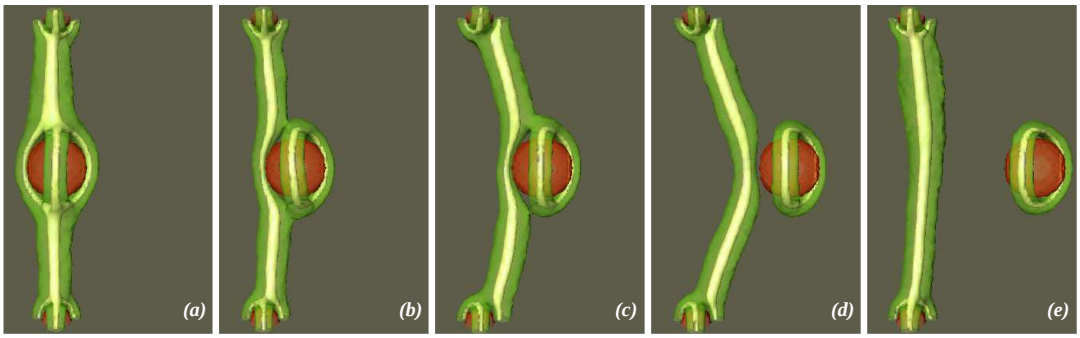

Figure 6.4: (a)-(e) Mean defect structures of the system at $T^* = 1.0$, with the position of the particle (red), $x_c = 0$, 10, 20, 30, and 40. Isosurfaces are drawn at $c_l^i = 0.28$ (yellow) and 0.53 (green).

At $T^* = 1.0$ the defect structure appears to have a threefold symmetry wherein it forks into three branches around the particle and then rejoins to form a single disclination. In the present lattice simulations, this structure apparently gets modified as the temperature is lowered. This can be attributed to a reduced defect line bending near the particle in accordance with larger line tensions under these conditions. Note that sometimes transformations between different entangling structures occur also during the course of simulations at fixed external parameter values [for instance, see the difference between the entangling of the displaced colloid by the disclination line in Figures 6.3 (i) and (j)]. It is seen that when the large ($10a$ radius) moving particle is considered, it is the disclination that detaches from the pinning particle, on shifting the particle far away from the center. For the small ($5a$ radius) particle, the opposite is true: the disclination detaches from the moving particle instead, relaxing back to the center, while leaving the moving particle with a Saturn ring defect [90]. This seems to be due to a more pronounced anchoring effect by the larger particle at this temperature. Another effect of temperature is on the fluctuations of the disclination line itself. A manifestation of its spatial fluctuations over the MC "time" is seen as an increase in the disclination line thickness in regions far away from the particles as in Figures 6.3(a) and (g), at $T^* = 1.0$. Figure 6.4 shows the mean defect structures obtained at $T^* = 1.0$ at different values of x_c. Here a superimposed second isosurface at a higher threshold

of $c_l^i = 0.53$ enveloping the one with a lower c_l^i, alludes to the fact that the defect structures formed for different system parameters in our simulations are all qualitatively similar.

6.3 Unstretching of disclination line with mobile particle

Now we extend our simulations by allowing colloidal particle translation as the system evolves during MC "time", t_c, in order to explore the ability of a stretched disclination to move an entangled particle. In this case we take an initial configuration of the system where the particle is at $x_c > 0$, entangled by a stretched disclination. In an experiment this is achieved by pulling the disclination affined either to an isotropic laser-created region, or to a particle tweezed by a laser, and then withdrawing the laser intensity. This corresponds to a state similar to that depicted in Figure 6.3(d) where the particle is at $x_c = 20$ units away from the origin. The trail of the moving particle is monitored over t_c and is shown in Figure 6.5. In all cases the particle is found to be drawn, approximately, back to the origin at $x_c \sim 0$, adducing the presence of a restoring force which drives the relaxation of the disclination to its equilibrium. This indeed should be expected, since a shorter disclination corresponds to lesser volume occupied by the defect region, thereby reducing the total free energy. Note that in some cases the equilibrated particle position is slightly off-centered, with typically slightly negative equilibrium x_c values; this is understood as due to the asymmetric particle entanglement (see Figure 6.3). Note also that very large fluctuations in the particle position occur at higher temperatures, and so most of our simulations are performed at relatively low T^* to facilitate the analysis.

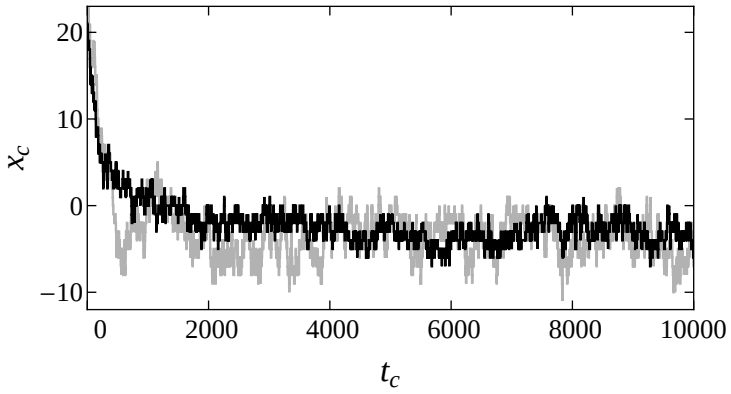

Figure 6.5: Trail of the particle as the system evolves from an initially stretched entangled disclination with particle at $x_c = 20$, along x at $T^* = 0.1$ (black) and 0.15 (grey).

6.4 Constant-force simulations with mobile particle

Finally, we perform constant-force simulations wherein a constant force F^* is applied on the particle, initially positioned at the origin. The force is applied along the positive x-axis and, for simplicity, the particle motion is also restricted along the same axis. Initially, the force shifts the particle away from the origin and after a transient time this distance is seen to equilibrate over a mean value, when the system assumes a nearly steady state. This occurs when the restoring force, manifested through the disclination line tension, balances with the external force F^*. Larger F^* values result in an equilibration farther from the origin. Beyond a threshold value of the force, a detachment occurs. It is ensured that such simulations are discarded, by monitoring the defect structures at regular intervals as the simulation proceeds. We observe in all the cases that the particle position x_c equilibrates within first $2000t_c$; then, its average is determined over the next $8000t_c$. These simulations are carried out at various temperatures. Figure 6.6 shows the trail of the particle for various values of F^* at $T^* = 0.1$. Here also the

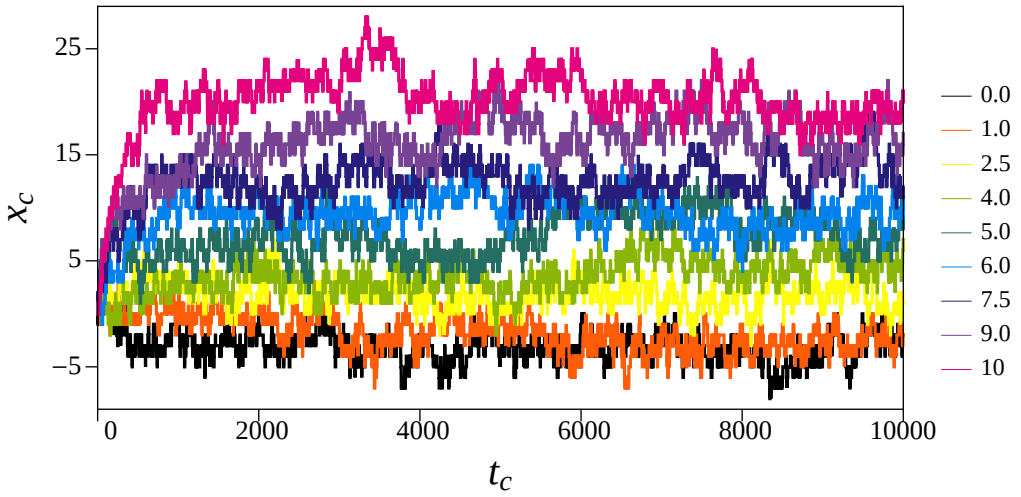

Figure 6.6: Trail of the particle as the system evolves from an initial equilibrated configuration with the colloidal particle placed at $x_c = 0$, for various values of the constant force, F^* at $T^* = 0.1$.

slightly off-centered positions of the particle is seen even at zero value of force due to the asymmetric particle entanglement at this temperature, as indicated earlier.

The dependence of the average equilibrated distance $\langle x_c \rangle$ on the applied force F^* at different temperatures is shown in Figure 6.7(a). The reasonably good linear fits (with Pearson's correlation coefficients ≥ 0.95) suggest Hookean behaviour, permitting the comparison of disclination with an elastic string. (Again, at zero force, slightly negative $\langle x_c \rangle$ are observed, consistent with our above reasoning.) Slopes obtained from the fits are inverse values of Hookean force constants, k^*, with their temperature dependence shown in Figure 6.7(b). These values translate to real units as $\epsilon k^*/a^2$ and are, for the a and ϵ estimates given in section. 6.1, in the range of $\sim 1.5 \times 10^{-3}$ N/m. In the temperature range considered here, typical line tension values just before detachment at $x_c \sim 20$ ($\tan\phi = h/2x_c \sim 2.5$, see Figure 6.1) and $F^* \sim 10$ are estimated as $F_d = F^*\epsilon/2a\cos\phi \sim 50$ pN, which agrees well with experiments yielding values between 20 and 120 pN [244, 250, 264]. Note that this estimate of F_d is sensitive to the choice of the lattice spacing parameter value, a. (Sometimes, a nematic spin in the LL model is taken to represent a close-packed cluster of up to $\sim 10^2$ molecules rather than a single molecule [113],

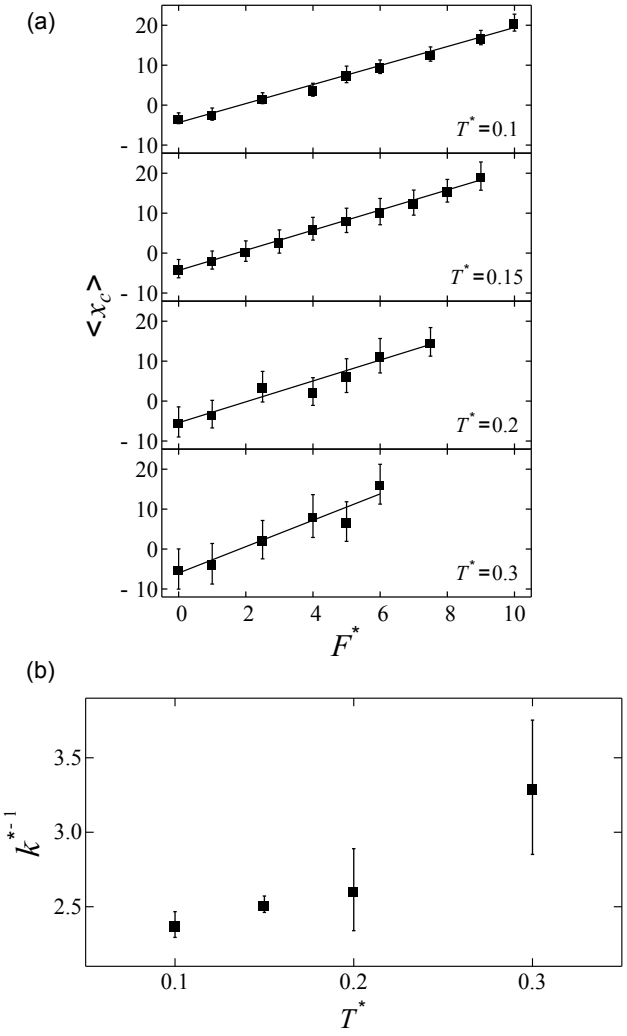

Figure 6.7: (a) Equilibrium colloidal particle position versus applied force for different temperatures. Straight lines represent Hookean linear fits. (b) Temperature dependence of the force constant inverse $1/k^*$.

yielding a somewhat larger a and, in turn, a smaller F_d.) Moreover, like in experiments [264], our data displayed in Figure 6.7(b) suggest a decrease of the line tension with increasing temperature. This also agrees with the phenomenological prediction $F_d \propto K$, where K, the Frank elastic constant of the nematic LC in one-constant approximation, decreases with increasing temperature [1, 260]. Finally, F_d is a liquid-crystalline material property and should be independent from

the specific geometrical setup of our simulated experiment, *i.e.*, nanochannel size parameters h and l, as well as the external force pulling direction.

In summary, a simple microscopic spin model is employed to study a nematic liquid-crystalline system containing a spherical particle entangled by a disclination line, using lattice-based Monte Carlo simulations. The conventional single-spin-flip Markov Chain Monte Carlo procedure is adapted to incorporate the multiscales entering into the problem via the relatively slow translational motion of a larger particle in equilibrium with the surrounding liquid-crystalline medium. It is seen that our simulations qualitatively capture the physical behaviour of a real system, including an estimate for the disclination line tension in the range of ~ 50 pN and its decrease with increasing temperature. Simulation methods adopted here enable a study of a reasonably large system, allowing for an examination of the detailed nanoscale behaviour. Currently, this would have been less practicable using an off-lattice model, coarse-grained or atomistic, for reasons of unacceptable computational cost. On the other hand, continuum-based phenomenological approaches have their own constraints in the lower limit of the length scales that they need to probe into.

Chapter 7

Conclusions

In this chapter we recapitulate the generic conclusions drawn from the simulational studies on different liquid crystal (LC) systems reported in this thesis, and speculate on the potential pathways of future research. The underlying protocol for these computations is the Markov chain Monte Carlo (MC) dynamics implemented to achieve a specific stationary state in the configurational space, identified as per the chosen constraining (experimental) conditions. All the models employed are lattice-based, benefiting from the circumstance that these investigations are primarily concerned with changes in the orientational properties of the liquid crystal medium, under the application of a set of suitable control parameters, encompassing temperature, external fields, and substrate anchoring conditions. These studies, besides exploring the phenomena characteristic of the system under consideration, also propose certain MC strategies to tackle potentially interesting new problems.

The work on simple planar films of a uniaxial nematic medium with strong anchoring influence requiring the molecules to be normal to the surfaces, has led to the detection of a relatively rare director structure (film B) (at low enough temperatures) which deviates from the trivial arrangement (film A) of all molecules being compatibly normal to the surface. Director structures hosted by film B turned out to be topologically different from those of film A, and these two configurational spaces have been found to be disjoint from the point of view of Markov chain MC dynamics (till moderately high temperatures in the nematic phase), - satisfyingly. This investigation prompted the development of a protocol for the random walk of the system, similar to entropic sampling, but along the order parameter coordinate, while keeping the energy of the system essentially constant (OP-sampling). The exploration of compatible microstates (through their director structures) of these two films with OP-sampling has provided an insight into the very interesting organisation of these films, conforming to the requirements of conservation of respective topological symmetry on one hand, and on the other compliance of

bounds imposed on the (low) energy values while algorithmically guided to access very low ordered states.

A systematic access provided by this new sampling procedure (to such rare states corresponding to structures far away from equilibrium structures), prompted its application to bulk systems, with both uniaxial and biaxial symmetry. Uniaxial bulk samples (Lebwohl-Lasher model) equilibrated at different temperatures in the nematic phase were subjected to OP-sampling procedure, yielding a spectrum of microstates spanning upto a low bulk order value of ~ 0.1. We find that, as the allowed energies of the system is kept lower (corresponding to a higher order equilibrium state reminiscent of low temperature), the system has to develop very curious structures hosting macroscopic periodicity in order to be compatible with the simultaneous requirement of very low energy and very low order. Such structures become more evident as the OP-sampling is carried out at progressively lower (fixed) energies. Biaxial nematic phases facilitated, somewhat unexpectedly, a very illustrative random walk of an equilibrated biaxial system (prolate) in the two dimensional space of its dominant order parameters. An analysis of the symmetries of these transient states showed that the system, under the algorithmic pressure to execute a uniform random walk along uniaxial order parameter axis, visits a rich variety of transient (very rare) nematic states. The availability of these structures through this procedure perhaps could be a handy tool to generate deeply quenched states by design from a high temperature (low ordered) phase, to carry out kinematic studies.

Effect of an external field on the phase transition phenomena in LC systems is rather subtle; it introduces an additional length scale (field coherence length), and contributions to the free energy arising from different (Fourier) modes are governed by the bounding limits on the wave vector values. Thus, though the dependence of the interaction energy of the medium with the field is quadratic, leading to a predictable quadratic field-dependence of the transition temperature, delicate experiments in uniaxial nematics showed that the shift in the transition temperatures is initially linear with the applied field, crossing over to a quadratic regime only at higher fields. An intuitively appealing argument is forwarded based

on continuum model of the medium: the applied field, in conjunction with the curvature elasticity of the medium introduces a mesoscopic length scale limiting the upper cut-off wave lengths of the fluctuation modes of the director. The resulting quenching of these degrees of freedom reduces the entropy of the system linearly with field, manifesting in the experimental observations reported. In this context, the present work examined the efficacy of the microscopic models (based on nearest neighbour interactions) in predicting the experimental observations: its such application, if proved successful, would rather dramatically demonstrate the capability of a toy model to measure unto an experimental result, thought to be a consequence of the manifestation of a mesoscopic length scale. In order to measure very small shifts in the transition temperatures (one part in about 10^4) in the linear regime of the field, the simulations have to be geared to achieve such resolutions with acceptable statistics. The first study on uniaxial nematics strives to achieve this through the construction of canonical ensembles by reweighing procedures on entropic (energy uniform) ensemble of microstates. We report that the MC simulations on a microscopic model (Lebwohl-Lasher interaction) yield an initial linear field-dependence of the isotropic-to-nematic (IN) transition temperature, consistent with the recent experiments.

The second study in this direction is to examine the effect of an external field on a biaxial nematic system, with focus on the changes in the uniaxial-to-biaxial transition temperature on cooling. The motivation comes from the prediction from the Landau theory that the slope of the variation of this transition temperature with field could be either positive or negative (including zero), depending on the choice of the free-energy model parameters, the implication (in view of the above explanation in uniaxial nematics) being that quenching of director fluctuations need not be the only mechanism in these systems. We chose two systems with different coordinates in the Hamiltonian parameter space, hosting biaxial media with different symmetries: for system C2 the long axis of the molecule is the symmetry axis while for the second system A2 one of the minor axes is the symmetric axis. In both the cases the field is coupled to the long axis of the molecule. Under the circumstances, the field, besides quenching the different director modes (of the biaxial system), breaks the symmetry of the A2 system, while it still preserves the

symmetry of C2 system. Our results show that application of the field along the symmetry axis leads to a marginal enhancement of the transition temperature, - manifestation of the quenching of the modes of the secondary directors. The effect of the field when it breaks the inherent symmetry of the Hamiltonian seems to be qualitatively different. It corresponds in A2 system, to a preferential alignment of the long axes aided by the field, and this leads to relative stabilisation of the uniaxial phase, delaying the onset of the biaxial symmetry. Thus there is a suppression of this transition temperature in the initial stages. At sufficiently high fields this trend reverses signalling a change into the regime of quenching of the directors. This work thus presents a microscopic basis for the mean-field prediction of a non-universal variation of this transition temperature with the applied field. We feel that, since the biaxial phase diagram (with two parameters controlling competing interactions) is known to be complex and somewhat intriguing, further exploration with an external field, with both positive and negative dielectric anisotropies, would be helpful in appreciating the relative roles of these microscopic interactions. Another area of future investigation could be the application of entropic sampling methods in the presence of external fields, in view of the fact that in certain regions of the model parameter space this sampling procedure points to mesoscopic inhomogeneities, leading to qualitatively different phase diagrams.

The last application of the MC technique is concerned with the presence of multiple length scales in a confined nematic medium hosting a disclination line and a spherical colloidal particle entangled to it. Such systems form a building block of a nematic colloidal crystal. Treating this system at continuum level poses difficulties in dealing with lower length scales. Similarly simulations of the same with more realistic continuous models, like Gay-Berne interaction, would be prohibitive from computational point in view of the large number of particles involved (typically $\sim 2 \times 10^6$). In this context we attempted to explore this system with a simple lattice model and employ a single-spin flip protocol for implementing the Markov chain dynamics. The length-scale, and hence time-scale, separation of the dynamics of the colloidal particle from the faster relaxing LC medium requires certain

improvisations. We essentially split the composite system walk in the direct product space of the translational coordinates of the colloidal and the orientational space of the LC molecules. The implementation of this strategy to locally equilibrate the LC medium in the immediate neighbourhood of the colloidal particle before attempting its random walk, could be effected successfully, though this still required extensive computation over prolonged periods of time, engaging a cluster of machines in the parallel mode. We could make contact with real experiments by simulating constant-force experiments in order to extract disclination line tension and its temperature dependence. We envisage future improvements in this methodology, particularly in implementing the local equilibration protocol, so as to enable this simulation to mimic topical laser-tweezing experiments in the laboratories.

In summary, this thesis embodies the results of modest attempts to apply Markov chain Monte Carlo sampling techniques, and its improvised variants, in order to investigate a variety of physical phenomena in both confined and bulk LC systems.

References

[1] P. G. de Gennes and J. Prost, *The Physics of Liquid Crystals*, Oxford science publications (Clarendon Press, 1993).

[2] G. Vertogen and W. H. de Jeu, *Thermotropic liquid crystals, fundamentals* (Springer, 1988).

[3] A. Jákli and A. Saupe, *One-and two-dimensional fluids: Properties of smectic, lamellar and columnar liquid crystals* (CRC Press, 2010).

[4] P. Poulin, H. Stark, T. C. Lubensky, and D. A. Weitz, Science **275**, 1770 (1997).

[5] G. R. Luckhurst, Thin Solid Films **393**, 40 (2001).

[6] R. Berardi, L. Muccioli, and C. Zannoni, J. Chem. Phys. **128**, 024905 (2008).

[7] W. Guo and B. Fung, J. Chem. Phys. **95**, 3917 (1991).

[8] F. Biscarini, C. Chiccoli, P. Pasini, F. Semeria, and C. Zannoni, Phys. Rev. Lett. **75**, 1803 (1995).

[9] F. Bisi, G. R. Luckhurst, and E. G. Virga, Phys. Rev. E **78**, 021710 (2008).

[10] G. R. Luckhurst, S. Naemura, T. J. Sluckin, T. B. T. To, and S. Turzi, Phys. Rev. E **84**, 011704 (2011).

[11] G. R. Luckhurst and C. A. Veracini, *The Molecular Dynamics of Liquid Crystals*, vol. 431 of NATO Advanced Study Institute, Series C (Kluwer Academic Publishers, 1994).

[12] W. S. Park, J. Korean Phys. Soc. **37**, 331 (2000).

[13] J. Thoen, in *Phase Transitions in Liquid Crystals*, edited by S. Martellucci and A. N. Chester (Plenum Pub Corp, New York, 1992), NATO Advanced Study Institute, Series B: Physics, pp. 155–174.

[14] H. J. Coles, Mol. Cryst. Liq. Cryst. **49**, 67 (1978).

[15] E. F. Gramsbergen, L. Longa, and W. H. de Jeu, Phys. Rep. **135**, 195 (1986).

[16] D. Allender and L. Longa, Phys. Rev. E **78**, 011704 (2008).

[17] K. Trojanowski, D. Allender, L. Longa, and Ł. Kuśmierz, Mol. Cryst. Liq. Cryst. **540**, 59 (2011).

[18] G. De Matteis, A. M. Sonnet, and E. G. Virga, Continuum Mech. Thermodyn. **20**, 347 (2008).

[19] T. B. T. To, T. J. Sluckin, and G. R. Luckhurst, Phys. Rev. E **88**, 062506 (2013).

[20] W. Maier and A. Saupe, Z. Naturforsch. Teil A **13**, 564 (1958).

[21] M. J. Freiser, Phys. Rev. Lett. **24**, 1041 (1970).

[22] M. J. Freiser, Mol. Cryst. Liq. Cryst. **14**, 165 (1971).

[23] C.-S. Shih and R. Alben, J. Chem. Phys. **57**, 3055 (1972).

[24] R. Alben, Phys. Rev. Lett. **30**, 778 (1973).

[25] R. Alben, J. Chem. Phys. **59**, 4299 (1973).

[26] R. Alben, J. R. McColl, and C. S. Shih, Solid State Commun. **11**, 1081 (1972).

[27] J. C. Rowell, W. D. Phillips, L. R. Melby, and M. Panar, J. Chem. Phys. **43**, 3442 (1965).

[28] J. P. Straley, Phys. Rev. A **10**, 1881 (1974).

[29] G. R. Luckhurst, C. Zannoni, P. L. Nordio, and U. Segre, Mol. Phys. **30**, 1345 (1975).

[30] G. R. Luckhurst and S. Romano, Mol. Phys. **40**, 129 (1980).

[31] R. Hashim, G. R. Luckhurst, and S. Romano, Mol. phys. **56**, 1217 (1985).

[32] R. Hashim, G. R. Luckhurst, F. Prata, and S. Romano, Liq. Cryst. **15**, 283 (1993).

[33] C. D. Mukherjee and N. Chatterjee, Phys. Lett. A **189**, 86 (1994).

[34] C. Chiccoli, P. Pasini, F. Semeria, and C. Zannoni, Int. J. Mod. Phys. C **10**, 469 (1999).

[35] A. M. Sonnet, E. G. Virga, and G. E. Durand, Phys. Rev. E **67**, 061701 (2003).

[36] L. Longa, P. Grzybowski, S. Romano, and E. Virga, Phys. Rev. E **71**, 051714 (2005).

[37] G. De Matteis and E. G. Virga, Phys. Rev. E **71**, 061703 (2005).

[38] G. De Matteis, S. Romano, and E. G. Virga, Phys. Rev. E **72**, 041706 (2005).

[39] F. Bisi, E. G. Virga, E. C. Gartland Jr, G. De Matteis, A. M. Sonnet, and G. E. Durand, Phys. Rev. E **73**, 051709 (2006).

[40] F. Bisi, S. Romano, and E. G. Virga, Phys. Rev. E **75**, 041705 (2007).

[41] G. De Matteis, F. Bisi, and E. G. Virga, Continuum Mech. Thermodyn. **19**, 1 (2007).

[42] S. Romano, Physica A **337**, 505 (2004).

[43] S. Romano, Phys. Lett. A **333**, 110 (2004).

[44] S. Romano, Physica A **339**, 511 (2004).

[45] C. Zannoni, J. Mat. Chem. **11**, 2637 (2001).

[46] R. Berardi, L. Muccioli, S. Orlandi, M. Ricci, and C. Zannoni, J. Phys. : Cond. Matt. **20**, 463101 (2008).

[47] R. Berardi, J. S. Lintuvuori, M. R. Wilson, and C. Zannoni, J. Chem. Phys. **135**, 134119 (2011).

[48] L. Querciagrossa, M. Ricci, R. Berardi, and C. Zannoni, Phys. Chem. Chem. Phys. **15**, 19065 (2013).

[49] S. Belli, A. Patti, M. Dijkstra, and R. Van Roij, Phys. Rev. Lett. **107**, 148303 (2011).

[50] S. D. Peroukidis and A. G. Vanakaras, Soft Matter **9**, 7419 (2013).

[51] P. Teixeira, A. Masters, and B. Mulder, Mol. Cryst. Liq. Cryst. **323**, 167 (1998).

[52] S. D. Peroukidis, A. G. Vanakaras, and D. J. Photinos, Phys. Rev. E **84**, 010702 (2011).

[53] M. A. Bates and G. R. Luckhurst, Phys. Rev. E **72**, 051702 (2005).

[54] B. K. Latha, R. Jose, K. P. N. Murthy, and V. S. S. Sastry, Phys. Rev. E **89**, 050501(R) (2014).

[55] L. Yu and A. Saupe, Phys. Rev. Lett. **45**, 1000 (1980).

[56] F. Hessel and H. Finkelmann, Polymer Bulletin **15**, 349 (1986).

[57] K. Severing and K. Saalwächter, Phys. Rev. Lett. **92**, 125501 (2004).

[58] L. A. Madsen, T. J. Dingemans, M. Nakata, and E. T. Samulski, Phys. Rev. Lett. **92**, 145505 (2004).

[59] B. R. Acharya, A. Primak, and S. Kumar, Phys. Rev. Lett. **92**, 145506 (2004).

[60] S. J. Picken, T. J. Dingemans, L. A. Madsen, O. Francescangeli, and E. T. Samulski, Liq. Cryst. **39**, 19 (2012).

[61] K. Merkel, A. Kocot, J. Vij, R. Korlacki, G. Mehl, and T. Meyer, Phys. Rev. Lett. **93**, 237801 (2004).

[62] J. L. Figueirinhas, C. Cruz, D. Filip, G. Feio, A. C. Ribeiro, Y. Frere, T. Meyer, and G. H. Mehl, Phys. Rev. Lett. **94**, 107802 (2005).

[63] S. Polineni, J. L. Figueirinhas, C. Cruz, D. A. Wilson, and G. H. Mehl, J. Chem. Phys. **138**, 124904 (2013).

[64] T. Ostapenko, C. Zhang, S. N. Sprunt, A. Jákli, and J. T. Gleeson, Phys. Rev. E **84**, 021705 (2011).

[65] C. Oseen, Trans. Faraday Soc. **29**, 883 (1933).

[66] H. Zocher, Trans. Faraday Soc. **29**, 945 (1933).

[67] F. C. Frank, Discuss. Faraday Soc. **25**, 19 (1958).

[68] P. P. Karat and N. V. Madhusudana, Mol. Cryst. Liq. Cryst. **40**, 239 (1977).

[69] J. Nehring and A. Saupe, J. Chem. Phys. **54**, 337 (1971).

[70] H. Yokoyama, Mol. Cryst. Liq. Cryst. **165**, 265 (1988).

[71] M. Nobili and G. Durand, Phys. Rev. A **46**, R6174 (1992).

[72] A. Rapini and M. Papoular, J. de Physique **30**, C4 (1969).

[73] P. G. Cummins, D. A. Dunmur, and D. A. Laidler, Mol. Cryst. Liq. Cryst. **30**, 109 (1975).

[74] W. Helfrich, Phys. Rev. Lett. **24**, 201 (1970).

[75] I. Lelidis and G. Durand, Phys. Rev. E **48**, 3822 (1993).

[76] A. J. Nicastro and P. H. Keyes, Phys. Rev. A **30**, 3156 (1984).

[77] S. Dhara and N. V. Madhusudana, Europhys. Lett. **67**, 411 (2004).

[78] C. Rosenblatt, Phys. Rev. A **24**, 2236 (1981).

[79] T. Ostapenko, D. Wiant, S. N. Sprunt, A. Jákli, and J. T. Gleeson, Phys. Rev. Lett. **101**, 247801 (2008).

[80] F. Vita, I. Placentino, E. Samulski, and O. Francescangeli, Mol. Cryst. Liq. Cryst. **573**, 46 (2013).

[81] A. G. Vanakaras and D. J. Photinos, J. Chem. Phys. **128**, 154512 (2008).

[82] N. D. Mermin, Rev. Mod. Phys. **51**, 591 (1979).

[83] M. V. Kurik and O. Lavrentovich, Sov. Phys. Usp. **31**, 196 (1988).

[84] I. Chuang, R. Durrer, N. Turok, and B. Yurke, Science **251**, 1336 (1991).

[85] M. Kléman, *Points, Lines and Walls in: Liquid Crystals, Magnetic Systems and Various Disordered Media* (Wiley, New York, 1983).

[86] I. Muševič, M. Škarabot, U. Tkalec, M. Ravnik, and S. Žumer, Science **313**, 954 (2006).

[87] A. Nych, U. Ognysta, M. Škarabot, M. Ravnik, S. Žumer, and I. Muševič, Nat. commun. **4**, 1489 (2013).

[88] C. M. Spillmann, J. Naciri, W. R. Algar, I. L. Medintz, and J. B. Delehanty, ACS Nano **8**, 6986 (2014).

[89] T. Lubensky, D. Pettey, N. Currier, and H. Stark, Phys. Rev. E **57**, 610 (1998).

[90] E. Terentjev, Phys. Rev. E **51**, 1330 (1995).

[91] S. Ramaswamy, R. Nityananda, V. Raghunathan, and J. Prost, Mol. Cryst. Liq. Cryst. **288**, 175 (1996).

[92] G. Lasher, Phys. Rev. A **5**, 1350 (1972).

[93] P. A. Lebwohl and G. Lasher, Phys. Rev. A **6**, 426 (1972).

[94] U. Fabbri and C. Zannoni, Mol. Phys. **58**, 763 (1986).

[95] G. R. Luckhurst and P. Simpson, Mol. Phys. **47**, 251 (1982).

[96] D. J. Cleaver and M. P. Allen, Phys. Rev. A **43**, 1918 (1991).

[97] Z. Zhang, O. G. Mouritsen, and M. J. Zuckermann, Phys. Rev. Lett. **69**, 2803 (1992).

[98] C. W. Greeff and M. A. Lee, Phys. Rev. E **49**, 3225 (1994).

[99] Z. Zhang, M. J. Zuckermann, and O. G. Mouritsen, Mol. Phys. **80**, 1195 (1993).

[100] D. J. Cleaver and M. P. Allen, Mol. Phys. **80**, 253 (1993).

[101] C. Chiccoli, S. Guzzetti, P. Pasini, and C. Zannoni, Mol. Cryst. Liq. Cryst. **360**, 119 (2001).

[102] D. Andrienko, M. P. Allen, G. Skačej, and S. Žumer, Phys. Rev. E **65**, 041702 (2002).

[103] D. Jayasri, V. S. S. Sastry, and K. P. N. Murthy, Phys. Rev. E **72**, 036702 (2005).

[104] G. Skačej and C. Zannoni, Phys. Rev. Lett. **100**, 197802 (2008).

[105] T. Gruhn and S. Hess, Z. Naturforsch. A **51**, 1 (1996).

[106] S. Romano, Int. J. Mod. Phys. B **12**, 2305 (1998).

[107] G. R. Luckhurst and S. Romano, Liq. Cryst. **26**, 871 (1999).

[108] J. Ilnytskyi, S. Sokołowski, and O. Pizio, Phys. Rev. E **59**, 4161 (1999).

[109] K. Venu, V. S. S. Sastry, and K. P. N. Murthy, Europhys. Lett. **58**, 646 (2002).

[110] B. J. Berne and P. Pechukas, J. Chem. Phys. **56**, 4213 (1972).

[111] J. G. Gay and B. J. Berne, J. Chem. Phys. **74**, 3316 (1981).

[112] R. Berardi, L. Muccioli, and C. Zannoni, Chem. Phys. Chem. **5**, 104 (2004).

[113] C. Chiccoli, P. Pasini, F. Semeria, E. Berggren, and C. Zannoni, Mol. Cryst. Liq. Cryst. **266**, 241 (1995).

[114] G. S. Preeti, K. Murthy, V. Sastry, C. Chiccoli, P. Pasini, R. Berardi, and C. Zannoni, Soft Matter **7**, 11483 (2011).

[115] M. P. Allen and D. J. Tildesley, *Computer simulation of liquids*, Oxford science publications (Clarendon Press, 1987).

[116] D. Frenkel and B. Smit, *Understanding Molecular Simulation: From Algorithms to Applications*, vol. 1 (Academic press, San Diego, 2002).

[117] D. P. Landau and K. Binder, *A Guide To Monte Carlo Simulations In Statistical Physics* (Cambridge University Press, 2005).

[118] M. E. Newman, G. T. Barkema, and M. Newman, *Monte Carlo methods in statistical physics*, vol. 13 (Clarendon Press Oxford, 1999).

[119] K. P. N. Murthy, *Monte Carlo methods in statistical physics* (Universities Press, 2004).

[120] N. Metropolis, A. W. Rosenbluth, M. N. Rosenbluth, A. H. Teller, and E. Teller, J. Chem. Phys. **21**, 1087 (1953).

[121] J. A. Barker and R. O. Watts, Chem. Phys. Lett. **3**, 144 (1969).

[122] C. Chiccoli, O. Lavrentovich, P. Pasini, and C. Zannoni, Phys. Rev. Lett. **79**, 4401 (1997).

[123] G. Pawlik, A. Mitus, and A. Miniewicz, Opt. Commun. **182**, 249 (2000).

[124] C. Chiccoli, P. Pasini, F. Semeria, and C. Zannoni, Mol. Cryst. Liq. Cryst. **212**, 197 (1992).

[125] E. Berggren, C. Zannoni, C. Chiccoli, P. Pasini, and F. Semeria, Phys. Rev. E **49**, 614 (1994).

[126] P. Pasini, G. Skačej, and C. Zannoni, Chem. Phys. Lett **413**, 463 (2005).

[127] Y.-K. Yu, P. Taylor, and E. Terentjev, Phys. Rev. Lett. **81**, 128 (1998).

[128] G. Skačej and C. Zannoni, Proc. Nat. Acad. Sc. **109**, 10193 (2012).

[129] R. Ruhwandl and E. Terentjev, Phys. Rev. E **56**, 5561 (1997).

[130] M. P. Allen, Liq. Cryst. **8**, 499 (1990).

[131] P. W. Kasteleyn and C. M. Fortuin, J. Phys. Soc. Jpn. Suppl. **26** (1969).

[132] C. M. Fortuin and P. W. Kasteleyn, Physica **57**, 536 (1972).

[133] R. H. Swendsen and J.-S. Wang, Phys. Rev. Lett. **58**, 86 (1987).

[134] U. Wolff, Phys. Rev. Lett. **62**, 361 (1989).

[135] G. M. Torrie and J. P. Valleau, J. Comp. Phys. **23**, 187 (1977).

[136] C. H. Bennett, J. Comp. Phys. **22**, 245 (1976).

[137] A. M. Ferrenberg and R. H. Swendsen, Phys. Rev. Lett. **61**, 2635 (1988).

[138] A. M. Ferrenberg and D. P. Landau, Phys. Rev. B **44**, 5081 (1991).

[139] A. M. Ferrenberg and R. H. Swendsen, Phys. Rev. Lett. **63**, 1195 (1989).

[140] B. A. Berg and T. Neuhaus, Phys. Lett. B **267**, 249 (1991).

[141] B. A. Berg and T. Neuhaus, Phys. Rev. Lett. **68**, 9 (1992).

[142] B. A. Berg, Fields Inst. Commun **26**, 1 (2000).

[143] B. A. Berg and T. Celik, Phys. Rev. Lett. **69**, 2292 (1992).

[144] A. P. Lyubartsev, A. A. Martsinovski, S. V. Shevkunov, and P. N. Vorontsov-Velyaminov, J. Chem. Phys. **96**, 1776 (1992).

[145] E. Marinari and G. Parisi, Europhys. Lett. **19**, 451 (1992).

[146] K. Hukushima and K. Nemoto, J. Phys. Soc. Japan **65**, 1604 (1996).

[147] J. Lee, Phys. Rev. Lett. **71**, 211 (1993).

[148] I. Shteto, J. Linares, and F. Varret, Phys. Rev. E **56**, 5128 (1997).

[149] J. Linares, C. Enachescu, K. Boukheddaden, and F. Varret, Polyhedron **22**, 2453 (2003).

[150] A. R. de Lima, P. M. C. de Oliveira, and T. J. P. Penna, J. Stat. Phys. **99**, 691 (2000).

[151] R. Dickman and A. Cunha-Netto, Phys. Rev. E **84**, 026701 (2011).

[152] V. Souza Leite and W. Figueiredo, Physica A **350**, 379 (2005).

[153] C.-Y. Lee and S. K. Han, Phys. Rev. E **57**, 3611 (1998).

[154] M. Y. Choi, H. Y. Lee, D. Kim, and S. H. Park, J. Phys. A **30**, L749 (1997).

[155] F. Wang and D. P. Landau, Phys. Rev. Lett. **86**, 2050 (2001).

[156] F. Wang and D. P. Landau, Phys. Rev. E **64**, 056101 (2001).

[157] A. Malakis, S. Martinos, I. Hadjiagapiou, N. Fytas, and P. Kalozoumis, Phys. Rev. E **72**, 066120 (2005).

[158] A. Malakis and N. G. Fytas, Phys. Rev. E **73**, 056114 (2006).

[159] R. E. Belardinelli and V. D. Pereyra, J. Chem. Phys. **127**, 184105 (2007).

[160] P. N. Vorontsov-Velyaminov, N. A. Volkov, and A. A. Yurchenko, J. Phys. A **37**, 1573 (2004).

[161] N. A. Volkov, A. A. Yurchenko, A. P. Lyubartsev, and P. N. Vorontsov-Velyaminov, Macromol. Th. Sim. **14**, 491 (2005).

[162] N. A. Volkov, P. N. Vorontsov-Velyaminov, and A. P. Lyubartsev, Phys. Rev. E **75**, 016705 (2007).

[163] T. S. Jain and J. J. de Pablo, J. Chem. Phys. **116**, 7238 (2002).

[164] M. Troyer, S. Wessel, and F. Alet, Phys. Rev. Lett. **90**, 120201 (2003).

[165] P. N. Vorontsov-Velyaminov and A. P. Lyubartsev, J. Phys. A **36**, 685 (2003).

[166] Y. Okabe, Y. Tomita, and C. Yamaguchi, Comp. Phys. Commun. **146**, 63 (2002).

[167] N. Rathore and J. J. de Pablo, J. Chem. Phys. **116**, 7225 (2002).

[168] D. Jayasri, N. Satyavathi, V. S. S. Sastry, and K. P. N. Murthy, Physica A **388**, 385 (2009).

[169] R. Jose, D. Jayasri, S. Dhara, K. P. N. Murthy, and V. S. S. Sastry, Mol. Cryst. Liq. Cryst. **545**, 168 (2011).

[170] J. Dontabhaktuni, R. Jose, K. P. N. Murthy, and V. S. S. Sastry, Comp. Mat. Sc. **92**, 238 (2014).

[171] M. S. Shell, P. G. Debenedetti, and A. Z. Panagiotopoulos, Phys. Rev. E **66**, 056703 (2002).

[172] F. Calvo, Mol. Phys. **100**, 3421 (2002).

[173] C. Zhou, T. C. Schulthess, S. Torbrügge, and D. P. Landau, Phys. Rev. Lett. **96**, 120201 (2006).

[174] D. Jayasri, Ph. D. Thesis, University of Hyderabad (2009).

[175] B. A. Berg, Comp. Phys. Commun. **153**, 397 (2003).

[176] C. Zannoni, J. Chem. Phys **84**, 424 (1986).

[177] P. Pasini and C. Zannoni, *Advances in the computer simulations of liquid crystals*, vol. 545 (Springer, 1999).

[178] K. Binder, Phys. Rev. Lett. **47**, 693 (1981).

[179] M. S. S. Challa, D. P. Landau, and K. Binder, Phys. Rev. B **34**, 1841 (1986).

[180] G. P. Crawford and S. Žumer, *Liquid crystals in complex geometries: formed by polymer and porous networks* (CRC Press, 1996).

[181] P. Sheng, Phys. Rev. Lett. **37**, 1059 (1976).

[182] P. Sheng, Phys. Rev. A **26**, 1610 (1982).

[183] G. Barbero and R. Barberi, J. de Physique **44**, 609 (1983).

[184] A. Poniewierski and T. J. Sluckint, Liquid Crystals **2**, 281 (1987).

[185] M. M. T. da Gama and P. Tarazona, Phys. Rev. A **41**, 1149 (1990).

[186] T. Gruhn and M. Schoen, J. Chem. Phys. **108**, 9124 (1998).

[187] G. Skačej, A. L. Alexe-Ionescu, G. Barbero, and S. Žumer, Phys. Rev. E **57**, 1780 (1998).

[188] A. Šarlah and S. Žumer, Phys. Rev. E **60**, 1821 (1999).

[189] D. J. Cleaver and P. I. C. Teixeira, Chem. Phys. Lett. **338**, 1 (2001).

[190] R. Barberi, F. Ciuchi, G. E. Durand, M. Iovane, D. Sikharulidze, A. M. Sonnet, and E. G. Virga, E. Phys. J. E **13**, 61 (2004).

[191] C. Care and D. Cleaver, Reports on progress in physics **68**, 2665 (2005).

[192] C. Chiccoli, P. Pasini, G. Skačej, and C. Zannoni, Mol. Cryst. Liq. Cryst. **429**, 255 (2005).

[193] C. Chiccoli, S. P. Gouripeddi, P. Pasini, K. P. N. Murthy, V. S. S. Sastry, and C. Zannoni, Mol. Cryst. Liq. Cryst. **500**, 118 (2009).

[194] R. G. Marguta, Y. Martínez-Ratón, N. G. Almarza, and E. Velasco, Phys. Rev. E **83**, 041701 (2011).

[195] G. P. Crawford, D. W. Allender, and J. Doane, Phys. Rev. A **45**, 8693 (1992).

[196] R. Ondris-Crawford, G. Crawford, S. Žumer, and J. Doane, Phys. Rev. Lett. **70**, 194 (1993).

[197] C. Chiccoli, P. Pasini, F. Semeria, E. Berggren, and C. Zannoni, Mol. Cryst. Liq. Cryst. **290**, 237 (1996).

[198] Z. Bradač, S. Kralj, and S. Žumer, Phys. Rev. E **58**, 7447 (1998).

[199] N. V. Priezjev, G. Skačej, R. A. Pelcovits, and S. Žumer, Phys. Rev. E **68**, 041709 (2003).

[200] G. Sai Preeti, V. Vijay Kumar, V. Sastry, and K. Murthy, Comp. Mat. Sc. **44**, 180 (2008).

[201] C. Chiccoli, P. Pasini, L. Evangelista, R. Teixeira De Souza, and C. Zannoni, Mol. Cryst. Liq. Cryst. **576**, 42 (2013).

[202] J. H. Erdmann, S. Žumer, and J. W. Doane, Phys. Rev. Lett. **64**, 1907 (1990).

[203] C. Chiccoli, P. Pasini, F. Semeria, and C. Zannoni, Physics Letters A **150**, 311 (1990).

[204] C. Chiccoli, P. Pasini, F. Semeria, and C. Zannoni, Mol. Cryst. Liq. Cryst. **221**, 19 (1992).

[205] C. Chiccoli, P. Pasini, G. Skačej, C. Zannoni, and S. Žumer, Phys. Rev. E **60**, 4219 (1999).

[206] D. Jayasri, T. Sairam, K. P. N. Murthy, and V. S. S. Sastry, Physica A **390**, 4549 (2011).

[207] M. Dadmun and M. Muthukumar, J. Chem. Phys. **98**, 4850 (1993).

[208] G. S. Iannacchione, S. Qian, D. Finotello, and F. M. Aliev, Phys. Rev. E **56**, 554 (1997).

[209] T. Araki, M. Buscaglia, T. Bellini, and H. Tanaka, Nature Mat **10**, 303 (2011).

[210] V. S. U. Fazio, L. Komitov, and S. T. Lagerwall, Liq. Cryst. **24**, 427 (1998).

[211] A. D. Rey and M. M. Denn, Ann. Rev. Fluid Mech. **34**, 233 (2002).

[212] V. M. Pergamenshchik, P. I. C. Teixeira, and T. J. Sluckin, Phys. Rev. E **48**, 1265 (1993).

[213] O. D. Lavrentovich and V. M. Pergamenshchik, Int. J. Mod. Phys. B **9**, 2389 (1995).

[214] R. Soref and M. Rafuse, Journal of Applied Physics **43**, 2029 (1972).

[215] F. Brochard, L. Leger, and R. B. Meyer, J. de Physique **36**, C1 (1975).

[216] D. R. M. Williams and A. Halperin, Macromolecules **26**, 2025 (1993).

[217] W. Turalski, A. Miniewicz, and A. C. Mitus, Adv. Mat. Opt. Elec. **7**, 71 (1997).

[218] Y. Yang, J. Lu, H. Zhang, and D. Yan, Mol. Cryst. Liq. Cryst. **259**, 23 (1995).

[219] S. D. Durbin, S. M. Arakelian, and Y. R. Shen, Phys. Rev. Lett. **47**, 1411 (1981).

[220] A. J. Karn, S. M. Arakelian, Y. R. Shen, and H. L. Ong, Phys. Rev. Lett. **57**, 448 (1986).

[221] H. L. Ong, Phys. Rev. A **28**, 2393 (1983).

[222] F. Lonberg and R. B. Meyer, Phys. Rev. Lett. **55**, 718 (1985).

[223] G. Srajer, S. Fraden, and R. B. Meyer, Phys. Rev. A **39**, 4828 (1989).

[224] F. Lonberg, S. Fraden, A. J. Hurd, and R. E. Meyer, Phys. Rev. Lett. **52**, 1903 (1984).

[225] N. Priezjev and R. A. Pelcovits, Phys. Rev. E **62**, 6734 (2000).

[226] G. Boyd, J. Cheng, and P. Ngo, Appl. Phys. Lett. **36**, 556 (1980).

[227] I. Dozov and G. Durand, Liq. Cryst. Today **8**, 1 (1998).

[228] S. Bhar and S. K. Roy, Comp. Phys. Commun. **180**, 699 (2009).

[229] S. Sinha and S. K. Roy, Phys. Lett. A **373**, 308 (2009).

[230] T. Schilling and D. Frenkel, Phys. Rev. Lett. **92**, 085505 (2004).

[231] H.-W. Chiu and T. Kyu, J. Chem. Phys. **110**, 5998 (1999).

[232] C. Shen and T. Kyu, J. Chem. Phys. **102**, 556 (1995).

[233] G. De Matteis and S. Romano, Phys. Rev. E **78**, 021702 (2008).

[234] D. A. Dunmur and P. Palffy-Muhoray, J. Phys. Chem. **92**, 1406 (1988).

[235] I. Lelidis, M. Nobili, and G. Durand, Phys. Rev. E **48**, 3818 (1993).

[236] P. Palffy-Muhoray and D. A. Dunmur, Mol. Cryst. Liq. Cryst. **97**, 337 (1983).

[237] G. R. Luckhurst, P. Simpson, and C. Zannoni, Chem. Phys. Lett. **78**, 429 (1981).

[238] G. R. Luckhurst and P. Simpson, Chem. Phys. Lett. **95**, 149 (1983).

[239] W. Turalski, A. C. Mitus, and A. Miniewicz, Pure Appl. Opt. **6**, 589 (1997).

[240] N. Ghoshal, K. Mukhopadhyay, and S. K. Roy, Phys. Rev. E **89**, 042505 (2014).

[241] I. Muševič, M. Škarabot, U. Tkalec, M. Ravnik, and S. Žumer, Science **313**, 954 (2006).

[242] M. Ravnik, G. P. Alexander, J. M. Yeomans, and S. Žumer, Proc. Natl. Acad. Sci. **108**, 5188 (2011).

[243] T. Araki, F. Serra, and H. Tanaka, Soft Matter **9**, 8107 (2013).

[244] I. I. Smalyukh, A. N. Kuzmin, A. V. Kachynski, P. N. Prasad, and O. D. Lavrentovich, Appl. Phys. Lett. **86**, 021913 (2005).

[245] M. Škarabot, M. Ravnik, D. Babič, N. Osterman, I. Poberaj, S. Žumer, I. Muševič, A. Nych, U. Ognysta, and V. Nazarenko, Phys. Rev. E **73**, 021705 (2006).

[246] S. Žumer, I. Muševič, M. Ravnik, M. Škarabot, I. Poberaj, B. Dušan, and T. Uroš, Proc. SPIE **6911**, 69110C (2008).

[247] D. Pires, J.-B. Fleury, and Y. Galerne, Phys. Rev. Lett. **98**, 247801 (2007).

[248] J.-B. Fleury, D. Pires, and Y. Galerne, Phys. Rev. Lett. **103**, 267801 (2009).

[249] P. Kossyrev, M. Ravnik, and S. Žumer, Phys. Rev. Lett. **96**, 048301 (2006).

[250] N. Osterman, J. Kotar, E. M. Terentjev, and P. Cicuta, Phys. Rev. E **81**, 061701 (2010).

[251] T. Araki and H. Tanaka, J. Phys.: Condens. Matter **18**, L193 (2006).

[252] A. V. Ryzhkova and I. Muševič, Phys. Rev. E **87**, 032501 (2013).

[253] J. Milette, V. Toader, E. R. Soulé, R. B. Lennox, A. D. Rey, and L. Reven, Langmuir **29**, 1258 (2013).

[254] G. M. Koenig Jr, J. J. de Pablo, and N. L. Abbott, Langmuir **25**, 13318 (2009).

[255] F. R. Hung, B. T. Gettelfinger, G. M. Koenig Jr, N. L. Abbott, and J. J. de Pablo, J. Chemical Phys. **127**, 124702 (2007).

[256] J. A. Moreno-Razo, E. J. Sambriski, G. M. Koenig, E. Díaz-Herrera, N. L. Abbott, and J. de Pablo, Soft Matter **7**, 6828 (2011).

[257] J. K. Whitmer, A. A. Joshi, T. F. Roberts, and J. J. de Pablo, J. Chem. Phys. **138**, 194903 (2013).

[258] J. K. Whitmer, X. Wang, F. Mondiot, D. S. Miller, N. L. Abbott, and J. J. de Pablo, Phys. Rev. Lett. **111**, 227801 (2013).

[259] R. Jose, G. Skačej, V. S. S. Sastry, and S. Žumer, Phys. Rev. E **90**, 032503 (2014).

[260] P. M. Chaikin and T. C. Lubensky, *Principles of Condensed Matter Physics*, vol. 1 (Cambridge University Press, Cambridge, 1997).

[261] D. Frenkel and B. Smit, *Understanding molecular simulation: from algorithms to applications*, vol. 1 (Academic press, 2001).

[262] G. Raos and G. Allegra, J. Chem. Phys. **113**, 7554 (2000).

[263] A. C. Callan-Jones, R. A. Pelcovits, V. A. Slavin, S. Zhang, D. H. Laidlaw, and G. B. Loriot, Phys. Rev. E **74**, 061701 (2006).

[264] A. Mertelj and M. Čopič, Phys. Rev. E **69**, 021711 (2004).

Publications

1. **Regina Jose**, D. Jayasri, Surajit Dhara, K. P. N. Murthy and V. S. S. Sastry, *Effect of external field on the nematic to isotropic transition: An entropic sampling study*, Molecular Crystals and Liquid Crystals, **545**, 168 (2011).

2. S. C. R. Roshan, Lavanya Kunduru, **Regina Jose**, K. P. N. Murthy, and V. S. S. Sastry, *Azimuthal bistability in patterened nematic liquid crystal films: A Monte Carlo study*, AIP Conference Proceedings, **1349**, 178 (2011).

3. B. Kamala Latha, **Regina Jose**, K. P. N. Murthy, and V. S. S. Sastry, *Detection of an intermediate biaxial phase in the phase diagram of biaxial liquid crystals: Entropic sampling study*, Physical Review E, **89**, 050501(R) (2014).

4. D. Jayasri, **Regina Jose**, K. P. N. Murthy, and V. S. S. Sastry, *Effect of phase shift between geometrical and chemical patterning in nematic liquid crystal cells: A Monte Carlo study*, Computational Materials Science, **92**, 238 (2014).

5. **Regina Jose**, Gregor Skačej, V. S. S. Sastry, and Slobodan Žumer, *Colloidal nanoparticles trapped by liquid crystal defect lines: A lattice Monte Carlo simulation*, Physical Review E, **90**, 032503 (2014).

6. B. Kamala Latha, **Regina Jose**, K. P. N. Murthy and V. S. S. Sastry, *Mean field phase diagram of biaxial nematics revisited: New insights from Monte Carlo studies*, Physical Review E (2014) – under review.

Manuscripts under preparation

1. **Regina Jose**, D. Jayasri, K. P. N. Murthy and V. S. S. Sastry, *Detection of topologically distinct director structures in planar nematic films: Development of novel sampling technique.*

2. **Regina Jose**, B. Kamala Latha, K. P. N. Murthy, and V. S. S. Sastry, *Effect of external field on biaxial nematic transitions: Sensitivity to competing microscopic interactions.*

3. **Regina Jose**, K. P. N. Murthy, and V. S. S. Sastry, *Application of order parameter-based sampling technique to nematic liquid crystals.*